Lehrstuhl für Akustik Mobiler Systeme

Structural Dynamics of Ultrasonic Transducers: Simulation and Experiment

Johannes Henneberg

Vollständiger Abdruck der von der Fakultät für Maschinenwesen der Technischen Universität München zur Erlangung des akademischen Grades eines

Doktor-Ingenieurs (Dr.-Ing.)

genehmigten Dissertation.

Vorsitzender: apl. Prof. Dr.-Ing. Christian Stemmer

Prüfer der Dissertation: 1. Prof. Dr.-Ing. Steffen Marburg
2. Prof. Dr.-Ing. Holger Cebulla

Die Dissertation wurde am 22.08.2019 bei der Technischen Universität München eingereicht und durch die Fakultät für Maschinenwesen am 21.01.2020 angenommen.

Kurzfassung

Der zunehmende Automatisierungsgrad in den Bereichen von Automobil-, Robotik- und Industrieanwendungen erfordert Umfeldsensierungssysteme mit erhöhter Leistungsfähigkeit und Zuverlässigkeit. Schallwandler, die im Ultraschallbereich arbeiten, stellen eine bekannte und weit verbreitete Technik zur Umfeldsensierung dar, welche insbesondere im Nahfeldbereich < 6 m eingesetzt wird.

Die vorliegende Arbeit untersucht neue Konzepte, um die Leistungsfähigkeit von Ultraschallwandlern zu erhöhen. Dies kann sich in unterschiedlichen Eigenschaften widerspiegeln. Dazu zählen die Überwindung von Designbeschränkungen zur Erzielung anisotroper Richtcharakteristiken, die Herstellung eines Mehrfrequenz-Ultraschallwandlers mit nur einem elektromechanischen Kopplungselement und die Reduktion des mechanischen Übersprechens in Phased-Array-Wandlern mit einer gemeinsamen Trägerstruktur.

Die neuen Konzepte werden in numerischen Simulationen mit Hilfe der finiten Elemente Methode untersucht. Anschließend wird die Wirksamkeit mit experimentellen Verfahren nachgewiesen. Das Wellenausbreitungsverhalten in periodischen Strukturen wird durch das Dispersionsverhalten innerhalb einer Einheitszelle untersucht. Die Berechnung erfolgt mit der sogenannten wave finite element method. Die Schallabstrahlung der untersuchten Komponenten wird durch die Kopplung der Berechnungsergebnisse der finiten Elemente Methode mit dem Rayleigh Integral ermittelt.

Der erste Ansatz, der untersucht wird, beruht auf dem Prinzip lokal strukturierter Faser-Verbund-Werkstoffe. Dieser Ansatz eröffnet eine neue Gestaltungsdimension im Vergleich zu klassischen Werkstoffen. Durch die Kombination von faserverstärkten Bereichen mit unverstärkten Bereichen können lokal verschiedene Materialeigenschaften erzielt werden. Diese ermöglichen die Einstellung anisotroper Richtcharakteristiken bei einer rotationssymmetrischen Gestaltung des Schallwandlers. Somit können bestehende Einschränkungen der heutigen Schallwandlergestaltung überwunden werden. Im zweiten vorgestellten Konzept wird lokal verteiltes Stopp Band Material untersucht. Ziel ist es, die Herstellung von Mehrfrequenz-Schallwandlern mit nur einem elektromechanischen Kopplungselement zu ermöglichen. Es wird gezeigt, dass bei unterschiedlichen Arbeitsfrequenzen Schwingungsformen mit geeigneter Schallabstrahlung für die Umfeldsensierung erzielt werden können. Im dritten Konzept wird der Einsatz von Stopp Band Material in Phased-Array-Wandlern zur Reduktion des Übersprechens untersucht. Das vorgestellte Konzept adressiert insbesondere kompakte, tieffrequente, luftgekoppelte Array-Wandler. Es wird gezeigt, dass bei korrekter Abstimmung des Frequnzstoppbands auf die Betriebsfrequenz des Schallwandlers eine signifikante Reduktion des Übersprechens erzielt werden kann.

Die vorgestellten, neuen Konzepte tragen zur Steigerung der Leistungsfähigkeit und Zuverlässigkeit von Ultraschallwandlern bei. Daraus resultierend können leistungsfähigere Umfeldsensierungssysteme entwickelt werden.

Abstract

The increasing level of automation in automotive, robotic, and industrial applications requires growing performance and reliability of surround sensing systems. Sound transducers operating in the ultrasonic frequency range are a well-known technique for surround sensing purposes. Ultrasonic transducers are used for obstacle detection, especially in the short range distance < 6 m.

This work investigates new approaches to increase the performance of ultrasonic transducers. The increased performance can be reflected in the reduction of design limitations to achieve anisotropic directivity patterns, in the accomplishment of multi-frequency ultrasonic transducers having only one electro-mechanical coupling element, or in the reduction of mechanical cross-coupling in phased array transducers with a common backing.

All presented approaches are studied in finite element simulations as well as experimental testing. In order to investigate the dynamic behavior of periodic stop band material, the dispersion relations are calculated in the unit cell. Therefore, the wave finite element method is applied. The sound radiation behavior and the resulting directivity patterns are determined with an approach coupling finite element simulation and the Rayleigh integral.

The first approach uses locally structured fiber reinforcement in composite materials as a new design space. Sections with and without fiber reinforcement are combined resulting in a monolithic structure with various material properties. This finally enables the design of ultrasonic transducer with highly anisotropic directivity patterns and a rotationally symmetric geometry at the same time. The second approach investigates the potential of stop band material to achieve a multi-frequency ultrasonic transducer. Due to the particular dynamic properties of the stop band material, the operational deflection shape of the ultrasonic transducer can be modified within a certain frequency range. Hence, only one electro-mechanical coupling element is required to achieve a multi-frequency ultrasonic transducers. It is shown that suitable sound radiation behavior can be achieved at two operating frequencies. The third approach addresses the field of ultrasonic array transducers. Mechanical cross-coupling caused by a common backing is a serious issue in compact, low frequency, air-coupled ultrasonic array transducers. The usage of stop band material as common backing is a suitable solution to overcome this issue.

The approaches presented in this work contribute to increase the performance and reliability of ultrasonic transducers. Finally, this opens up the possibility to develop more comprehensive surround sensing systems.

Danksagung

"Nicht die Glücklichen sind dankbar. Es sind die Dankbaren, die glücklich sind."

Francis Bacon

Und darum bildet Dankbarkeit das Fundament, auf dem diese Arbeit entstanden ist. Dieser Dank gilt allen die durch große und kleine Debatten, mit bestärkenden Worten, kontroversen Diskussionen, einer helfenden Hand oder ganz einfach Vertrauen zum Gelingen der Arbeit beigetragen haben.

Mein ganz besonderer Dank gebührt meinem Doktorvater Prof. Dr.-Ing. Steffen Marburg. Mit zahlreichen fachlichen Diskussionen, Anregungen und kritischen Fragen hast Du, lieber Steffen, diese Arbeit überhaupt erst ermöglicht. Und obwohl das zweifelsohne schon viel ist, machten erst die Zwischenmenschlichkeiten, getragen von weisen Ratschlägen und gespickt mit spitzfindigem Humor, die Zeit so lehrreich und außergewöhnlich für mich. Danke! Meinem Zweitprüfer Herrn Prof. Dr.-Ing. Holger Cebulla danke ich recht herzlich für die Begleitung der Arbeit während der gesamten Bearbeitungsdauer. Herrn apl. Prof. Dr.-Ing. Christian Stemmer danke ich vielmals für die kurzfristige Übernahme des Vorsitzes der Prüfungskommission.

Mein herzlicher Dank gilt Dr.-Ing. André Gerlach, der mich als industrieller Betreuer seitens der Robert Bosch GmbH seit vielen Jahren begleitet. Du, lieber André, hast meine Begeisterung für die Ultraschallsensorik geweckt und mit Deiner fachlichen Begleitung den Verlauf meiner Promotionszeit maßgeblich geprägt. Deine Weitsicht kombiniert mit Vertrauen und großem Geschick haben es mir ermöglicht, diese Arbeit im industriellen Umfeld zu erstellen. Vielen Dank.

Ein herzliches Dankeschön gilt Dir, lieber Bernd. Deine Unterstützung und Dein Vertrauen in meine Forschung gaben mir Auftrieb, wenn ich mich unter Wasser fühlte. Dir, lieber Heiner, gilt mein herzlicher Dank für unzählige kurze Diskussionen, die am Ende doch nie so kurz waren wie anfangs gedacht. Ohne Dich hätte ich vermutlich nie erfahren, wie viel mit Feder-Masse-Systemen mit drei oder weniger Freiheitsgraden erklärbar ist. Des Weiteren bedanke ich mich bei allen Kollegen der Abteilung CR/ARF1, die mich in vielen unterschiedlichen Aspekten unterstützt haben. Der Robert Bosch GmbH danke ich für die Finanzierung der Arbeit inklusive der dazugehörigen Konferenzbesuche.

Als ich meine Promotion begann, war Steffen mit seiner Mannschaft noch an der Universität der Bundeswehr München. Hier fühlte ich mich von Anfang an herzlich aufgenommen und gut integriert. Dafür danke ich Euch allen ganz herzlich. Und auch nach dem Wechsel an die Technische

Universität München sollte sich das nicht ändern. Bald begann dann meine Münchner Zeit - eine sehr intensive und lehrreiche, vor allem aber sehr schöne Zeit. Ein herzliches Dankeschön an alle Mitarbeiter des Lehrstuhls für Akustik mobiler Systeme. Mein außerordentlicher Dank gilt Dir, Patrick. Gerne erinnere ich mich an den gemeinsamen, morgendlichen „Caffè“, ein Bier am Abend und großartige Konferenzen. Auch konnte ich bei Dir immer eine Bleibe finden. Niemand vermag zu ahnen, wie gut es sich unter Deinem Küchentisch schlafen lässt. Danke Chief!

Ein großes Dankeschön an meine Freunde, insbesondere Marc, Max und Stefan. Gemeinsame Urlaube, eine Runde Pub-Quiz am Montagabend oder auch eine Mate in der großen, weiten Welt waren eine Bereicherung und willkommene Abwechselung.

Tiefer Dank gebührt meiner Familie, insbesondere meinen Eltern, Julia und Matthias, sowie meinen beiden Brüdern, Martin und Christian. Ihr habt mich zu dem gemacht, der ich heute bin und mit allem ausgestattet was ich zum Leben brauche. Ohne Euch wäre eine solche Arbeit nicht möglich gewesen. Dankeschön.

Mein größter Dank gilt meiner lieben Viktoria. Ich danke Dir für jeden Augenblick den Du mich begleitest und für Deine großartige Unterstützung in allen Facetten. In schönen Momenten konnte ich mit Dir die Freude teilen. In schwierigen Momenten vermochtest Du, mich wieder aufzubauen. Für Deine Liebe und Selbstlosigkeit bin ich Dir zu tiefst dankbar.

Gewidmet meiner lieben Mama und meinem lieben Papa.

Appended papers

A J. Henneberg, A. Gerlach, H. Cebulla, S. Marburg, Locally structured fiber reinforcements: An approach to realize anisotropic directivity pattern in ultrasound transducers, accepted for publication in: SAE Technical Paper, SAE International, 2018

Henneberg developed the approach of locally structured fiber reinforcement. The numerical simulation, the test specimen preparation, and the experimental testing were done by Henneberg. Gerlach contributed to the ultrasonic transducer design. Cebulla contributed in the design of the locally structured fiber reinforcement. Marburg discussed the theory. Cebulla and Marburg supervised the work.

B J. Henneberg, A. Gerlach, H. Cebulla, S. Marburg, The potential of stop band material in multi-frequency ultrasonic transducers, Journal of Sound and Vibration 452 (2019) 132 - 146.

Henneberg developed the approach of distributed stop band material for the purpose of multi-frequency ultrasonic transducers, conducted the simulations, and the experiments. Gerlach defined the design requirements for multi-frequency ultrasonic transducers. Marburg discussed the theory. Cebulla and Marburg supervised the work.

C J. Henneberg, A. Gerlach, H. Storck, H. Cebulla, S. Marburg, Reducing mechanical cross-coupling in phased array transducers using stop band material as backing, Journal of Sound and Vibration 424 (2018) 352 - 364.

Henneberg introduced the idea of using stop band material as backing, conducted the numerical simulations and the experiments. Gerlach contributed the requirements for the design of phased transducer arrays. Storck contributed the analysis and interpretation of cross-coupling in harmonic analysis. Cebulla and Marburg supervised the work.

Publications not appended to this work

- J. Henneberg, A. Gerlach, H. Cebulla, S. Marburg, Reducing mechanical cross-coupling in phased array transducers using acoustic metamaterial as backing, Proceedings of 24th International Congress on Sound and Vibration, Great Britain, London, 2017
- J. Henneberg, A. Gerlach, H. Cebulla, S. Marburg, Lokal strukturierte Faserverstärkungen: Ein Ansatz zur Realisierung anisotroper Richtcharakteristiken in Ultraschallsensoren, Proceedings of DAGA 2018 - 44. Jahrestagung der Deutschen Arbeitsgemeinschaft für Akustik, Germany, Munich, 2018

- J. Henneberg, A. Gerlach, H. Cebulla, S. Marburg, Lokal strukturierte Faserverstärkungen: Ein Ansatz zur Realisierung anisotroper Richtcharakteristiken in Ultraschallsensoren, Proceedings of DAGA 2018 - 44. Jahrestagung der Deutschen Arbeitsgemeinschaft für Akustik, Germany, Munich, 2018

- J. Henneberg, A. Gerlach, H. Cebulla, S. Marburg, Multi-frequency ultrasonic sensors with locally distributed resonators, Proceedings of Noise and vibration emerging methods (Novem), Spain, Ibiza, 2018
- J. Henneberg, J. S. Gomez Nieto, K. Sepahvand, A. Gerlach, H. Cebulla, S. Marburg, The influence of uncertainties in periodic structures for vibro-acoustic problems, Proceedings of International Conference on Noise and Vibration Engineering (ISMA), Belgium, Leuven 2018
- J. Henneberg, S. Preuss, A. Gerlach, S. Marburg, Multifrequency ultrasonic transducers with spatially distributed stop band material, Proceedings of the 23rd International Congress on Acoustics, Germany, Aachen, 2019, *accepted for publication*

Contents

List of Figures

Part I

Summary and Overview

Chapter 1

Introduction

Paul Langevin and Constantin Chilowsky can be denoted as the inventors of modern, technical ultrasonic transducers in surround sensing applications [1, 2]. However, bats have been using the principle of echolocating for thousands of years [3]. During World War I, Langevin and Chilowsky developed an underwater sonar for the purpose of submarine detection. In 1916, they managed to receive echo signals from a distance up to 200 m. About that time, Chilowsky left the working group while Langevin continued his work. Two years later, he could increase the detectable range up to 1500 m [4]. The newly developed transducer was based on a piezoelectric quartz crystal which was a key element to reach this performance. Even if it took more than 30 years to make it usable in a real ultrasonic transducer application, the discovery of the piezoelectric effect by the brothers Pierre and Jacques Curie in 1880 [5] was the main driver for the development, not only for ultrasonic transducers, but for electroacoustic transducers in general. The term ultrasonic sound or ultrasound describes sound waves with a frequency above the upper hearing limit of humans. This is usually denoted to 16 kHz [6].

During the last decades, the automotive and robotic sectors have pushed the development of compact, air-coupled ultrasonic transducer for surround sensing purposes. The increasing automation level and autonomous driving functions lead to continuous developments in surround sensing systems. Therefore, ultrasonic transducer with extended functionality are desired. The improvement of the performance can be defined with different purposes, namely the enhancement of the range for obstacle detection, the reduction of measurement time, and the achievement of angle information between obstacle and transducer. This work addresses the various purposes employing mainly two approaches. The first approach is related to the usage of fiber reinforced composites. This class of material offers the possibility to vary the material properties within a monolithic structure. A novel concept to realize ultrasonic transducers is investigated based on this approach. The aim is to achieve highly anisotropic directivity patterns without restricting the transducer topology. The second approach refers to the characteristic property of acoustic metamaterial to exhibit stop bands. The presented research investigates a possiblity to increase the performance in ultrasonic transducers and ultrasonic transducer arrays based on acoustic metamaterial. Thus, existing approaches for ultrasonic transducers are enhanced and novel concepts are proposed. The investigations comprise numerical simulations and experimental validation. In the first part of this thesis, an introduction to the topic of structural dynamics of ultrasonic transducers is given. The state of the art in the field of ultrasonic transducers as well as in the field of the applied approaches is discussed. Afterwards, the investigated models are presented. Subsequently, a summary is given for each of the three appended papers. The first part ends with a discussion of the results and a conclusion. The three papers form the second part of this thesis and have been published in this context. The papers contain detailed results of the investigated approaches.

1.1 State of the art

1.1.1 Ultrasonic transducers

Ultrasonic transducers can be operated in both, sound emission mode and sound reception mode. Thus, the term ultrasonic transducer indicates the possible use as a sound radiator as well as a sensor. For surround sensing purposes, the pulse-echo principle is used to detect the distance between the transducer and an obstacle, cf Fig. 1.1. Therefore, sound waves are emitted by the ultrasonic transducer in sound emission mode. These sound waves are reflected by an obstacle and subsequently are detected by the ultrasonic transducer in reception mode. The distance between sensor and obstacle is calculated by $X = c_{\mathrm{air}} \cdot \frac{\Delta t}{2}$ with Δt and c_{air} being the run time between sound emission and reception, and the sound velocity in air, respectively [7].

The electro-mechanical coupling of current ultrasonic transducers is realized mainly with the two following principles:

- piezoelectric effect,
- electrostatic, capacitive coupling.

An overview of electro-mechanical coupling mechanisms and their use in electro-acoustic transducers is given in fundamental literature of acoustics [7, 8].

In order to attain high sound pressure in emission mode and high sensitivity in reception mode, ultrasonic transducers are usually used at a resonant operating point. The determination of the op-

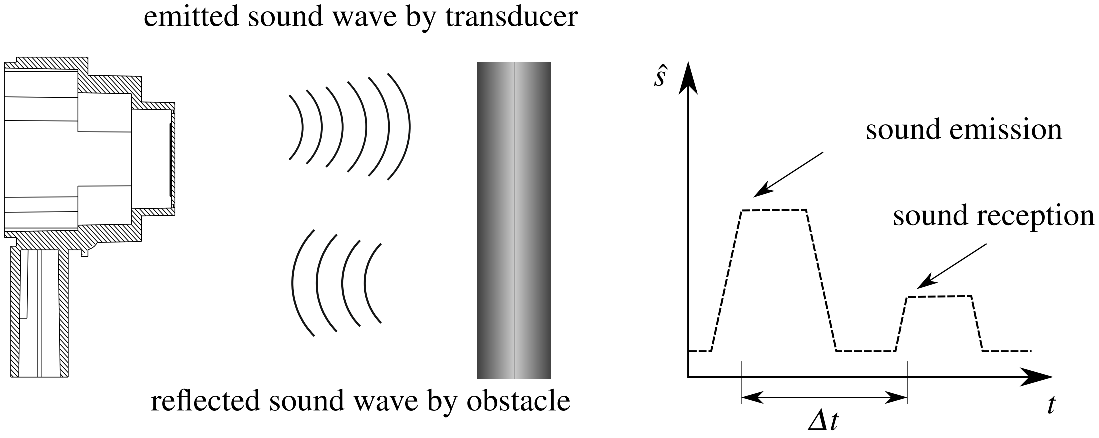

Figure 1.1: Illustration of the Pulse-Echo principle with a strongly simplified scheme of the transducer signal amplitude $\hat{s}$ and the runtime Δt between sound emission and reception, cf. [7].

erating frequency is a compromise between robustness of the measurement and achievable distance range. On one hand, a rising operating frequency results in less disturbing signals. On the other hand, the sound absorption in air increases with a rising frequency [9–11]. Present air-coupled ultrasonic sensors usually have an operating frequency between 30 kHz and 500 kHz. In automotive applications, the use of 48 kHz is very common [12].

In [13], a widely used setup for ultrasonic transducers is described. It is based on a piezoelectric ceramic assembled in a pot like structure made of metal. The concept of using functionally graded piezoelectric material is presented in [14]. The purpose of using functionally graded piezoelectric material is the reduction of stress concentration as well as the expansion of bonding strength and bandwidth. A fundamental investigation on radiation of ultrasonic waves into fluid and solid media is presented in the work of Kocbach [15]. Therefore, an axisymmetric ultrasonic piezoelectric transducers is studied employing the finite element method. The different modes of a piezoelectric disk radiator and the belonging radiated sound fields are calculated. The basic setup of an ultrasonic transducer using the electrostatic, capacitive coupling between electrical and mechanical domains is given in [16]. Due to the manufacturing process, these types of transducers are called capacitive micromachined ultrasonic transducers (CMUT). They are often used in ultrasonic phased array transducers, cf. Section 1.1.2.

The space in which obstacles can be detected is called the field of view (FOV) of a sensor. In order to achieve a considerable FOV and a large detectable distance up to 6 m, the directivity pattern of the radiated sound is in the focus of research during the last decades. In automotive and robotic applications, an anisotropic directivity pattern is desired. A wide angular aperture in the horizontal plane is proposed to detect obstacles being situated in the half space in front of the sensor. In constrast, a narrow angular aperture in the vertical plane is intended. Thus, reflections from the ground, which decrease the detectable distance, are reduced or avoided, cf. Fig. 1.2. Early developments use horns to achieve anisotropic directivity patterns like presented in [17]. In 1992, a new concept is presented by Rapps et al. [18]. The authors purpose a sensor with an embodiment which is reinforced on two opposite sides. Thus, the resulting operational deflection shape at the operating frequency leads to an anisotropic directivity pattern. Ho et al. [19] investigate the influence of altered boundary conditions in a pot like ultrasonic transmitter made of an aluminum pot and a piezoelectric ceramic. Cheng et al. [20] present a study to increase the anisotropy of directivity pattern by inserting cutting slots in the cylindrical shell of the ultrasonic transducer.

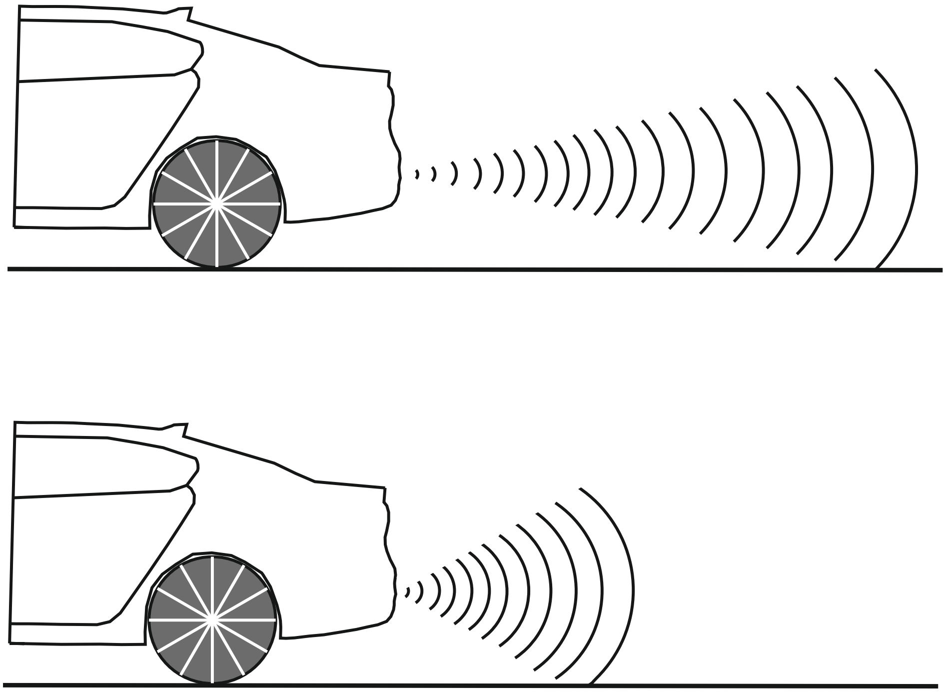

Figure 1.2: Scheme of directivity pattern of ultrasonic transducer in an automotive application with a narrow-angled beam (top) and wide-angled beam (bottom).

The rising requirements of the performance of surround sensing applications lead to the development of ultrasonic transducers with multiple operating frequencies. Thus, two objectives can be attained:

- Several sensors can be operated in parallel or in short intervals.
- Various FOV can be realized at different operating frequencies.

Already in 1948, Bundy [21] presents a stepped frequency transducer with multiple elements. The elements consist of magnetostrictive laminated nickel stack. They are mechanically isolated and linked with a common electrical winding. Thus, a broad frequency response is achieved. Depending on the damping of the system, the presented transducer can be interpreted as a multi-frequency transducer with separated resonance frequencies. In [22], a split mode ultrasonic transducer is investigated. Therefore, a two-dimensional periodic structure of poled domains in a ferroelectric wafer with free surfaces is set up. Thus, an ultrasonic transducer with multiple acousto-electric resonances is obtained. Wang and Lee [23] present a multi-frequency piezoelectric micromachined ultrasonic transducer (PMUT) with multiple electrodes. Due to multiple electrodes, the device provides high sensitivity at multiple frequencies coinciding with the first, third and fifth fundamental frequency of the transducer. In [24], a multi-frequency capacitive micromachined ultrasonic transducer array with acoustic elements of different dimensions is presented. Thus, an array transducer for multiband operation is designed. Chopra et al. [25] present a multi-frequency transducer realized with one electro-mechanical coupling element. It is achieved with various matching layers. It is used for interstitial ultrasound thermal therapy. In the same context of medical ultrasonic therapy, a dual-frequency lead zirconate titanate (PZT)-transducer array with fundamental frequency at 4.1 MHz and third harmonic at 13.3 MHz is characterized in [26]. Muttakin et al. [27] present a hybrid multi-frequency ultrasonic transducer. It consists of different electro-mechanical coupling elements. One is a piezoelectric ceramic while the other one is made of PVDF. By hybridization of both characteristic properties, the transducer enables the usage at multiple resonance frequencies. In [28], the electrical circuit, which is employed for signal processing of such a transducer, is presented. In [29], also two electro-mechanical coupling mechanisms are combined. Thus, a CMUT as well as a PMUT electro-mechanical coupling is realized in one element. The transducer can be operated at two operating frequencies. Suitable sound radiation properties for surround sensing can be expected with the obtained mode shapes at both frequencies.

1.1.2 Ultrasonic array transducers

Ultrasonic phased array transducers consist of multiple transducer elements with well defined, mostly equidistant spacing between the single transducer elements [7]. They are used in medical diagnostic, non-destructive material testing, and in surround sensing applications. While single ultrasonic transducers can only detect the distance between the transducer and an obstacle, like discussed in Section 1.1.1, phased array transducers offer more functions. In transmission mode, it is possible to electronically bend, steer, and focus the emitted sound wave. Therefore, the excitation signals of the single transducer elements are delayed as shown in Fig. 1.3. Vice-versa, in echo reception mode the angle information of an incoming wavefront can be obtained [30]. Ultrasonic phased array transducers are divided generally dependent on the arrangement of the single transducer elements. Arrangements with multiple elements in only one direction are called linear arrays. Thus, electronically bending, steering, and focusing as well as the detection of angle information from an incoming wavefront can be performed only in one direction. In constrast, 2D arrays have a certain pattern of elements in two dimensions. This leads to the possibility to steer, bend, and focus waves within the half-space in front of the phased array transducer. In echo reception mode, this behavior leads to the ability to obtain 3D positioning information of obstacles. The position of the obstacle can be described in spherical coordinates with the radial distance, the polar angle, and the azimuthal angle. An overview of signal processing with focus on non-destructive testing (NDT) is given in [30]. The process of spatial filtering the sensor data is called beamforming [31]. To obtain the previous described functionality, the single transducer elements are required to work independently [32]. The property of cross-coupling [32], also known as crosstalk [33], characterizes that the elements do not work independently. In the literature, it is shown that cross-coupling between array elements leads to a loss in resolution [34–36]. In [37], the directivity pattern of a linear array influenced by interaction between the transducer elements is investigated. [38] presents a basic model for cross-coupling included signals and the effect on the directivity pattern. The reduction of cross-coupling is one of the major design challenges in ultrasonic transducer arrays. Firstly, this section reviews studies in design and fabrication of linear and 2D arrays presented in the literature. Furthermore, a focus is set on investigations in the mechanisms of cross-coupling and strategies to reduce it. Generally, cross-coupling effects can be classified by the domain in which they emerge, cf. Fig. 1.4. Thus, cross-coupling is divided in mechanical cross-coupling and electrical cross-coupling. As this work is only related to the mechanical domain, effects caused by electrical cross-coupling are not considered. Within the mechanical domain, cross-coupling can be divided by the paths of inter-element coupling which are the acoustic load medium, the common backing of the single transducer elements, and an optional common matching layer. Dependent on

- operating frequency,
- acoustic load medium, and
- individual setup of the phased array transducer,

the predominant mechanism varies.

In 1979, Swartz and Plummer [39] present a polymer based ultrasonic transducer array employing polyvinylidene fluoride (PVF_2) as electro-mechanical coupling element. A quite similar polymer based micromachined diaphragm structure for integrated ultrasound transducer arrays is presented in the studies of Mo et al. [40]. The cross-coupling of this structure is investigated in [41].

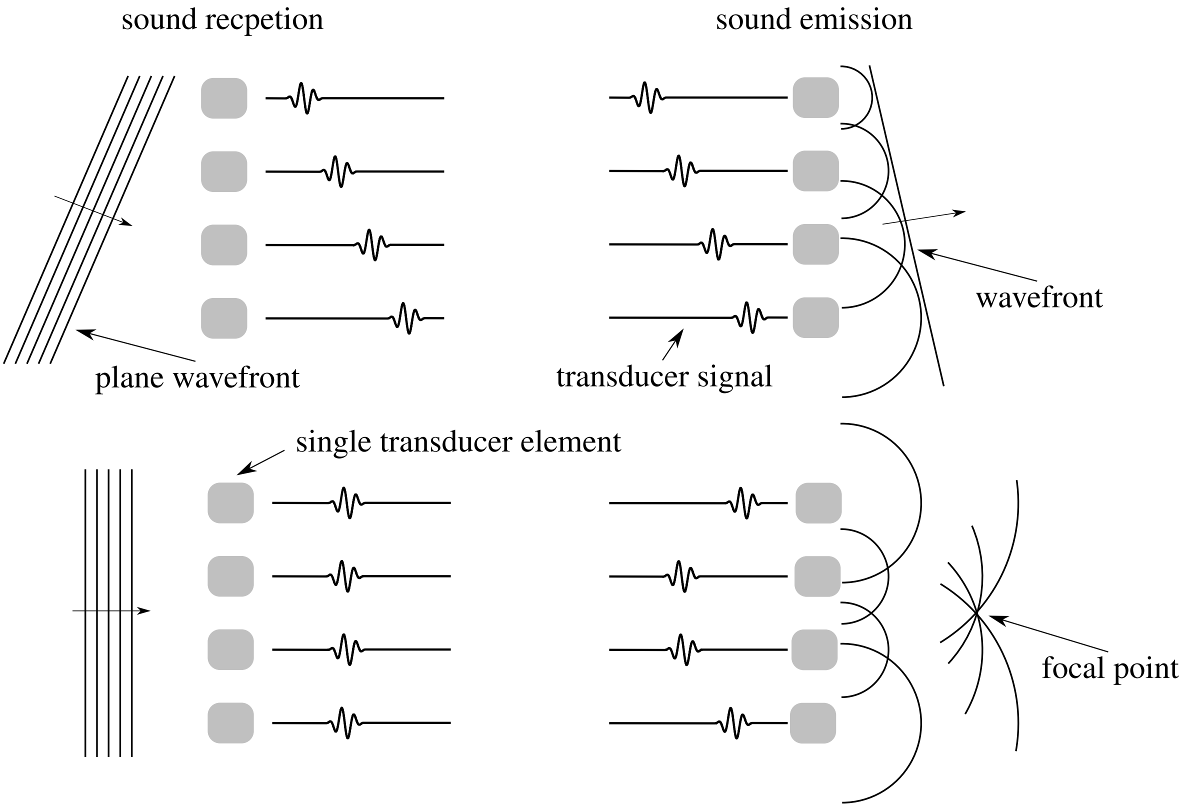

Figure 1.3: Phased array transducer consisting of multiple single transducer elements. Signals with various time delays in sound reception and sound emission mode. Thus, angle information can be obtained from an incoming wavefront and emitted waves can be steered (top) and focused (bottom), cf. [30]

Therefore, different silicon backings are designed. The investigation shows best results for array elements having a separated backing for each array element. In [42], piezoelectric multilayer ceramics are used to form 2D arrays for medical applications. The transducer performance is predicted accurately with 3D finite element analysis. PZT thin film elements are employed in [43]. Yen et al. [44] present a study on building a 2D array with a large count of elements consisting of two layers of perpendicular 1D arrays. One array is used for sound emission while the other one is used for sound reception. An ultrasonic phased array for surround sensing is presented by Harput and Bozkurt [45]. Therefore, the array device uses six single ultrasonic transducers in a line for emission and four single ultrasonic transducers in a line for reception. The employed electronic device for signal processing is presented in [46]. The beamforming algorithm is performed on a field programmable gate array (FPGA). Further studies on air-coupled, low frequency phased arrays are presented in [47] and [48]. These ultrasonic transducers are realized with piezoelectric crystals. Konetzke et al. [49] present an array of ultrasonic transducers which has no grating lobes.

Therefore, commercially available single element transducers are used to build an array structure. Each transducer is connected with a shrinking tube to an additional layer which represents the final sound emitting and receiving layer. The shrinking tube acts as a waveguide in this construction. In [50], the signal reception performance of this transducer array is investigated. Apart from the previous piezoelectric based transducers, CMUTs show suitable performance to build transducer arrays. Jin et al. [51] report a fabrication technique for surface micromachined ultrasonic immersion transducers. Several issues in this fabrication process, like e.g. membrane formation, vacuum sealing, and metalization are investigated. A CMUT fabricated with the suggested process is characterized in [52].

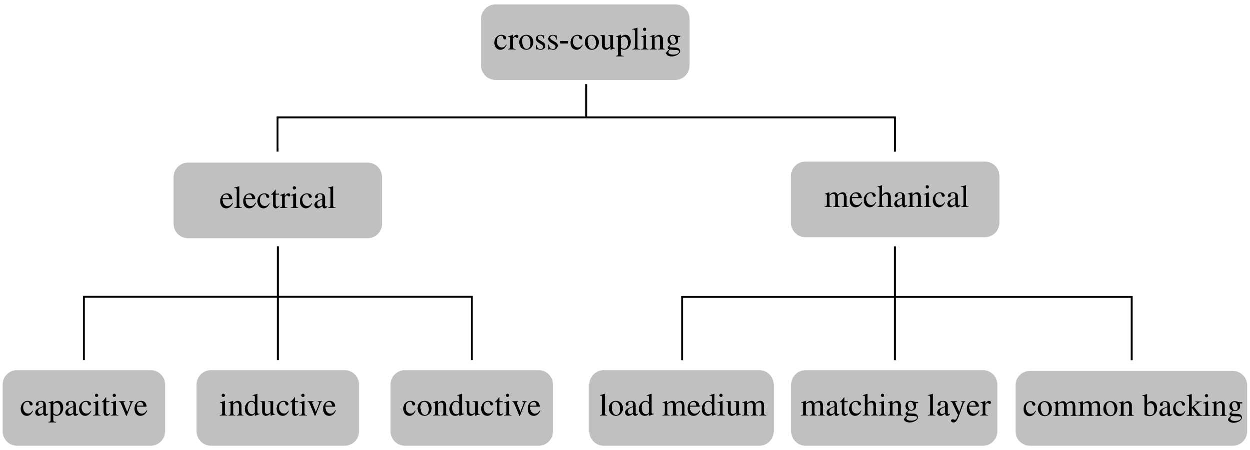

Figure 1.4: Cross-coupling in various domains and media in phased array transducers.

Early studies like [34, 35] and [36] discuss the effect of inter-element cross-coupling in transducer arrays and first methods to reduce it. [32] presents a quantitative theory for cross-coupling in ultrasonic transducer arrays. Surface waves in the backing and in the load medium in front of the transducers are indicated as reason for cross-coupling. This theory assumes a series of uniformly distributed, unbacked transducer elements. The cross-coupling is caused by interaction through a semi-infinite substrate, the solid load medium. First asymmetrical lamb wave A0 mode has been identified as the responsive effect for cross-coupling in a CMUT-array [53]. The first order resonance frequency of the investigated structure is at 2.3 MHz.

Hofer et al. [54] present a computer-aided engineering (CAE) environment for the design of CMUT arrays. The tool takes various nonlinearities into account, such as geometric nonlinearity of the mechanical structures, electrostatic force, and moving body in an electrostatical field. The domains of acoustics, mechanics, and electrostatics are coupled. It is found that the mechanical cross-coupling increases with an increasing backing thickness for the given setup. Furthermore, the acoustical cross-coupling is predominant in the presented investigations. The operating frequency is higher than 200 kHz. In [33], the mechanical cross-coupling through the common backing is focused. A piezoelectric 2D array is investigated with regard to minimize the cross-coupling between the transducer elements. Therefore, various kerf designs between the elements are investigated. Further studies on kerf design and backing design in piezoelectric phased array transducers are presented in [55] and [56]. Ji et al. [57] investigate a lightweight, phase-cancelling backing for the application in ultrasonic transducer arrays. The backing consists of different material layers with various thicknesses and particular acoustics impedances. The proposed backing structure can suppress the back-wall echo signals which lead to the possibility to reduce the thickness of the backing. Yang et al. [58] investigate the influence of different pillars on cross-coupling in PZT 1-3 composite arrays. Arrays with operating frequency at 10 MHz and 15 MHz are presented. It is shown that a pseudo-random pillar shows best results with respect to cross-coupling.

Khuri-Yakub et al. [59] present a study on cross-coupling in CMUT arrays with operating frequency in the range of a couple MHz. Employing finite element analysis, the dispersive guided mode propagating in the fluid-solid interface is identified as the main cross-coupling mechanism in the investigated setup. Stytsenko et al. [60] investigate acoustic cross-coupling through the acoustic load medium in piezoelectric based, linear arrays. It is shown that cross-coupling through the acoustic load medium effects the beam patterns and the frequency response substantially in the investigated uniformly-spaced array of narrow strip elements. Roh and Khuri-Yakub [61] investigate an underwater CMUT array using FEA. The influence of several structural variations of the silicon wafer is investigated. The setup uses a couple of transducer elements as transmitter while another couple of transducer elements act as receiving array. While a trench between these groups of elements does not show any evidence of cross-talk level reduction, a wall was found to be the most promising method to reduce the cross-coupling. In contrary to this results, Roh and Kim [62] found kerfs being an effective method to reduce crosstalk in PMUT arrays for a different array setup.

In sound transmission mode, cross-coupling can be reduced with appropriate excitation signals. Cugnet et al. [63] use the finite element method to optimize the far-field pattern by applying an electrical correction signal to the neighbor elements. Bybi et al. [64] investigate the active cancellation of acoustic cross-coupling between array transducer elements through the load medium in harmonic [65, 66] and transient regime [64]. The active cancellation is also realized by applying an electrical correction signal to the neighbor elements. Meng et al. [67] present a method to reduce cross-coupling when using multiple ultrasonic sensors in transmission mode. Therefore, a novel form of the excitation signal, called frequency hopping pseudo-random pulse width modulation, is presented. The signal includes multiple variable-width and fixed-amplitude pulses. Another approach is presented in [68] and [69]. In order to reduce inter-element cross-coupling in CMUT arrays in transmission mode, modified waveforms were transmitted at adjacent elements. The waveforms are calculated employing a transfer function matrix approach.

1.1.3 Acoustic metamaterial

In 1968, Veselago [70] firstly mentioned the idea of material with negative dielectric constant ε and negative magnetic permeability μ at the same time. This results in a negative index of refraction. Due to a lack of such materials, the idea of Veselago [70] remained a theoretical study. In the 1990s, first structures with the previous mentioned properties are presented by Pendry et al. [71]. The term metamaterial is coined by John Pendry within the last three decades [72]. It describes structures which exhibit properties that are not found in nature [73]. The metamaterial consists of sub-units with a scale much smaller than the entire structure. Thus, effective properties of the whole structure are attained which cannot be found in nature [74].

In the field of sound and vibration, Liu et al. [75] present a sonic crystal with a lattice constant being at a subscale of the sonic wavelength of the exhibited band gap for the first time. Therefore, rigid spheres of lead were coated with rubber and placed in an epoxy plate. Some years before, Strasberg and Feit [76] investigates the effect of a multitude of small sprung masses attached to a large main structure and their influence on the vibrational behavior. This is basically what is described as the principle of tuned resonators in literature.

During the last two decades, a lot of research has been carried out in the field of acoustic metamaterial. Thus, various terms are used to describe the investigated structures. However, certain terms are used with different meaning. Banerjee [77] distinguishes between metamaterial on the one hand and phononic and photonic crystals on the other hand. In the group of metamaterial, the effect couples to waves with resonances and the internal dimensions of the metamaterial are independent from the wavelength they interact with. In contrast, phononic and photonic crystals are characterized by effects which are strongly coupled to the periodicity of the structure, like Bragg scattering or some other kind of periodic media concept. With respect to the previously discussed definition of metamaterial as structures which exhibit properties that are not found in nature, it seems reasonable to handle both groups described by Banerjee [77] with the term of metamaterial. In the field of vibro-acoustics, the usage of the term stop band material or band gap material seems suitable as it describes the resulting property. However, it should be pointed out that it is a property caused by the structural design and not by the pure material properties themselves.

Most of the metamaterials investigated in literature consist of periodic structures. Nonetheless, Kaina et al. [78] demonstrated the effect of randomly distributed resonant structures in the field of electromagnetic metamaterials. A similar investigation is carried out for acoustic metamaterial in the studies of Rupin et al. [79]. Therefore, long aluminum rods are attached to an aluminum plate in ordered (periodic) and disordered (non-periodic) form. The band gap behavior, also known as stop band behavior, is attained by the resonance of the aluminum rods. It is shown that appropriate wave attenuation can be achieved by both, ordered and disordered resonant substructures. Sugino et al. [80] investigate the band gap behavior in resonant metamaterial. Uniform distributed and non-uniform distributed resonators are investigated.

Claeys et al. [81] investigate interference stop bands as well as resonant stop bands regarding their perspective to create low frequency stop bands. It is shown that periodic tuned resonators are suitable to create low frequency stop bands with high wave attenuation. The stop band arises at the resonance frequency of the tuned resonator as long as the resonance frequency is below the standing wave frequency of the unit cell. The unit cell describes the smallest, periodically repeated structure.

Olsson III et al. [82] present a microfabricated acoustic crystal in order to obtain an acoustic band gap. Therefore, tungsten scatters are included in a SiO_2 matrix. A band gap around 67 MHz is achieved. In [83], a study on hybrid elastic solids is presented. Therefore, components of soft silicone rubber, hard silicone rubber, and steel are placed in a foam host. The presented structure shows unusual acoustic properties. Within a high frequency band, the elastic metamaterial behaves in a fluid like manner. In a lower frequency band, the solid shows unusual anisotropy. In certain directions it behaves like a fluid, while in a certain other direction the structure behaves like an incompressible solid. Xiao et al. [84] investigate the propagation of flexural waves in thin plates. It is shown that wave propagation can be attenuated by locally attached spring-mass resonators. The behavior of different excitations is investigated with regard to the vibration transmission. In [85], similar structures are investigated with regard to the sound transmission loss (STL). Furthermore, it is demonstrated that the frequency band of increased STL in a metamaterial-based plate can be broadened significantly by replacing a single resonator in each unit cell with multiple smaller, appropriately damped resonators. Oudich et al. [86] present a negative effective mass density of an acoustic metamaterial plate decorated with low frequency resonant pillars. In [87], the effect of these acoustic metamaterials is investigated with regard to sound mitigation. In the research of Claeys et al. [88], the acoustic radiation efficiency of stop band materials based on local resonance is studied. Song et al. [89] investigates the stop band behavior of a sandwich plate with a stepped resonator. The influence of the stop band design on the sound transmission properties is studied.

A widely known demonstrator for acoustic isolation based on resonant acoustic metamaterial is presented by Claeys et al. [90]. The presented stop band material is extended with microslots in the study of Ruiz et al. [91]. As a result, acoustic absorption is achieved by viscous losses. Lewińska et al. [92] investigate locally resonant acoustic metamaterial with viscoelastic material behavior. A generalized Maxwell model is employed to take the nonlinear, frequency dependent material properties into account. In [93], the influence of thermal stresses on the band structure of periodic metamaterials is investigated. It is shown that thermal stresses have significant, nonlinear effects on the frequency band structure. Kruisová et al. [94] investigate the band gap behavior of 3D-printed periodic ceramic microlattices. Band gaps in the range of several MHz are obtained.

Peng et al. [95] present a theoretical investigation on multi-stop band material. It is designed by adding two-degree of freedom mass-spring systems to a plate. Chen et al. [96] present a possibility to widen the band gap of resonant sonic metamaterials by a stacked structure. Therefore, coated-steel rods are stacked orthogonally and are embedded layer by layer in an epoxy matrix. The studies [97] and [98] investigate the attenuation of structural vibrations in a duct by applying locally resonant metamaterial. It is shown that the combination of different resonator configurations in one structure can lead to combined stop bands if they are appropriately designed.

Trainiti et al. [99] investigate the wave propagation in structures with 1D and 2D periodicity. It is shown that undulation in beams and plates is an appropriate design parameter to obtain band gap behavior. In order to maximize the frequency band gap, optimization algorithms are employed to Bernoulli-Euler beams in the studies of Olhoff et al. [100]. It is shown that maximization of the frequency gap leads to significant design periodicity within the shape of the Bernoulli-Euler beams. Lu et al. [101] present a work on topology optimization of acoustic metamaterial using local resonance in a two-dimensional case. The objective is to minimize the effective bulk modulus at certain frequencies. As a result, negative effective bulk modulus is reached at a target frequency. Another study on a design method for locally resonant sonic materials using topology optimization algorithms is presented by Matsuki et al. [102]. He and Kang [103] present a study on gradient-based topology optimization of material with microstructural configurations to obtain directional wave propagation. Therefore, partial band gaps are maximized in two-dimensional, periodic structures.

Li et al. [104] build a sound absorbing metasurface by coupling multiple Helmholtz resonators. Over 99 % energy absorption is reached with a thickness of $\lambda/20$. Wang et al. [105] investigate the manipulation of reflected wavefront by structured phase gradient metasurfaces. Therefore, circular-holed cubes are placed on a surface. It is shown that the hole diameter is an effective design parameter for the presented metasurface. The use of the metasurface is demonstrated in simulations for structures with anomalous reflections, an acoustic focusing lens, and an acoustic carpet cloak. In the studies of Ma et al. [106], a membrane-type acoustic metamaterial (MAM) is presented in which the membrane is decorated with a platelet. The presented unit attains over 99 % acoustic absorption coefficient at a certain frequency. Assembling different units closely together results in nearly total acoustic absorption at various frequencies. Furthermore, the structure can be employed as power conversion device from acoustical to electrical energy. A 3D-printed membrane type-acoustic metamaterial is realized by flexible thermoplastic material in the studies of Ba et al. [107]. In the center of the membrane a center mass is placed. It is shown that the frequency ranges with high absorption can be tuned by geometrical parameters of the added mass. Langfeldt et al. [108] present a study on MAM which has adjustable sound transmission properties. Therefore, the MAM is inflatable with pressurized air to adjust its acoustic properties. Wang et al. [109] present a MAM for sound absorption. The motion of the membrane is constrained with a stick in the center position. The achieved band gaps are broaden compared to conventional MAMs. The position, shape, and thickness of the constraining stick are appropriate design parameters to influence the vibration modes which are related to peaks and dips in sound absorption.

The influence of defects in 2D periodic structures is investigated in [110]. Another study on point defects in thin plates with 2D periodic structures is presented by Yao et al. [111]. It is shown that the defect modes, existing in the first band gap, are strongly dependent on the size of the point defect and the filling fraction of the system. Defect modes are investigated experimentally by applying a fiber Bragg grating to a beam with 1D periodicity in [112].

1.1.4 Fiber reinforced composites

Fiber reinforced composites are known from nature for centuries. Probably the most famous and most used natural fiber reinforced material is wood. It consists mainly of fibers of cellulose and hemicelluloses embedded in a amorphous matrix of lignin [113]. It has been the state of the art material to construct ships, vehicles, weapons, and buildings for centuries. This is due to excellent density to strength ratio. The technique of reinforcing continuous materials with fiber similar material has already been known by the Egyptians. In order to make clay bricks more durable and strong, they were reinforced by straw [114]. The reinforcement of clay bricks with straw was even mentioned in the bible [115, Exodus 5:7].

A uniform definition of the term composite is complex. According to Rösler et al. [116], modern composites are characterized by the following properties:

- A second, reinforcing phase is embedded in a continuous matrix.
- The matrix and the reinforcing phase are separated before they are combined in the manufacturing process.
- The reinforcing phase has a scale in the range of micrometer or higher.
- The volume fraction of the reinforcing phase is at least 10%.

Today, fiber reinforced composites are widely used in technical applications in nearly all sectors of engineering such as aerospace, automotive, marine, and industrial equipment to name only a few. Most important fiber materials for technical uses are carbon, glass, and aramid fiber [117]. Nonetheless, there are a lot of materials suitable to form fiber reinforcements depending on the requirements of the composite, cf. [117]. A wide overview on fiber materials, fiber construction and fabric construction of textiles is given in [118] and [117]. In this work, only balanced, plain woven fabrics and non-crimp fabrics of carbon fiber are relevant. Although there is a lot of literature in the field of composites, in this thesis, only a small number of publications with focus on modeling mechanical properties of composites are reviewed. A well-known possibility to describe the material properties of fiber reinforced composites is the so-called classical laminate theory. A comprehensive literature is given by Schürmann [119]. Halpin [120] presents a method to approximate the stiffness and expansion of oriented short fiber composites. A closer look is given in [121]. Applying this theory, the non-uniform strain in the matrix of fiber reinforced composites can be taken into account. Foye [122] presents a method to calculate the transverse Poisson's ratio of composites using the material data of the single components. In Jacquet et al. [123], it is demonstrated how to use the rule of mixture in order to obtain transverse and shear moduli of unidirectional composite material. Akkerman [124] adopts the mechanics of unidirectional laminates to predict the mechanical properties of composites with balanced, woven fabrics. Therefore, the mechanical behavior of balanced, woven fabric is represented by orthogonal plies with manipulated properties. In [125], a method to predict the shear modulus of orthotropic materials is presented. Pal and Haseebuddin [126] present a study on estimation of elastic properties of fiber reinforced composites using finite element analysis. Therefore, the representative volume element is investigated in FEA. Afterwards, the results are compared with the analytical solution applying the rule of mixture and the semi-analytical solution of Halpin-Tsai.

1.2 Contribution of this work

This work contributes to the field of structural dynamics and acoustics of ultrasonic transducers. The research questions can be formulated by

1. How to achieve highly anisotropic directivity patterns in ultrasonic transducers with rotationally symmetric geometry? (**Paper A**)
2. How to operate ultrasonic transducers having one electro-mechanical coupling element at two or more frequencies with appropriate sound radiation properties? (**Paper B**)
3. How to reduce mechanical cross-coupling in compact, low frequency, air-coupled ultrasonic array transducers? (**Paper C**)

In order to investigate these questions, three papers are appended to this thesis. Each paper addresses one of the research question. The results offer the possibility to achieve ultrasonic transducers with an increased performance compared to state of the art concepts.

Paper A The approach of locally structured fiber reinforcements is suggested and investigated. The fiber reinforcement is used as a design space to achieve sections with different material properties in a monolithic structure. Different designs and textile fabrics are considered to achieve ultrasonic transducers with anisotropic directivity patterns. The approach is investigated in a generic model consisting of the head of an ultrasonic sensor. In order to conduct numerical simulations, an appropriate material description is required. The employed material model is presented in detail. It allows the prediction of the homogenized composite material properties knowing the material properties of the single components and the fiber volume ratio of the structure. The presented approach of locally structured fiber reinforcements is validated in experimental testing.

Paper B In this study, a novel concept to achieve multi-frequency ultrasonic transducers is presented. It is based on the modification of the resulting operational deflection shape of the sound radiating surface in a certain frequency range. This is achieved by the introduction of spatially distributed stop band material. In a simplified, generic model of an ultrasonic transducer with only one electro-mechanical coupling element, the approach is examined. It is found that suitable sound radiating properties can be achieved at two distinctive operating frequencies. Furthermore, it is shown that the second operating frequency and the corresponding operational deflection shape are nearly independent from the boundary conditions. They rather depend on the frequency of the stop band exhibited by the stop band material.

Paper C Cross-coupling in compact, low frequency, air-coupled phased array transducers is investigated in this paper. The focus is on mechanical cross-coupling caused by a common backing.

Initially, the relation between backing thickness and cross-coupling is studied. It is found that weak cross-coupling can be interpreted as a strong cancellation effect between the single bending elements of the phased array transducer. This cancellation effect is achieved in case the in-phase and out-of-phase mode of the bending elements exhibit small differences in eigenfrequency. Consequently, weak cross-coupling can be achieved by a backing with high stiffness and by avoiding the coincidence of a backing dominated mode with the operating frequency. To overcome this limitation, a novel concept to reduce mechanical cross-coupling is presented. Therefore, 25 beam resonators are added to the downside of the backing. Due to the behavior of the tuned resonators, a stop band is exhibited. Consequently, shear and bending waves cannot freely propagate in the backing. In numerical and experimental investigations, it is shown that a major reduction of cross-coupling is achieved in case the operating frequency of the phased array transducer is within the frequency range of the stop band.

Chapter 2

Applied Methods

In this chapter, the methods applied to investigate the dynamic behavior of ultrasonic transducers are introduced. In general, the finite element method is used to achieve numerical results for complex models. Firstly, a brief introduction is given to this method. Afterwards, the wave finite element method is discussed. This approach offers the possibility to analyze periodic structures in a unit cell. In order to approximate the sound radiation behavior of an ultrasonic transducer, the Rayleigh integral is employed. Finally, the applied experimental test methods are described.

2.1 Finite element method

Today, finite element analyses are widely used in the field of engineering. The method is used in the analysis of structural mechanics, fluid mechanics, and heat transfer analysis. The term *finite element* was introduced in 1960 by Clough [127], a pioneer in the development of the finite element method.

The finite element method is an approach to approximate the solution of a boundary value problem [128]. This mathematical problem contains a number of dependent variables which must fit specific conditions at the boundary of the domain. Furthermore, they are governed by a differential equation which has to be satisfied. The dependent variables are called field variables and represent the variables of interest. The boundary conditions are specific values of the field variable (Dirichlet boundary conditions) or its derivatives (Neumann boundary conditions) on the boundary of the domain. To solve the mathematical problem, the boundary value problem needs to be described by a closed-form algebraic expression for every point of the domain. In case of complex geometrical problems, the chance to obtain such an exact closed-form solution is small. Finite element method provides an approach to approximate the solution with high accuracy. First of all, the domain is divided in elements with a finite size. The element consists of exterior nodes and optional interior nodes. Exterior nodes are located on the boundaries of the finite element and can be connected to other elements [128]. In the finite element method, the values of the field variable are calculated at the nodal points of the element. Between the nodal points, the field values are interpolated. Several literature exists explaining the finite element method. In Bathe [129], a comprehensive introduction with focus on the use in structural mechanics is given. The following introduction is based on this work.

2.1.1 Displacement-based formulation

In structural dynamics, a widely used approach is the displacement-based formulation. In order to explain the general approach, an arbitrarily shaped three-dimensional body is assumed, cf. Fig. 2.1. It is described in the stationary coordinate system X, Y, Z. The body is deformed by body forces $\mathbf{f}^{\mathrm{B}}$, $\mathbf{f}^{S}$, surface traction, and concentrated loads $\mathbf{R}^{i}_{\mathrm{C}}$. The vector of the external loads and forces is given by

$$\mathbf{f}^{\mathrm{B}} = \begin{bmatrix} f^{\mathrm{B}}_{X} \\ f^{\mathrm{B}}_{Y} \\ f^{\mathrm{B}}_{Z} \end{bmatrix} \quad \mathbf{f}^{S} = \begin{bmatrix} f^{S}_{X} \\ f^{S}_{Y} \\ f^{S}_{Z} \end{bmatrix} \quad \mathbf{R}^{i}_{\mathrm{C}} = \begin{bmatrix} \mathbf{R}^{i}_{\mathrm{C}X} \\ \mathbf{R}^{i}_{\mathrm{C}Y} \\ \mathbf{R}^{i}_{\mathrm{C}Z} \end{bmatrix} \quad . \tag{2.1}$$

The displacement of the body caused by the loads and forces is denoted by

$$\mathbf{U} = \begin{bmatrix} U \\ V \\ W \end{bmatrix} \quad . \tag{2.2}$$

The strains ε are related to the displacements $\mathbf{U}$ as follows

$$\varepsilon^{\mathrm{T}} = [\varepsilon_{XX} \quad \varepsilon_{YY} \quad \varepsilon_{ZZ} \quad \gamma_{XY} \quad \gamma_{YZ} \quad \gamma_{ZX}] \quad , \tag{2.3}$$

with

$$\varepsilon_{XX} = \frac{\partial U}{\partial X} \quad , \quad \varepsilon_{YY} = \frac{\partial V}{\partial Y} \quad , \quad \varepsilon_{ZZ} = \frac{\partial W}{\partial Z} \quad , \tag{2.4}$$

and

$$\gamma_{XY} = \frac{\partial U}{\partial Y} + \frac{\partial V}{\partial X} \quad , \quad \gamma_{YZ} = \frac{\partial V}{\partial Z} + \frac{\partial W}{\partial Y} \quad , \quad \gamma_{ZX} = \frac{\partial W}{\partial X} + \frac{\partial U}{\partial Z} \quad . \tag{2.5}$$

The constitutive relation for linear elastic material following Hooke's law is stated by

$$\tau = \mathbf{C}\varepsilon \quad , \tag{2.6}$$

where C is a fourth-order stress-strain material tensor. Considering initial stresses of the body, τ is expressed by

$$\tau = \mathbf{C}\varepsilon + \tau_{\text{initial}} \quad . \tag{2.7}$$

The displacement-based formulation employs the principle of virtual displacements, also known as the principle of virtual work. Thus, for small virtual displacements, the total internal virtual work equals the total external work. This is stated by

$$\int_{\Omega} \bar{\varepsilon}^{\mathrm{T}} \tau \mathrm{d}\Omega = \int_{\Omega} \bar{\mathbf{U}}^{\mathrm{T}} \mathbf{f}^{\mathrm{B}} \mathrm{d}\Omega + \int_{S} \bar{\mathbf{U}}^{S\mathrm{T}} \mathbf{f}^{S} \mathrm{d}S + \sum_{i} \bar{\mathbf{U}}^{i\mathrm{T}} \mathbf{R}_{\mathrm{C}}^{i} \quad , \tag{2.8}$$

where the left-hand side and right-hand side represent the internal and external virtual work, respectively. Ω denotes the domain which is physically represented by the body, cf. Fig. 2.1. The virtual quantities are denoted with a bar, e.g. virtual displacement $\bar{U}$.

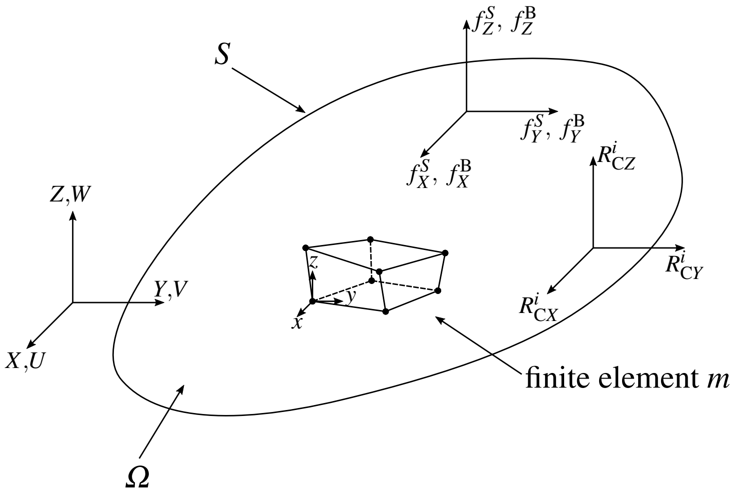

Figure 2.1: Three-dimensional body with finite element, based on [129].

Assuming the body now as assembly of N finite element nodal points, the displacement $\mathbf{u}^{(m)}$ of the finite element m expressed in its local coordinate system $x,\ y,\ z$ is

$$\mathbf{u}^{(m)}(x,y,z) = \mathbf{H}^{m}(x,y,z)\hat{\mathbf{U}} \quad , \tag{2.9}$$

where $\mathbf{H}^m$ and $\hat{\mathbf{U}}$ represent the displacement interpolation matrix and the vector of all nodal displacements, respectively. Consequently, the strain relations are obtained by

$$\varepsilon^{(m)}(x,y,z) = \mathbf{B}^{m}(x,y,z)\hat{\mathbf{U}} \quad , \tag{2.10}$$

with $\mathbf{B}^m$ being the strain-displacement matrix. The stresses $\tau^{(m)}$ within the finite element can be described by

$$\tau^{(m)} = \mathbf{C}^{(m)}\varepsilon^{(m)} + \tau^{(m)}_{\text{initial}} \quad . \tag{2.11}$$

Hence, $\mathbf{C}^{(m)}$, $\varepsilon^{(m)}$, and $\tau^{(m)}_{\text{initial}}$ represent the stress-strain material tensor of the element, the elemental strain, and the initial stress of the finite element m, respectively. Considering the principle of virtual work for each element m leads to

$$\begin{aligned}
&\sum_m \int_{\Omega^{(m)}} \bar{\varepsilon}^{(m)\mathrm{T}} \tau^{(m)} \mathrm{d}\Omega^{(m)} = \dots \\
&\qquad = \sum_m \int_{\Omega^{(m)}} \bar{\mathbf{u}}^{(m)\mathrm{T}} \mathbf{f}^{\mathrm{B}(m)} \mathrm{d}\Omega^{(m)} + \sum_m \int_S \bar{\mathbf{u}}^{S(m)\mathrm{T}} \mathbf{f}^{S(m)} \mathrm{d}S^{(m)} + \sum_i \bar{\mathbf{u}}^{i\mathrm{T}} \mathbf{R}^i_{\mathrm{C}} \quad .
\end{aligned} \tag{2.12}$$

The principle of virtual work is the weak formulation of the equation of motion as shown in [130]. Inserting Eq. (2.9), Eq. (2.10), and Eq. (2.11) with the assumption of virtual displacements into Eq. (2.12) leads to

$$\begin{aligned}
\bar{\hat{\mathbf{U}}}^{\mathrm{T}} \left[\sum_m \int_{\Omega^{(m)}} \mathbf{B}^{(m)\mathrm{T}} \mathbf{C}^{(m)} \mathbf{B}^{(m)} d\Omega^{(m)} \right] \hat{\mathbf{U}} = & \bar{\hat{\mathbf{U}}}^{\mathrm{T}} \left[\left\{ \sum_m \int_{\Omega^{(m)}} \mathbf{H}^{(m)\mathrm{T}} \mathbf{f}^{\mathrm{B}(m)} \mathrm{d}\Omega^{(m)} \right\} \right. \\
& + \left\{ \sum_m \int_{S_1^{(m)} \dots S_Q^{(m)}} \mathbf{H}^{S(m)\mathrm{T}} \mathbf{f}^{S(m)} \mathrm{d}S^{(m)} \right\} \\
& \left. - \left\{ \sum_m \int_{\Omega^{(m)}} \mathbf{B}^{(m)\mathrm{T}} \tau^{(m)}_{\text{initial}} \mathrm{d}\Omega^{(m)} \right\} + \mathbf{R}_{\mathrm{c}} \right] \quad ,
\end{aligned} \tag{2.13}$$

where the surface displacement interpolation matrices $\mathbf{H}^{S(m)\mathrm{T}}$ are obtained from the displacement interpolation matrices $\mathbf{H}^{(m)}$ [129]. $S_1^{(m)} \dots S_Q^{(m)}$ denotes the surface of the body. The vector $\mathbf{R}_{\mathrm{c}}$ contains all loads applied to the nodes of the body. Hence, the i^{th} component of $\mathbf{R}_{\mathrm{c}}$ contains the concentrated force corresponding to the i^{th} displacement component in $\hat{\mathbf{U}}$ [129]. By introducing the identity matrix **I** for the virtual displacement $\bar{\hat{\mathbf{U}}}$, Eq. (2.13) can be written as

$$\mathbf{K}\hat{\mathbf{U}} = \mathbf{R} \quad , \tag{2.14}$$

which is the equilibrium equation in the static case. **K** represents the stiffness matrix of the finite element assembly and is obtained by

$$\mathbf{K} = \sum_m \int_{\Omega^{(m)}} \mathbf{B}^{m\mathrm{T}} \mathbf{C}^m \mathbf{B}^{(m)} \mathrm{d}\Omega^{(m)} \quad . \tag{2.15}$$

The load vector **R**

$$\mathbf{R} = \mathbf{R}_\mathrm{B} + \mathbf{R}_S - \mathbf{R}_\mathrm{initial} + \mathbf{R}_C \tag{2.16}$$

consists of body forces $\mathbf{R}_\mathrm{B}$

$$\mathbf{R}_\mathrm{B} = \sum_m \int_{\Omega^{(m)}} \mathbf{H}^{(m)\mathrm{T}} \mathbf{f}^{\mathrm{B}(m)} \mathrm{d}\Omega^{(m)} \quad , \tag{2.17}$$

surface traction $\mathbf{R}_S$

$$\mathbf{R}_S = \sum_m \int_{S_1^{(m)} \ldots S_Q^{(m)}} \mathbf{H}^{S(m)\mathrm{T}} \mathbf{f}^{S(m)} \mathrm{d}S^{(m)} \quad , \tag{2.18}$$

initial stress $\mathbf{R}_{initial}$

$$\mathbf{R}_\mathrm{initial} = \sum_m \int_{\Omega^{(m)}} \mathbf{B}^{(m)\mathrm{T}} \tau_\mathrm{initial}^{(m)} \mathrm{d}\Omega^{(m)} \quad , \tag{2.19}$$

and concentrated loads $\mathbf{R}_C$. Employing the D'Alembert's principle for dynamic analysis, the inertia force is included to the body forces by

$$\mathbf{R}_\mathrm{B} = \sum_m \int_{\Omega^{(m)}} \mathbf{H}^{(m)\mathrm{T}} \left[\mathbf{f}^{\mathrm{B}(m)} - \rho^{(m)} \mathbf{H}^{(m)} \hat{\hat{\mathbf{U}}} \right] \mathrm{d}\Omega^{(m)} \quad , \tag{2.20}$$

with $\rho^{(m)}$ and $\hat{\hat{\mathbf{U}}}$ being the mass density of the element and nodal point accelerations, respectively. The equation of equilibrium for dynamic analysis can then be written as

$$\mathbf{M}\hat{\hat{\mathbf{U}}} + \mathbf{K}\hat{\mathbf{U}} = \mathbf{R} \quad . \tag{2.21}$$

M represents the mass matrix of the body and can be obtained by

$$\mathbf{M} = \sum_m \int_{\Omega^{(m)}} \rho^{(m)} \mathbf{H}^{(m)\mathrm{T}} \mathbf{H}^{(m)} \mathrm{d}\Omega^{(m)} \quad . \tag{2.22}$$

Taking energy dissipation into account, a velocity dependent part is included in Eq. (2.20)

$$\mathbf{R}_{\mathrm{B}} = \sum_m \int_{\Omega^{(m)}} \mathbf{H}^{(m)\mathrm{T}} \left[\mathbf{f}^{\mathrm{B}(m)} - \rho^{(m)} \mathbf{H}^{(m)} \ddot{\hat{\mathbf{U}}} - \kappa^m H^{(m)} \dot{\hat{\mathbf{U}}} \right] \mathrm{d}\Omega^{(m)} \quad , \tag{2.23}$$

which leads to

$$\mathbf{M}\ddot{\hat{\mathbf{U}}} + \mathbf{C}\dot{\hat{\mathbf{U}}} + \mathbf{K}\hat{\mathbf{U}} = \mathbf{R} \quad . \tag{2.24}$$

It is worth to point out that in Eq. (2.20) $\mathbf{f}^{B(m)}$ no longer contains inertia forces and in Eq. (2.23) $\mathbf{f}^{B(m)}$ no longer contains inertia forces and velocity-dependent damping forces. **C** denotes the damping matrix including the elemental damping property parameter $\kappa^{(m)}$

$$\mathbf{C} = \sum_m \int_{\Omega^{(m)}} \kappa^{(m)} \mathbf{H}^{(m)\mathrm{T}} \mathbf{H}^{(m)} \mathrm{d}\Omega^{(m)} \quad . \tag{2.25}$$

2.1.2 Analysis techniques

The finite element formulation, as introduced in Section 2.1.1, allows various analyses in order to characterize the investigated structure. In the field of vibration analysis, the extraction of vibration modes is desired in order to characterize the general dynamic behavior of the structure. If damping is neglected, the vibration mode can be obtained from the generalized eigenvalue problem which is stated as

$$(-\mu \mathbf{M} + \mathbf{K})\phi = 0 \quad , \tag{2.26}$$

with μ being the eigenvalues which are related by $\mu = \omega^2$ to the angular eigenfrequency and ϕ being the corresponding eigenvector. Assuming r solutions of the generalized eigenvalue problem, it can be written as

$$(-\Lambda \mathbf{M} + \mathbf{K})\Phi = 0 \quad , \tag{2.27}$$

with Λ denoting a diagonal matrix with the dimension $r \times r$ containing the eigenvalues and Φ containing the corresponding eigenvectors $\Phi = [\phi_1,\ \phi_2, \ldots \phi_r]$. In practical use, often a certain number of eigenvalues and corresponding eigenvectors are the subject of interest rather than the entire number r of possible solutions. In order to obtain the desired solutions, an abundance of numerical solving approaches exists. Two very common approaches are the Lanczos iteration method [131–134] and the subspace iteration method, also know as Bathe subspace iteration method [135, 136, 129, 137].

In order to obtain the dynamic response of a system to a load, the equilibrium equation Eq. (2.24) has to be solved. Similar to the generalized eigenvalue problem, a great amount of approaches to solve this numerical problem effectively are available. An effective method to solve this problem is the approach of mode superposition. Basically, the differential equations of motion are projected onto the modes obtained from the generalized eigenvalue problem. Thus, n independent differential equations of motion of the form

$$\ddot{z}_i + 2\xi_i\omega_i\dot{z} + \omega_i^2 z_i = \frac{1}{m_i} f_i \quad , \tag{2.28}$$

with z_i, ξ_i, m_i, and f_i denoting the generalized modal displacement of the i^{th} mode, the fraction of critical damping, the generalized modal mass, and the modal load, respectively. In case of $n = r$,

$$\hat{\mathbf{U}} = \sum_i^n \phi_i z_i \tag{2.29}$$

gives the exact solution for the displacement $\hat{\mathbf{U}}$. Due to the nature of finite element methods, the solution is an approximation as pointed out previously. Thus, often it is not necessary to consider all pairs of eigenvalue and the corresponding eigenvectors to achieve an appropriate approximation of the dynamic behavior of the investigated structure. Consequently, the computational effort can be reduced by $n \ll r$. The number of n which is employed in the mode superposition approach finally depends on the investigated structure, applied loads, and required accuracy. It can by determined in a convergence study. A more detailed elaboration of the method is discussed in [129].

2.2 Wave finite element method

Periodic structures consist of a large amount of identical structure elements. The smallest structure repeated is called unit cell. In order to reduce the computational effort, the wave propagation properties are characterized in the unit cell rather than in the entire structure. The wave propagation behavior is described by the dispersion relations in the unit cell. The wave finite element method offers a possibility to achieve the dispersion relations in an unit cell employing classical finite element method with Floquet-Bloch boundary conditions [138]. In the presented work, two-dimensional periodicity is most important and is therefore discussed in this section. The theory of the approach is discussed also in the appended **Paper B** [139].

Employing the Floquet-Bloch theorem, for time harmonic dependence $\mathrm{e}^{\mathrm{i}wt}$, the response function ψ can be described by

$$\psi = W\mathrm{e}^{\mathrm{i}(\omega t - k_x x - k_y y)} \quad , \tag{2.30}$$

with W, k_x, and k_y being a function through the solid thickness and the component of the wavenumber in x- and y-direction, respectively. In this work, the wavenumber k is considered as real rather than complex or purely imaginary. Thus, it describes the wave propagation in the absence of damping. Considering a four node-element as given in Fig. 2.2, the vector of generalized displacements $\mathbf{q}$ is defined by

$$\mathbf{q} = [\mathbf{q}_1 \quad \mathbf{q}_2 \quad \mathbf{q}_3 \quad \mathbf{q}_4]^{\mathrm{T}} \quad . \tag{2.31}$$

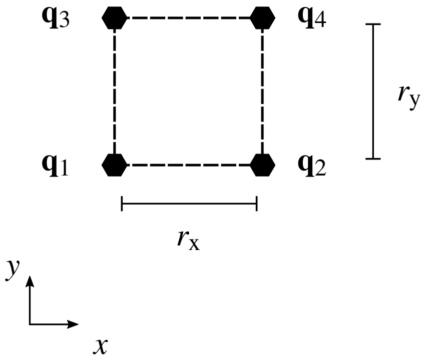

Figure 2.2: Generalized displacements $\mathbf{q}$ at various points in case of two-dimensional periodicity [139].

According to Bloch theorem stated in Eq. (2.30), the generalized displacements are related to $\mathbf{q}_1$ by [140]

$$\begin{aligned} \mathbf{q}_2 &= \lambda_x \mathbf{q}_1 \quad , \\ \mathbf{q}_3 &= \lambda_y \mathbf{q}_1 \quad , \\ \mathbf{q}_4 &= \lambda_x \lambda_y \mathbf{q}_1 \quad , \end{aligned} \tag{2.32}$$

with

$$\begin{aligned} \lambda_x &= \mathrm{e}^{-\mathrm{i} k_x \cdot r_x} \qquad \text{and} \qquad \mu_x = k_x r_x \quad , \\ \lambda_y &= \mathrm{e}^{-\mathrm{i} k_y \cdot r_y} \qquad \text{and} \qquad \mu_y = k_y r_y \quad , \end{aligned} \tag{2.33}$$

where $r_{x,y}$ and $\mu_{x,y}$ denote the length of the periodic lattice and the propagation constant in the direction of periodicity, respectively. In matrix notation it is possible to write

$$\mathbf{q} = \Lambda_\mathrm{R} \mathbf{q}_1 \quad , \tag{2.34}$$

with Λ_R being the right reduction matrix

$$\Lambda_\mathrm{R} = [\mathbf{I} \quad \lambda_x \mathbf{I} \quad \lambda_y \mathbf{I} \quad \lambda_x \lambda_y \mathbf{I}]^{\mathrm{T}} \quad . \tag{2.35}$$

The generalized displacements **q** are related to generalized forces **f** in the absence of damping by [141]

$$\left[\mathbf{K}-\omega^2\mathbf{M}\right]\mathbf{q}=\mathbf{f} \quad . \tag{2.36}$$

For free vibration, the sum of forces at nodal point 1 implies

$$\Lambda_\mathrm{L}\mathbf{f}=0 \quad . \tag{2.37}$$

In equivalence to Eq. (2.35), the left reduction matrix is formulated by

$$\Lambda_\mathrm{L}=\begin{bmatrix}\mathbf{I} & \lambda_x^{-1}\mathbf{I} & \lambda_y^{-1}\mathbf{I} & \lambda_x^{-1}\lambda_y^{-1}\mathbf{I}\end{bmatrix} \quad . \tag{2.38}$$

Based on these relations, it is possible to formulate a reduced eigenvalue problem

$$\Lambda_\mathrm{L}\left[\mathbf{K}-\omega^2\mathbf{M}\right]\Lambda_\mathrm{R}\mathbf{q}_1=0 \quad . \tag{2.39}$$

The obtained eigenvalues ω^2 are a function of the propagation constants μ_x and μ_y. Thus, it must be solved for any combination of the propagation constants in the first Brillouin zone $\mu_x,\mu_y=[-\pi,\pi]$ [142]. A typical presentation of the solution is done in three-dimensional surface plots. These surfaces are called dispersion surfaces. They characterize the free wave propagation in the unit cell. Frequency ranges, where no dispersion surface is present, are defined as stop bands or band gaps. In case of symmetric unit cells, the calculation can be reduced from the Brillouin Zone to the irreducible Brillouin Zone or to the contour of the irreducible Brillouin Zone. Thus, the dispersion surfaces are reduced to two-dimensional dispersion curves. The conditions for this reduction are investigated in [143]. The approach of wave finite element method is discussed in detail in [141, 140, 144, 145]

2.3 Sound radiation of plain structures

Sound radiation and sound detection are the two general purposes of an ultrasonic transducer. Thus, the characterization of the radiated sound field is of elementary interest when investigating ultrasonic transducers. Ultrasonic transducers used in automotive applications are desired to provide a flat surface. Furthermore, they are usually embedded in a mounting structure like a car bumper. Considering these boundary conditions, the Rayleigh integral [146] provides a suitable approximation of the sound radiation behavior of an ultrasonic transducer. The theory of the approach is discussed also in the appended **Paper A** [147]. The Rayleigh integral provides exact solutions in the far-field if the following requirements are fulfilled

- the radiating surface is flat,
- the radiator is embedded in a flat, infinite, and rigid baffle.

For $\mathrm{e}^{\mathrm{i}\omega t}$ harmonic time dependence, the Rayleigh integral for a plane surface can be expressed by [148]

$$p(\vec{y}) = \int_{\Gamma} -\mathrm{i}\omega\rho_{\mathrm{f}}\, G(\vec{x},\vec{y})\, v_{\mathrm{f}}(\vec{x})\mathrm{d}\Gamma(\vec{x}) \quad , \tag{2.40}$$

with

$$G(\vec{x},\vec{y}) = \frac{\mathrm{e}^{-\mathrm{i}kr}}{2\pi r} \qquad \text{and} \qquad r = |\vec{x}-\vec{y}| \quad , \tag{2.41}$$

where $\Gamma,\ k,\ \omega,\ v_{\mathrm{f}},\ \rho_{\mathrm{f}},\ \mathrm{i}$ denote the radiating surface, wavenumber, circular frequency, fluid particle velocity, fluid density, and imaginary unit, respectively. In order to solve Eq. (2.40), an approximation in the far-field is considered. To fulfill the far-field assumption, three conditions must hold [149]. Firstly, the distance R between the radiator and the field point has to be much greater than the dimension l of the radiator

$$R \gg l \quad . \tag{2.42}$$

Secondly, the condition

$$\frac{R}{l} \gg \frac{l}{\lambda} \tag{2.43}$$

must be fulfilled. Consequently, the error caused by phase shifts is small. Finally, the wavelength λ should be small compared to the distance between the radiator and field point

$$\lambda \ll R \,. \tag{2.44}$$

Furthermore, a coordinate transformation from Cartesian to spherical coordinates is applied by

$$\begin{aligned} x &= R\sin(\vartheta)\cos(\varphi) \quad , \\ y &= R\sin(\vartheta)\sin(\varphi) \quad , \\ z &= R\cos(\varphi) \quad . \end{aligned} \tag{2.45}$$

Finally, the approximation of the Rayleigh integral is stated by [8]

$$p(R,\vartheta,\varphi) = \frac{\mathrm{i}\omega\rho_{\mathrm{f}}}{2\pi R}\mathrm{e}^{-\mathrm{i}kR} \int_{-l_y\backslash 2}^{l_y\backslash 2} \int_{-l_x\backslash 2}^{l_x\backslash 2} \mathrm{e}^{\mathrm{i}k(x_{\mathrm{Q}}\sin\vartheta\cos\varphi + y_{\mathrm{Q}}\sin\vartheta\sin\varphi)}\, v(x_{\mathrm{Q}},y_{\mathrm{Q}})\, \mathrm{d}x_{\mathrm{Q}}\, \mathrm{d}y_{\mathrm{Q}} \quad . \tag{2.46}$$

In [150], it is shown that the particle velocity distribution on the surface of the structure can be used to estimate the radiated far-field sound pressure. This velocity distribution of the surface can be obtained from a harmonic analysis employing the finite element method. The exact solution of Eq. (2.46) can be calculated employing the nodal velocities of the finite element analysis and the element interpolation functions. Thus, a continuous function of the velocity is derived. However, as Eq. (2.46) is the approximation of the Rayleigh integral, the calculation can be approximated as well. Therefore, it is converted in a discrete formulation and the average surface velocity $\tilde{v}_i$ of each element is employed. This results in

$$p(R,\vartheta,\varphi) = \frac{\mathrm{i}\omega\rho_\mathrm{f}}{2\pi R}\mathrm{e}^{-\mathrm{i}kR}\sum_{j}^{N_s}\mathrm{e}^{\mathrm{i}k(\tilde{x}_{\mathrm{Q}j}\sin\vartheta\cos\varphi+\tilde{y}_{\mathrm{Q}j}\sin\vartheta\sin\varphi)}\,A_j\tilde{v}_j \quad , \tag{2.47}$$

where N_s, $\tilde{v}_j$, $\tilde{x}_{\mathrm{Q}j}$, $\tilde{y}_{\mathrm{Q}j}$, and A_j denote the number of finite elements of the surface, the average surface velocity, the element center x- and y-coordinate, and the element surface area, respectively.

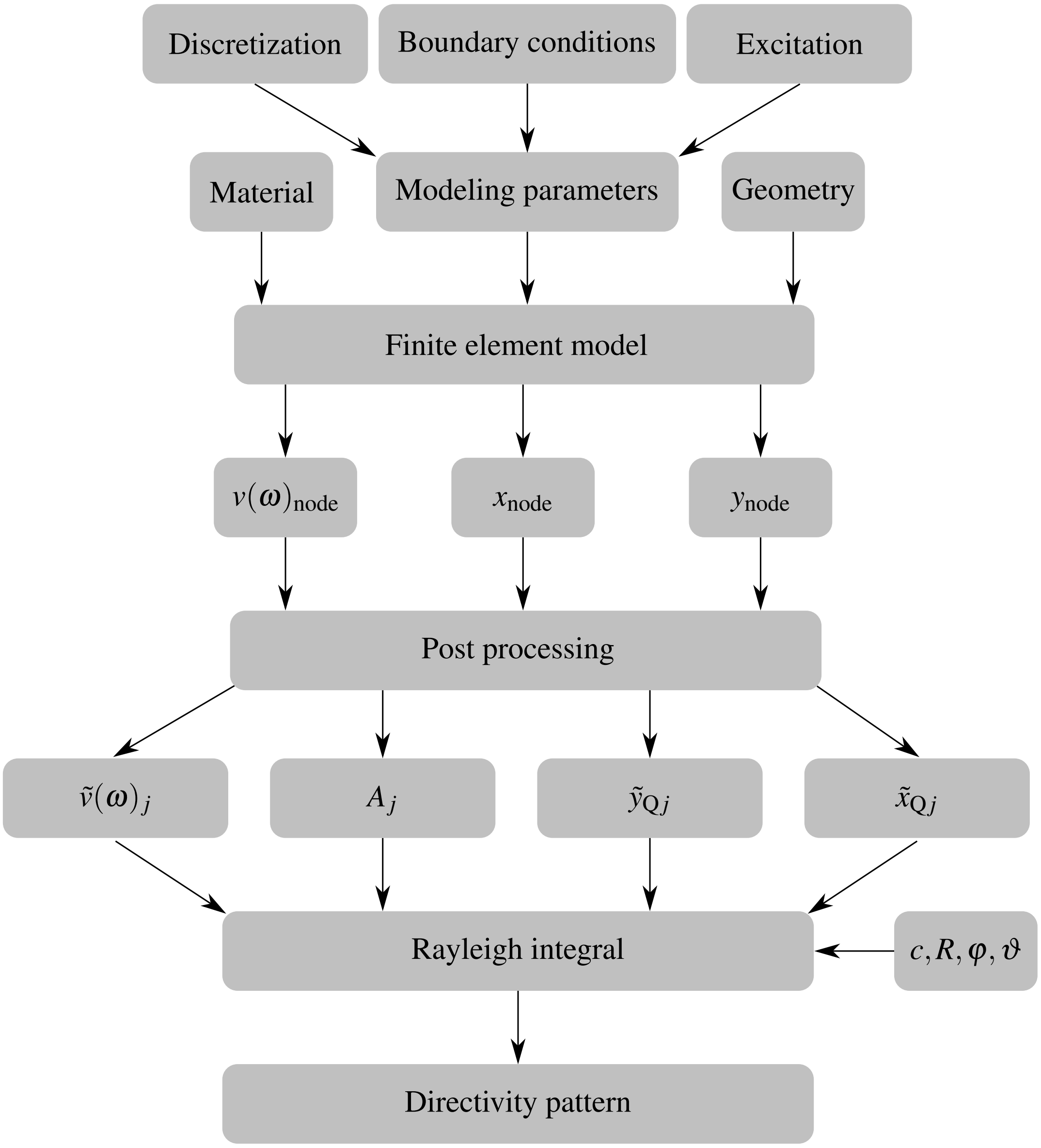

Figure 2.3: Workflow for calculation of the directivity pattern of an ultrasonic transducer with a coupled approach of finite element simulation and Rayleigh integral.

The accuracy of the solution depends on the size of the finite element mesh. In order to avoid mesh dependency, a convergence study can be carried out. Finally, the sound radiation behavior of the ultrasonic transducer is obtained with the workflow shown in Fig. 2.3. The approach couples the results obtained from finite element simulation with the Rayleigh integral.

2.4 Experimental testing

Numerical methods, as presented above, are very powerful tools and modern engineering tasks could be hardly solved without these methods. However, real applications of technical products are the overall objective of engineering tasks. Experimental testing of the investigated approaches is an important step. Thus, it is possible to evaluate whether the assumptions and simplifications made in the numerical investigations are appropriate to predict the behavior of real structures. In the field of vibration measurements, non-contact methods based on laser Doppler vibrometry are state of the art in scientific and industrial validation processes. Due to the absence of the contact between the measuring device and the measured object, the measurement does not affect the structural behavior. This is essential when investigating structures with low mass. Furthermore, the dynamic measurement is possible up to several MHz. Using a scanning laser Doppler vibrometer, the structure can be measured at multiple points with a high spatial resolution. Due to these advantages, laser Doppler vibrometry is a convenient method to characterize the structural, dynamic behavior of ultrasonic transducers. Special attention must be paid to the boundary conditions in experimental testing. In contrast to numerical methods, ideal boundary conditions like free-free, clamped or fixed cannot be obtained when testing real structures. They can rather be approximated. Hence, a certain deviation between physical and numerical model is present in any case. In order to validate the results from numerical simulations by experimental testing, this deviation must be minimized.

In the present work, mostly free-free boundary conditions are approximated. This is achieved by placing the test structure on two horizontally tightened yarns. Thus, a good approximation of free-free boundary conditions is achieved especially for light and small structures. In contrary, fixed boundary conditions can be approximated by jointing the test structure to a backing with high stiffness and large mass compared to the investigated structure. The excitation is realized be applying an electrical voltage to the electro-mechanical coupling element contained in the ultrasonic transducer. The surface velocity is then measured at several points. The obtained frequency response function offers the possibility to identify resonance frequencies and the corresponding operational deflection shape. Afterwards, the eigenfrequencies and modeshapes can be identified by an experimental modal analysis. A comprehensive introduction on the topic of modal testing is given by Ewins [151].

Chapter 3

Models

In this chapter, the investigated models are presented. Firstly, the finite element models are introduced. Afterwards, the material models are presented which are employed to describe the behavior of fiber reinforced composites. In Section 3.3, the manufacturing of physical models is discussed.

3.1 Finite element models

The finite element method, as introduced in Section 2.1, is a powerful method the approximate the behavior of complex structures. Therefore, the structure is discretized by a certain number of finite elements. The accuracy of the solution strongly depends on the type and size of finite elements. A detailed elaboration on this topic is given in [152]. It is shown that the convergence behavior of elements with quadratic interpolation formulation is significantly better than of elements with linear interpolation formulation. For this reason, only elements with quadratic interpolation formulation are employed in the investigated finite element models. Langer et al. [152] present guidelines to avoid mesh dependency of the results. The guidelines are applied to the finite element models used in this work. Afterwards, the mesh dependency is evaluated in a convergence study. Therefore, the average element edge length is reduced to a half in each step of the convergence study. Different parts are connected with tie-constraints [153]. In this way, a rigid connection is assumed. This is valid for monolithic structures. In case of joints in the physical model, an error is introduced. In order to reduce the influence of these joints on the dynamic behavior of the test structure, in Section 3.3 a short guideline is given for the model setup of physical models.

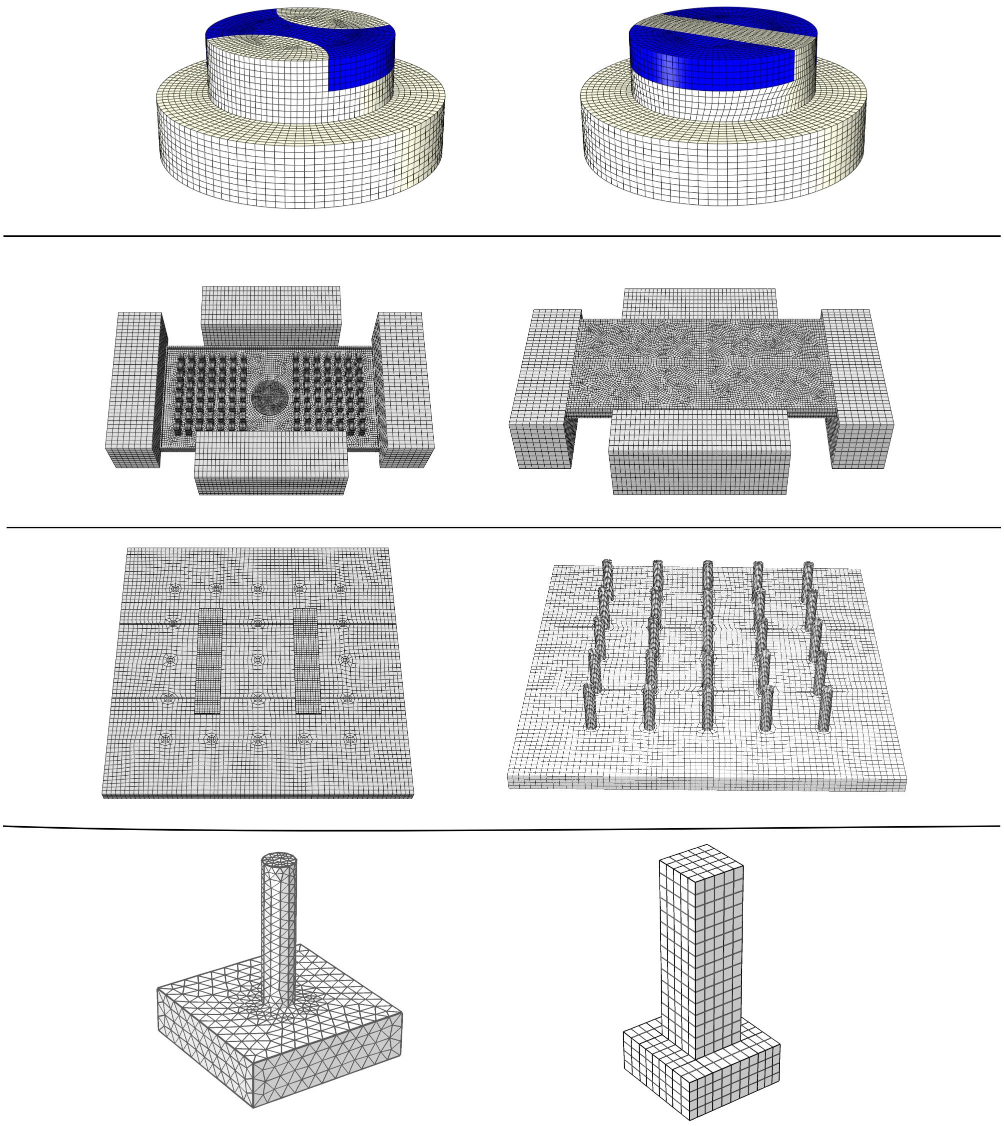

Figure 3.1: Overview of the finite element models investigated in this work. Top row: Sensor head models to investigate the influence of locally structured fiber reinforcements on the directivity patterns of ultrasonic transducers. 2$^{\text{nd}}$ row: Generic model of multi-frequency ultrasonic transducer employing stop band material. 3$^{\text{rd}}$ row: Generic model of phased array transducer to investigate the effect of stop band material as common backing structure in order to reduce cross-coupling. Bottom row: Unit cell models for calculating the dispersion properties of the above mentioned stop band materials.

Fig. 3.1 shows an overview of the finite element models used in this work. In the first category, a generic model of an ultrasonic sensor represented by the sensor head is illustrated. This model is employed to investigate the influence of locally structured fiber reinforcements on the directivity pattern of the sensor, cf. **Paper A**. In the second category, a model to investigate the potential of spatially distributed stop band material to achieve multi-frequency ultrasonic transducers is presented, cf. **Paper B**. The model consists of a plate like structure representing the sound radiating surface of an ultrasonic transducer. On the downside, 2×56 beam resonators are attached in order to form a stop band material. Blocks of aluminum are jointed to the structure in order to realize appropriate boundary conditions.

The model shown in the third category represents a generic model of a phased array transducer with a backing of stop band material. The single transducer elements are realized by bending elements of carbon fiber reinforced composite. These are jointed to a common backing. On the downside of the backing, 25 resonators form a resonant stop band material. Objective of the investigation is the reduction of mechanical cross-coupling caused by the common backing. The fourth category shows the unit cells corresponding to the models of category two and three. These are employed in the wave finite element method, cf. Section 2.2. Hence, the stop band behavior of the unit cell can be characterized.

3.2 Material models

The appropriate description of the material behavior is a key factor for suitable modeling. As introduced in Section 1.1.4, composite materials consist of at least two different materials. Fiber reinforced composites in particular consist of a large amount of fibers which are embedded in the matrix material. The modeling of the single fiber and matrix elements is not possible for the structure. In order to achieve an effective and appropriate description of the material behavior, a homogenization approach is employed to calculate the effective material parameters. Therefore, the properties of the single components of the composite are used to determine the homogenized properties. The approach is also known as the rule of mixtures [119]. In the presented work, carbon fiber reinforced composites are investigated. Due to the anisotropic behavior of the fiber, an orthotropic material model is employed to predict the dynamical behavior of the carbon fiber reinforced composite. The material models are discussed also in the appended **Paper A** [147]. Firstly, orthotropic material behavior is introduced. Afterwards, the homogenization approach is discussed for two different types of fiber reinforcements.

3.2.1 Orthotropic material behavior

The description of the behavior is done in a Cartesian coordinate system 1-2-3 related to the fiber orientation. The general stress-strain relation in an orthotropic material is described by [119]

$$\begin{pmatrix} \varepsilon_1 \\ \varepsilon_2 \\ \varepsilon_3 \\ \gamma_{12} \\ \gamma_{13} \\ \gamma_{23} \end{pmatrix} = \underbrace{\begin{bmatrix} S_{11} & S_{12} & S_{13} & 0 & 0 & 0 \\ S_{12} & S_{22} & S_{23} & 0 & 0 & 0 \\ S_{13} & S_{23} & S_{33} & 0 & 0 & 0 \\ 0 & 0 & 0 & S_{44} & 0 & 0 \\ 0 & 0 & 0 & 0 & S_{55} & 0 \\ 0 & 0 & 0 & 0 & 0 & S_{66} \end{bmatrix}}_{[S]} \cdot \begin{pmatrix} \sigma_1 \\ \sigma_2 \\ \sigma_3 \\ \tau_{12} \\ \tau_{13} \\ \tau_{23} \end{pmatrix} , \tag{3.1}$$

where $[\boldsymbol{S}]$ denotes the compliance matrix. ε, γ, σ, τ denote the normal strain, shear strain, normal stress, and shear stress, respectively. Assuming linear elastic behavior, the relation can be described in accordance to Hooke's law with so-called engineering constants [153] resulting in

$$\begin{pmatrix} \varepsilon_1 \\ \varepsilon_2 \\ \varepsilon_3 \\ \gamma_{12} \\ \gamma_{13} \\ \gamma_{23} \end{pmatrix} = \begin{bmatrix} 1/E_1 & -\nu_{21}/E_2 & -\nu_{31}/E_3 & 0 & 0 & 0 \\ -\nu_{12}/E_1 & 1/E_2 & -\nu_{32}/E_3 & 0 & 0 & 0 \\ -\nu_{13}/E_1 & -\nu_{23}/E_2 & 1/E_3 & 0 & 0 & 0 \\ 0 & 0 & 0 & 1/G_{12} & 0 & 0 \\ 0 & 0 & 0 & 0 & 1/G_{13} & 0 \\ 0 & 0 & 0 & 0 & 0 & 1/G_{23} \end{bmatrix} \cdot \begin{pmatrix} \sigma_1 \\ \sigma_2 \\ \sigma_3 \\ \tau_{12} \\ \tau_{13} \\ \tau_{23} \end{pmatrix} . \tag{3.2}$$

Applying the relation $\frac{\nu_{ij}}{E_i} = \frac{\nu_{ji}}{E_j}$, known as the Maxwell-Betti reciprocity relation [119], Eq. (3.2) can by written as

$$\begin{pmatrix} \varepsilon_1 \\ \varepsilon_2 \\ \varepsilon_3 \\ \gamma_{12} \\ \gamma_{13} \\ \gamma_{23} \end{pmatrix} = \begin{bmatrix} 1/E_1 & -\nu_{12}/E_1 & -\nu_{13}/E_1 & 0 & 0 & 0 \\ -\nu_{12}/E_1 & 1/E_2 & -\nu_{23}/E_2 & 0 & 0 & 0 \\ -\nu_{13}/E_1 & -\nu_{23}/E_2 & 1/E_3 & 0 & 0 & 0 \\ 0 & 0 & 0 & 1/G_{12} & 0 & 0 \\ 0 & 0 & 0 & 0 & 1/G_{13} & 0 \\ 0 & 0 & 0 & 0 & 0 & 1/G_{23} \end{bmatrix} \cdot \begin{pmatrix} \sigma_1 \\ \sigma_2 \\ \sigma_3 \\ \tau_{12} \\ \tau_{13} \\ \tau_{23} \end{pmatrix} . \tag{3.3}$$

Finally, nine material properties of the composite are required to characterize the orthotropic material stress-strain behavior, the Young's moduli E_1, E_2, E_3, the Possion's ratios ν_{12}, ν_{13}, ν_{23}, and the shear moduli G_{12}, G_{13}, G_{23}. Besides the stress-strain relation of the material, the mass density is required to characterize the dynamic behavior of the structure, cf. Section 2.1.1. In order to achieve the effective mass density of the composite ρ_C, the rule of mixture is applied to the single components.

3.2.2 Unidirectional, non-crimp fabric

Unidirectional, non-crimp fabrics are textiles having one distinctive axis of fiber orientation. According to the Cartesian coordinate system 1-2-3 of the material, the direction of fiber orientation coincides with direction 1. Unidirectional, non-crimp fabrics exhibit symmetry, normal to direction 1. Thus, the independent variables of material properties are reduced from nine to six by $E_2^\mathrm{UD} = E_3^\mathrm{UD}$, $\nu_{12}^\mathrm{UD} = \nu_{13}^\mathrm{UD}$, and $G_{12}^\mathrm{UD} = G_{13}^\mathrm{UD}$. Introducing the assumption of $G_{23}^\mathrm{UD} = \frac{E_2^\mathrm{UD}}{2(1+\nu_{23}^\mathrm{UD})}$, the material model is specified as transversal isotropic material model. The number of independent material parameters is reduced to five in this case.

The mechanical properties can be represented by applying a rheological model. Fig. 3.2 shows exemplarily the rheological model to obtain the Young's modulus in direction 1. It consists of a parallel circuit out of a spring representing the Young's modulus parallel to the fiber axis $E_{\mathrm{F},\parallel}$ and a spring representing the Young's modulus of the matrix material E_M.

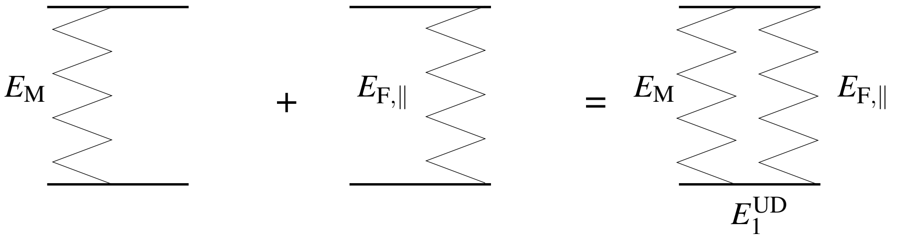

Figure 3.2: Rheological model to calculate the Young's modulus E_1^UD in direction parallel to the fiber axis for a unidirectional, non-crimp fabric, cf. [147].

The Young's modulus can be calculated by [119]

$$E_1^\mathrm{UD} = \Phi E_{\mathrm{F},\parallel} + (1-\Phi)E_\mathrm{M} \quad , \tag{3.4}$$

with Φ denoting the overall fiber volume fraction of the composite. The Young's modulus transverse to the fiber direction is calculated using the semi-empirical approach of Puck by [119]

$$E_2^\mathrm{UD} = \frac{E_\mathrm{M}}{1-\nu_\mathrm{M}^2} \frac{1+0.85\Phi^2}{(1-\Phi)^{1.25} + \frac{E_\mathrm{M}}{(1-\nu_\mathrm{M}^2)E_{\mathrm{F},\perp}}} \quad . \tag{3.5}$$

The Poisson's ratio is calculated applying the rule of mixture

$$\nu_{12}^{\mathrm{UD}} = \Phi\nu_{\mathrm{F},12} + (1-\Phi)\nu_{\mathrm{M}} \quad . \tag{3.6}$$

The transverse Poisson's ratio ν_{23}^{UD} is obtained by the approach presented of Foye [122]

$$\nu_{23}^{\mathrm{UD}} = \Phi\nu_{\mathrm{F},23} + (1-\Phi)\nu_{\mathrm{M}} \left[\frac{\left(1+\nu_{\mathrm{M}} - \nu_{12}^{\mathrm{UD}}\frac{E_{\mathrm{M}}}{E_{1}^{\mathrm{UD}}}\right)}{\left(1-\nu_{\mathrm{M}}^{2} + \nu_{\mathrm{M}}\nu_{12}^{\mathrm{UD}}\frac{E_{\mathrm{M}}}{E_{1}^{\mathrm{UD}}}\right)} \right] \quad . \tag{3.7}$$

The shear moduli G_{12}^{UD} and G_{13}^{UD} are obtained with the semi-empirical approach of Förster [119]

$$G_{12}^{\mathrm{UD}} = G_{13}^{\mathrm{UD}} = G_{\mathrm{M}} \frac{1+0.4\Phi^{0.5}}{(1-\Phi)^{1.45} + \frac{G_{\mathrm{M}}}{G_{\mathrm{F},12}}\Phi} \quad . \tag{3.8}$$

In order to retrieve the shear modulus $G_{\mathrm{F},12}$ for anisotropic materials, the approach given by Summerscales [125] is employed

$$G_{\mathrm{F},12} = \frac{\sqrt{E_{\mathrm{F},\parallel}E_{\mathrm{F},\perp}}}{2(1+\sqrt{\nu_{\mathrm{F},12}\nu_{\mathrm{F},21}})} \quad . \tag{3.9}$$

Applying the Maxwell-Betti relation, the Poisson's ratio $\nu_{\mathrm{F},21}$ is obtained by

$$\nu_{\mathrm{F},21} = \nu_{\mathrm{F},12}\frac{E_{\mathrm{F},\perp}}{E_{\mathrm{F},\parallel}} \quad . \tag{3.10}$$

Due to the assumption of a transversal isotropic material, G_{23}^{UD} is determined by

$$G_{23}^{\mathrm{UD}} = \frac{E_{2}^{\mathrm{UD}}}{2(1+\nu_{23}^{\mathrm{UD}})} \tag{3.11}$$

as mentioned before.

3.2.3 Balanced, woven fabric

Woven fabrics are textiles formed on a loom. In this work, plain weaves are utilized to reinforce epoxy resin. The plain weave is formed by shedding after every weft insertion. Thus, the warp yarn alternates between lifting and lowering after every weft yarn. By this, the warp and weft yarn are crimped [118]. This has a major effect on the mechanical properties of the woven fabric, especially for anisotropic materials like carbon fiber. Balanced, woven fabrics exhibit a ratio of 1 between warp and weft yarn in terms of volume and weight. Consequently, the properties in warp and in weft direction are equal, corresponding to directions 1 and 2 of the coordinate system. Balanced, woven fabrics show less anisotropic behavior within one layer compared to unidirectional, non-crimp fabrics. The required material properties are reduced from nine to six engineering constants, because of $E_1^{\mathrm{WF}} = E_2^{\mathrm{WF}}$, $\nu_{13}^{\mathrm{WF}} = \nu_{23}^{\mathrm{WF}}$, and $G_{13}^{\mathrm{WF}} = G_{23}^{\mathrm{WF}}$. In contrast to unidirectional, non-crimp fabrics, the employed material model is not a transversal isotropic material model as $G_{12}^{\mathrm{WF}} = \frac{E_1^{\mathrm{WF}}}{2(1+\nu_{12}^{\mathrm{WF}})}$ does not apply [124].

An orthotropic material model, developed in [154], is applied. Fig. 3.3 shows the rheological model of the composite to calculate the Young's modulus in direction 1 for a balanced, woven fabric. It consists of a series and parallel circuit of fiber and matrix material properties. Two springs are arranged in a series, one of which representing the Young's modulus of the matrix (E_{M}) while the other one describes the Young's modulus perpendicular to the fiber axis ($E_{\mathrm{F},\perp}$). In parallel to this series, another spring element is considered. This is related to the Young's modulus of the fiber parallel to its axis ($E_{\mathrm{F},\|}$).

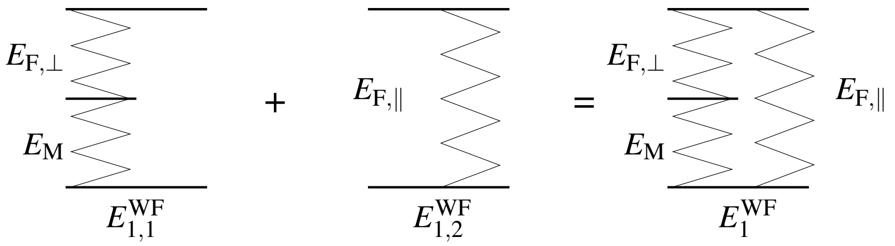

Figure 3.3: Rheological model to calculate the Young's modulus E_1^{WF}, cf. [154].

Applying the rule of mixture, the series of springs is calculated by

$$E_{1,1}^{\mathrm{WF}} = \frac{E_{\mathrm{M}} E_{\mathrm{F},\perp}}{\Phi_{1,1} E_{\mathrm{M}} + (1-\Phi_{1,1}) E_{\mathrm{F},\perp}} \quad , \tag{3.12}$$

where $\Phi_{1,1}$ denotes the fiber volume fraction of fibers with an axis orientation perpendicular to the direction 1. In a balanced, woven fabric, it can be calculated by

$$\Phi_{1,1} = \frac{\frac{\Phi}{2}}{1-\frac{\Phi}{2}} \quad , \tag{3.13}$$

with Φ representing the overall fiber volume fraction of the composite. The Halpin-Tsai method introduces a semi-empirical approach to take into account non-uniform strain in the matrix [120].

Consequently, a correction factor β is inserted into Eq. (3.12), resulting in

$$E_{1,1}^{\mathrm{WF}} = \frac{\beta E_{\mathrm{M}} E_{\mathrm{F},\perp}}{\Phi_{1,1}\beta E_{\mathrm{M}} + (1-\Phi_{1,1})E_{\mathrm{F},\perp}} \quad . \tag{3.14}$$

As mentioned above, in woven fabrics the fibers exhibit crimp. As a result, the fiber axis is only in some parts of the fabric parallel to the direction 1. This leads to a reduced stiffness in direction 1 for anisotropic materials like carbon. In the material model, this is considered by introducing a factor of stiffness reduction $\eta \in [0,1]$. The second part of the parallel circuit, cf. Fig. 3.3, is then calculated by

$$E_{1,2}^{\mathrm{WF}} = \eta E_{\mathrm{F},\parallel} \quad . \tag{3.15}$$

The resulting Young's modulus for the direction 1 is finally obtained by

$$E_{1}^{\mathrm{WF}} = \frac{\Phi}{2} E_{1,2}^{\mathrm{WF}} + (1-\frac{\Phi}{2}) E_{1,1}^{\mathrm{WF}} \quad . \tag{3.16}$$

In direction 3, there exists only a series circuit out of fibers perpendicular to its axis and matrix. Thus, E_3^{WF} is calculated in equivalent to $E_{1,1}^{\mathrm{WF}}$ by

$$E_{3}^{\mathrm{WF}} = \frac{\beta E_{\mathrm{M}} E_{\mathrm{F},\perp}}{\Phi\beta E_{\mathrm{M}} + (1-\Phi)E_{\mathrm{F},\perp}} \quad . \tag{3.17}$$

Applying the rule of mixture, the Poisson's ratio ν_{12}^{WF} is calculated in the same manner like Young's moduli by

$$\nu_{12,1}^{\mathrm{WF}} = \frac{\nu_{\mathrm{M}} \nu_{\mathrm{F},21}}{\Phi_{1,1}\nu_{\mathrm{M}} + (1-\Phi_{1,1})\nu_{\mathrm{F},12}} \tag{3.18}$$

and

$$\nu_{12,2}^{\mathrm{WF}} = \eta \nu_{\mathrm{F},12} \tag{3.19}$$

resulting in

$$\nu_{12}^{\mathrm{WF}} = \frac{\Phi}{2} \nu_{12,2}^{\mathrm{WF}} + (1-\frac{\Phi}{2}) \nu_{12,1}^{\mathrm{WF}} \quad . \tag{3.20}$$

Poisson's ratio $\nu_{13} = \nu_{23}$ is obtained by an approach presented in [124]. The properties of a balanced, woven fabric are mimicked by unidirectional layers. Thus, Poisson's ratio is calculated by

$$\nu_{13}^{\mathrm{WF}} = E_{1}^{\mathrm{WF}} \left(\frac{1}{E_1} \frac{E_1(\nu_{12}+\nu_{23}+\nu_{12}\nu_{23}) + \nu_{12}^2}{E_1 + (1+2\nu_{12})E_2} \right)^{\mathrm{UD}} \quad . \tag{3.21}$$

The in-plane shear modulus is obtained in the same way as the Young's moduli.

$$G_{12}^{\mathrm{WF}} = \frac{\beta G_{\mathrm{M}} G_{\mathrm{F},12}}{\Phi \beta G_{\mathrm{M}} + (1-\Phi) G_{\mathrm{F},12}} \quad . \tag{3.22}$$

A method to calculate the transverse shear moduli is presented in [124]. It uses equivalent properties of a unidirectional reinforced laminate to obtain G_{13}^{WF} by

$$G_{13}^{\mathrm{WF}} = G_{23}^{\mathrm{WF}} = (\frac{1+\nu_{23}^{UD}}{E_2^{UD}} + \frac{1}{2G_{12}})^{-1} \quad . \tag{3.23}$$

In [124], inaccuracies for the approach given in Eq. (3.23) are shown. However, in [154] it is shown that the influence of the transverse shear modulus on the dynamic behavior is small for mode shapes and frequencies ranges similar to the investigated ones in this work.

3.2.4 Prediction of material properties

The above presented material models are employed to predict the homogenized properties of the composite material. Therefore, the properties of the single components and the fiber volume fraction are required. Generally spoken, polymer materials show complex material behavior [155]. The material rather exhibits viscoelasticity than linearity as introduced by Hookean stress-strain behavior. In order to apply Hooke's law, the material behavior can be linearized at an operating point or interval with regard to temperature, frequency and deformation. This is done in preliminary investigations. Thus, effective material properties are determined. The properties of carbon fibers are obtained from the manufacturer. The Young's modulus $E_{\mathrm{F},\|}$ is usually given by the manufacturer. In contrast, $E_{\mathrm{F},\perp}$ is mostly unknown. The ratio of $\frac{E_{\mathrm{F},\|}}{E_{\mathrm{F},\perp}} = 12$ gives an appropriate assumption for the used carbon fiber [154].

Finally, the fiber-volume ratio needs to be calculated. In order to do so, the material properties of the fiber reinforcement and geometrical parameters of the structure are employed. Usually, textile fabrics are characterized by the areal density $\tilde{\rho}_{\mathrm{Fa}}$, also known as area weight. It describes the mass per area of two dimensional structures [156]. Knowing the density of carbon fiber ρ_{F} and the thickness of the structure t_{St}, the fiber volume fraction Φ is calculated by [154]

$$\Phi = \frac{n \tilde{\rho}_{\mathrm{Fa}}}{\rho_{\mathrm{F}} t_{\mathrm{St}}} \quad , \tag{3.24}$$

where n denotes the number of layers in the structure. The maximum number of layers in the structure is limited by the integer quotient

$$n_{\mathrm{max}} = \frac{t_{\mathrm{St}}}{t_{\mathrm{Fa}}} \quad , \tag{3.25}$$

with t_{Fa} describing the thickness of the fabric layer.

3.3 Physical models

Experimental testing is an important element to verify the numerical investigations as mentioned in Section 2.4. Consequently, physical models are required to carry out the experiments. In order to realize these models, different manufacturing techniques are combined. The most important ones for this work are

- resin transfer molding processes,
- additive manufacturing of polymers, and
- jointing based on adhesives.

Injection molding processes are well-known and widely used manufacturing processes for fiber reinforced composites [119]. The molding tool consists of at least two parts having a cavity. The general process to produce a composite structure can be described as follows. Firstly, the fiber reinforcement is placed in the cavity. Afterwards, the tool is closed and resin is injected. Once the curing of the resin is completed, the structure of fiber reinforced composite can be demolded. In practical use, a wide bunch of various injection molding procedures exist which can be distinguished by process details, e.g. injection pressure or pressurizing method [157].

Additive manufacturing attracted growing attention during the last years. It offers the possibility to produce structures by adding material at a defined position. The main advantage of this manufacturing technique is the flexibility and cost effectiveness for rapid prototyping. Hence, nearly every geometry can be produced directly without any other, design related tools. Furthermore, current additive manufacturing machines allow a user-friendly direct usage of 3D-CAD data as input. Disadvantages compared to classical manufacturing are mainly a lower accuracy, limitations in material choice, and lower productivity. However, additive manufacturing is a key enabler in the scientific and industrial field to shorten investigation and development time. As a consequence, a large number of different additive manufacturing techniques are developed during the last years, cf. [158]. In the presented work, the investigated structures are manufactured by PolyJet [159]. This technology offers the possibility to produce fully filled, solid structures. As a result, the material of the structure is homogeneous which allows a straightforward numerical modeling of the structure. As the physical models are employed to validate the numerical simulations, this is major advantage of PolyJet technology.

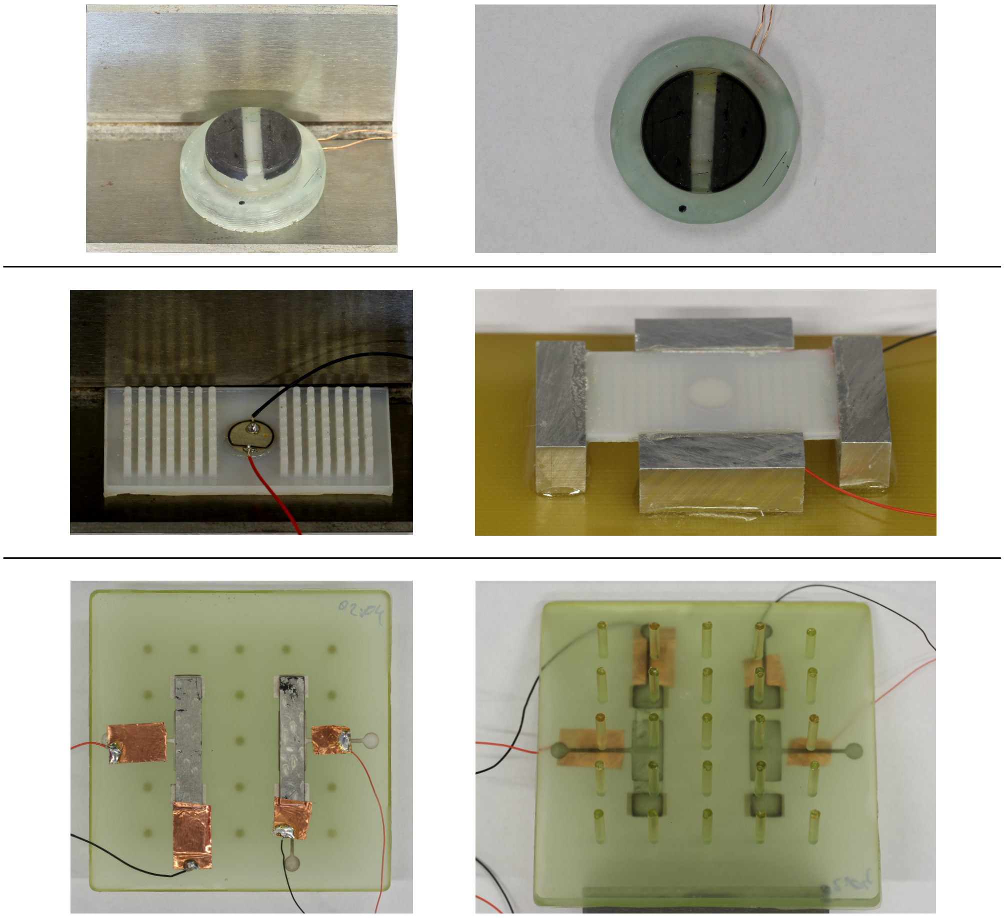

Figure 3.4: Overivew of the pyhsical models employed for experimental testing. Top row: Sensor head model to investigate the directivity pattern of an ultrasonic transducer. Middle row: Generic model of multi-frequency ultrasonic transducer employing stop band material. Bottom row: Generic model of phased array transducer to investigate the effect of stop band material as common backing structure.

In order to complete the assembling of the physical models, different parts are required to be jointed. The design, modeling, and applications of proper joints is a separate research field and out of scope of this work. In numerical simulations, the connection between different parts is assumed as rigid connections. In order to reduce the influence of joints in experimental testing the following guidelines are applied:

1. If possible, the test structure is realized as a monolithic part. Influences by joints are avoided.

2. In case joints cannot be avoided, test structures are designed with joints at locations where the influence is small. These are locations with small stresses.
3. Joints are realized with thin layers and with an adhesive providing high stiffness. Thus, the influence on the dynamic behavior is reduced and a rigid connection is approximated.

Fig. 3.4 gives an overview on physical models employed for experimental testing in this work.

Chapter 4

Results and Summary of Appended Papers

In this section, the key results and a short summary for each of the appended papers are presented. The main contribution of this work is stated as follows:

- A novel approach to realize ultrasonic transducers with anisotropic directivity pattern is presented. Therefore, locally structured fiber reinforcements are employed. A parameter study identifies the influence of various design parameters to the eigenfrequency and the anisotropy factor of the directivity pattern (**Paper A**).
- The concept of spatially distributed stop band material is presented. It is employed to modify the operational deflection shape of a structure within a particular frequency range. Based on this concept, a multi-frequency ultrasonic transducer with only one electro-mechanical coupling element and suitable sound radiation properties for surround sensing at two distinctive frequencies is achieved (**Paper B**).
- Mechanical cross-coupling caused by a common backing in phased array transducers is investigated. It is found that weak cross-coupling is associated to strong cancellation effect between in-phase and out-of-phase modes of the bending elements. Furthermore, stop band material is identified as novel solution to reduce mechanical cross-coupling in a phased array transducer (**Paper C**).

Fig. 4.1 gives an overview of the field of ultrasonic transducers for surround sensing applications and indicates to which category each of the appended papers contributes. The presented approaches can enhance the performance of ultrasonic transducers or transducer arrays. They can be applied separately as well as in combintation. Hence, this work contributes to achieve more comprehensive and more reliable surrond sensing systems. Furthermore, the introduced approaches to modify the operational deflection shapes of systems as shown in **Paper A** and **Paper B** can be transferred to other applications wherever a certain operational deflection shape is desired.

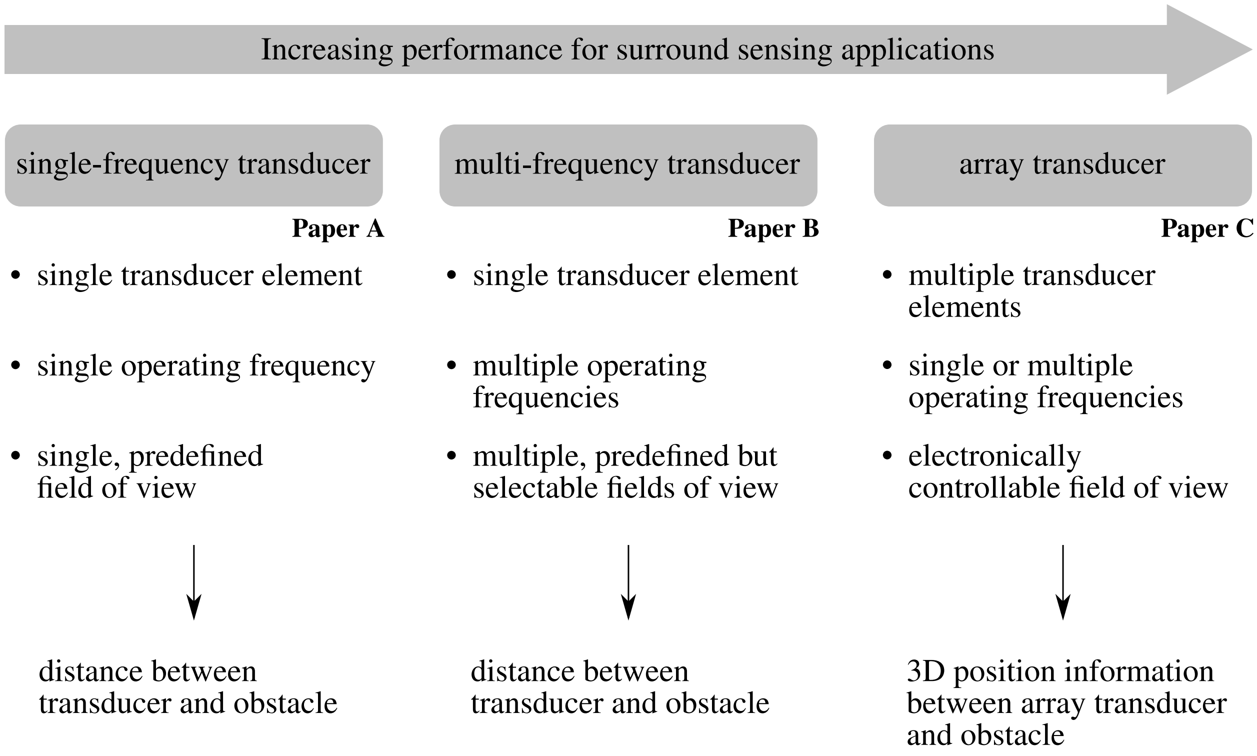

Figure 4.1: Overview of the field of ultrasonic transducers for surround sensing applications and the key performance indicators to distinguish the categories. It is indicated to which category of ultrasonic transducer each of the appended papers contributes.

4.1 Paper A

Locally structured fiber reinforcements: An approach to realize anisotropic directivity pattern in ultrasound transducers

Novelty and key results:

Ultrasonic transducers are desired to exhibit a comprehensive field of view. In order to avoid ground reflections, the directivity pattern in the vertical plan should be a narrow angled beam. In contrast, in the horizontal plane, a wide angled beam is desired to enlarge to the field of view. These two requirements lead to anisotropic directivity patterns. This study addresses the fiber reinforcement of composite material as a new design space. Thus, anisotropic directivity patterns can be achieved by locally structuring the fiber reinforcement. As a result, sections with different material properties are achieved within a monolithic structure.

In this study, a generic model representing the head of an ultrasonic transducer is investigated. The sound radiation behavior of the generic model is calculated using the Rayleigh integral. Two different designs of fiber reinforcement are considered. Each design is investigated with a balanced, woven fabric and with an unidirectional, non-crimp fabric. A parameter study is carried out for one of the two designs. Thus, the influence of various design parameters on the eigenfrequency and the anisotropy factor of the directivity pattern is identified. In the investigated design, the angle of fiber orientation is found to have the highest influence on the directivity pattern for both types of fabrics. Finally, the numerical investigation is validated by experimental testing. Therefore, the velocity of the sound radiating surface is measured employing laser Doppler vibrometry. Good accordance between simulation and experiment is found. A modal assurance criterion of 0.93 is determined. The presented approach offers a novel solution to realize anisotropic directivity patterns in ultrasonic transducers having a rotationally symmetric geometry.

Individual contributions of the candidate: Henneberg introduced the approach of modifiying the operational deflection shape of an ultrasonic transducer by locally structuring the fiber reinforcement. Hereby, the design of the fiber reinforcement was a key element. In order to evaluate the directivity pattern, the implementation of the Rayleigh integral was an essential step realized by Henneberg. The specimen preparation and finally the experimental testing were also conducted by Henneberg.

4.2 Paper B

The potential of stop band material in multi-frequency ultrasonic transducers

Novelty and key results:

Ultrasonic transducers are desired to be operated at two or more distinctive operating frequencies. Therefore, ultrasonic transducers can be operated in short intervals or in parallel. The sensor signal can be discriminated by frequency filtering. This study presents an approach to achieve two well separated operating frequencies with suitable sound radiation behavior using only one electro-mechanical coupling element. Therefore, the concept of spatially distributed stop band material is introduced. As a result, the operational deflection shape is modified within a certain frequency range. The study investigates a plate like structure with 2×56 resonators attached to one side of the plate. The resonators form two spatially separated sections of stop band material. They are designed to exhibit a resonant stop band for shear and bending waves. The other side of the plate like structure represents the sound radiating surface of an ultrasonic transducer. In order to achieve a generic model which is comparable to a real ultrasonic transducer, two different configurations of fixed boundary conditions are investigated. In the first configuration, only the short edges of the rectangular plate are fixed. In a second configuration, the long edges of the plate are fixed additionally. The excitation of the structure is realized with a piezoelectric element placed between the sections of stop band material in the center of the plate. As a result, it is found that a particular operational deflection shape is obtained in case the excitation frequency coincides with the frequency of the stop band. In this case, the bending wave, which is introduced in the center of the plate, is reflected at the boundary of the stop band material. The operational deflection shape at the middle part of the plate like structure is similar to the first normal mode of a plate with fixed boundaries while the rest of the plate like structure remains in equilibrium position. Finally, this results in a directivity pattern without distinctive sidelobes which is suitable for surround sensing applications. This particular behavior is similar in both configurations. Hence, it is nearly independent from the boundary conditions of the investigated system. In experimental testing, the results from numerical simulation are validated. The results show good accordance between simulation and experiments. Finally, the approach is transferred in the ultrasonic frequency range. Therefore, material and dimensions of the generic model are adjusted.

Individual contributions of the candidate: Henneberg developed the approach of distributed stop band material with the purpose to achieve distinctive operational deflection shapes in certain frequency ranges with the objective to establish a multi-frequency ultrasonic transducer. Numerical simulations, experimental testing as well as drawing the manuscript was done by Henneberg.

4.3 Paper C

Reducing mechanical cross-coupling in phased array transducers using stop band material as backing

Novelty and key results:

Cross-coupling is a characteristic property of phased array transducers. It describes the behavior that single transducer elements do not work independently which results in a loss of performance. In this study, the mechanical cross-coupling caused by a common backing is investigated in a generic model. It consists of two bending elements, representing the single transducer elements, jointed to a common backing. In the first part of the study, the influence of the backing on cross-coupling is examined. The backing does not contain an extra lossy region as known from other researches. Furthermore, the dimensions are small. Consequently, wave reflections must be taken into account at the edges of the backing. This is especially important in compact, low-frequency, air-coupled phased array transducers. In this configuration, weak cross-coupling is identified as strong cancellation effect between in-phase and out-of-phase modes of the bending elements. The occurrence of these modes is related to the particular dynamic behavior of the backing. Based on these results, it is possible to minimize mechanical cross-coupling based on a numerical modal analysis. With regard to an optimization task, this is an advantage in terms of computational efficiency. However, the reduction of cross-coupling by minimizing the difference in eigenfrequency between the in-phase and out-of-phase mode is connected to avoid the coincidence of backing dominated modes with the operating frequency. To overcome this issue, the potential of stop band material in order to reduce mechanical cross-coupling is investigated in a second part of this work. Therefore, the model of the backing is extended by 25 beam resonators on the downside of the plate. These resonators are designed to form a stop band which does not allow free wave propagation of shear and bending waves in certain frequency ranges. It is shown that stop band material as backing can reduce the cross-coupling in phased array transducers significantly in case the operating frequency is within the frequency range of the stop band. In order to validate the results from numerical simulation, a physical model is manufactured. Therefore, an epoxy backing with 25 beam resonators is prepared in a molding process. Afterwards, the bending elements are jointed to the backing. The results from experimental testing and numerical simulation show good accordance.

Individual contributions of the candidate: Henneberg introduced the idea to create a stop band and match its frequency range with the operating frequency of the ultrasonic transducer array in order to reduce mechanical cross-coupling. The design of an appropriate and manufacturable stop band material was done by Henneberg as well as the numerical simulations. The contribution includes the development of a process to manufacture monolithic epoxy structures of stop material and the conduction of the related experiments. The manuscript was drawn by the lead author.

Chapter 5

Discussion of Results

This work is guided by three research questions which have been formulated in Section 1.2. Each of the appended papers answers one of these questions. Hence, the introduction of locally structured fiber reinforcements shows a possibility to achieved a highly anisotropic directivity pattern in ultrasonic transducers with rotationally symmetric geometry. The approach aims to gain sections with different material properties within a monolithic structure. In this way, the dynamic behavior of an ultrasonic transducer can be tailored by the design of the locally structured fiber reinforcement. The design of the fiber reinforcement, in terms of its geometry as well as of its textile fabric construction, and the angle of fiber orientation are identified as suitable design parameters to control the directivity pattern of the ultrasonic transducer. A major difference of the approach is the use of fiber reinforced composites instead of metal like in many other realizations of ultrasonic transducers, e.g. [13]. Known approaches from literature employ the contour geometry of the transducer as design space in order to achieve anisotropic directivity patterns. [18] shows a realization where a reinforcement of the pot like structure is achieved with material accumulation on two opposite sides on the inner side of the transducer. As a result, this approach is accompanied by design limitations and it is not possible to achieve anisotropic directivity patterns with rotationally symmetric geometry on the inner side of the transducer. However, a rotationally symmetric contour can be an advantage for certain design aspects. These can be the increase of sensitivity by employing a larger piezoelectric element, reducing the diameter of the transducer but keeping the dimension of the piezoelectric coupling element, or adding further design elements as discussed later in this section. The study presented by Ho et al. [19] employs altering boundary conditions to modify the directivity pattern of the ultrasonic transducer. Another approach presented by Cheng et al. [20] introduces penetration slots in the lateral part of the transducer. Thus, the anisotropy factor is increased from 2.6 to 3.8 by inserting three penetrating slots. These approaches are also suitable to achieve anisotropic ultrasonic transducers with a rotationally symmetric contour of the inner side. However, a modification of the transducer contour is always required to control the directivity pattern. Furthermore, penetrating the transducer is mostly not permitted as the inner components of the transducer must be protected against environmental influences like humidity, dust, and chemicals. The approach of locally structured fiber reinforcement overcomes the above discussed restrictions as the directivity pattern can be controlled by the design of the fiber reinforcement. The high sensitivity of the directivity pattern to the angle of fiber orientation denote the advantage as well as the weakness of the presented approach at the same time. On the one hand, this fact allows the adoption of the dynamic behavior of the ultrasonic transducer to the requirements easily. On the other hand, it requires a reproducible process with tight manufacturing tolerances for production in order to achieve the desired directivity pattern of the ultrasonic transducer.

In order to increase the performance for surround sensing applications, the research is guided to multi-frequency ultrasonic transducers by the second research question, cf. Section 1.2. The intention is the development of ultrasonic transducers which have only one electro-mechanical coupling element but can be operated at two or more frequencies with suitable sound radiation properties. The approach presented in this work employs spatially distributed stop band material in order to achieve the desired behavior. The generic model consists of a section without stop band material where the excitation is realized by a piezoelectric coupling element. Furthermore, two spatially separated sections with stop band material are realized by attaching multiple tuned resonators on the downside of the plate like structure. These two sections exhibit a stop band within a certain frequency range which is defined by the resonant behavior of the stop band material. The dynamic behavior can be interpreted as follows. In frequency ranges where the excitation frequency does not coincide with the frequency range of the stop band, the plate like structure behaves similar to a plate as described by the classical plate theory [160]. Exciting the first resonance frequency, the plate like structure shows an operational deflection shape which is dominated by the first normal mode of the plate. At this frequency, suitable sound radiation properties are achieved. These are indicated by a directivity pattern similar to monopole or dipole characteristics without distinctive side lobes. In case the excitation frequency coincides with the stop band frequency range of the spatially distributed stop band material, the wave gets induced by the electro-mechanical coupling element in the center of the plate like structure. In the first section, the wave propagates freely until it reaches the section which exhibits the stop band behavior. As no free wave propagation is possible in this part of the plate, the wave gets reflected. As a result, an operational deflection shape is achieved which is mainly dominated by the design of the stop band material. Designing the plate like structure and the stop band material adequately, an operational deflection shape can be achieved where a part of the structure behaves similar to the first normal mode. The rest of the structure remains in equilibrium position in this case. Due to this behavior, suitable sound radiation properties are achieved at an additional resonance frequency which can be employed as second operating frequency of the ultrasonic transducer. Different to approaches known from literature, the presented approach can realize a multi-frequency ultrasonic transducer with only one electro-mechanical coupling element. No modification of the coupling element itself is required which allows the use of simple and cost effective electronics. In the studies of Wang and Lee [23], multiple electrodes are required to realize multiple operating frequencies. Sun et al. [29] combine two electro-mechanical coupling elements, a CMUT and a PMUT, into a hybrid one. Another approach of hybridization is presented in [27, 28]. An ultrasonic transducer array with multiple operating frequencies is realized in [24]. The various operating frequencies are realized by CMUT elements of different dimensions.

A disadvantage of the approach presented in this work can be identified in more required space on the inner side of the ultrasonic transducer to realize the stop band material. The available space is usually very limited in the application fields of ultrasonic transducers. Facing this issue, it seems reasonable to direct further investigations in the direction to combine the approaches of locally structured fiber reinforcement and spatially distributed stop band material. The first one reduces design restrictions as discussed above while the second one can be employed to achieve a multi-frequency transducer.

The highest surround sensing performance can be reached with phased array ultrasonic transducers. Thus, it is possible to electronically control the field of view and to obtain real 3D position information between the array transducer and an obstacle, cf. Fig. 4.1. However, mechanical cross-coupling between the transducer elements decreases the performance of phased array ultrasonic transducers. The reduction of mechanical cross-coupling is addressed by the last research question. In the first part of the study, the behavior of mechanical cross-coupling is investigated in a generic model representing a compact, low frequency, and air-coupled phased array transducer. Based on the modal behavior of the entire structure, mechanical cross-coupling is identified and interpreted as follows. The transducer elements exhibit a mode with in-phase motion and a mode with out-of-phase motion. It is found that a small difference in the eigenfrequency of the in-phase and the out-of-phase mode leads to weak cross-coupling and is interpreted as strong cancellation of these modes when considering the transfer mobility between two transducer elements. The drive point mobility remains nearly unaffected. The description of mechanical cross-coupling by the modal behavior of the entire structure is different to that known from literature, like [32, 53]. This is possible as in compact phased array transducers, the dimensions of the backing are small compared to the dimensions of the transducer elements. Furthermore, no extra lossy region on the edge of the backing is present. Thus, wave reflections on the edges of the backing must be considered in this type of array transducers. The presented method can be used to qualitatively evaluate mechanical cross-coupling based on a modal analysis and the difference in eigenfrequency between the in-phase and the out-of-phase mode can be used as an objective function for design optimization. This is an advantage as a modal analysis requires less computational effort compared to a harmonic analysis.

The eigenfrequencies of these modes are dependent on the boundary conditions of the transducer elements and hence on the backing of the phased array transducer. Thus, the particular dynamic behavior of the backing is identified to have a high influence on mechanical cross-coupling. In order to achieve compact phased array transducers with weak cross-coupling, a new approach employing stop band material as backing is introduced. Therefore, a large number of resonators are attached to the downside of the backing forming a resonant stop band material. The frequency range of the stop band is tuned by trimming the resonator length. It is shown that mechanical cross-coupling can be reduced significantly in case the frequency range of the stop band coincides with the operating frequency of the phased array transducer elements. The influence of the backing on mechanical cross-coupling is investigated in several studies, e.g. [57, 55]. The possibility to reduce it by inserting kerfs and perforations into the backing is shown in the studies of Celmer et al. [56]. The approach of using resonant stop band material as backing offers a new possibility to reduce the mechanical cross-coupling significantly. It can be easily adopted to various phased array ultrasonic transducers by tuning the frequency range of the stop band to the operating frequency. In comparison to various approaches which modify the excitation signal, e.g. [63, 64, 66–69], the presented approach in this work is suitable to reduce mechanical cross-coupling in sound emission and reception mode. The limitations of the proposed solution is mainly related to the manufacturability. However, this limitation holds in general for the realization of resonant stop band approaches.

Summarizing the result discussion, it can be stated that all approaches presented in this work show good prospects to enhance the performance of ultrasonic transducers. As stated in the discussion of the individual approaches, the manufacturability and reproducibility are key factors to realize the shown prospects and to bring the introduced approaches into real industrial applications.

Chapter 6

Conclusion

The presented work contributes to the field of structural dynamics and acoustics of ultrasonic transducers. New approaches for single, multi-frequency, and phased-array transducers are investigated with regard to increase the performance of surround sensing systems. Finally, this work is guided by three research questions.

The first research question addresses the realization of anisotropic directivity patterns in ultrasonic transducers. In order to increase the surround sensing performance, anisotropic directivity patterns with wide angled sound radiation in horizontal direction and narrow angled sound radiation in vertical direction are required. Thus, early ground reflections are avoided and at the same time a comprehensive field of view is obtained. Known approaches from literature employ asymmetric topologies of the ultrasonic transducer to achieve the desired behavior. This results in a limitation of the reachable anisotropy factor within the given sensor dimensions. The approach presented in this work opens up a new design space to overcome this limitation. Therefore, fiber reinforced composites are used to realize the ultrasonic transducer. The introduction of locally structured fiber reinforcements leads to sections with and without fiber reinforcement. Consequently, the material properties can be varied within a monolithic structure. This approach is suitable to achieve highly anisotropic directivity patterns in ultrasonic transducers with a rotationally symmetric geometry. Finally, the field of view of ultrasonic transducers can be enhanced resulting in a better surround sensing performance.

Besides an enhanced field of view, the number of applied ultrasonic transducers increases continuously. In order to operate a high number of transducers in short intervals or in parallel, a signal discrimination by frequency filtering is desired. Multi-frequency ultrasonic transducers allow such a discrimination. However, known approaches from literature suffer at least from one of two disadvantages. They employ multiple electro-mechanical coupling elements which lead to more complex electronics or they show sound radiation behavior which is not suitable for surround sensing applications at multiple operating frequencies, or both. The approach presented in this work offers a solution to design multi-frequency transducers having only one electro-mechanical coupling element and exhibiting suitable sound radiation properties at multiple well separated operating frequencies. To do so, the concept of spatially distributed stop band material is introduced. The first operating frequency does not coincide with the frequency of the stop band. Thus, the structure shows an operational deflection shape similar to that from state of the art ultrasonic transducers. Additionally, a particular operational deflection shape is obtained in case the operating frequency coincides with the frequency range of the stop band. The manner of the operational deflection shape is similar to that at the first operating frequency and suitable sound radiation properties are achieved. Finally, the above mentioned drawbacks of known concepts can be overcome with the presented approach.

Compared to the previous discussed transducer concepts, phased array transducers offer an even better performance in surround sensing applications. Thus, it is possible to obtain real 3D information instead of only the distance between the transducer and an obstacle. The technology of phased array transducers is well-known and applied in medical ultrasonic application and non destructive testing. However, the design of compact, air-coupled, low frequency phased array transducers leads to major design challenges. In the presented work, the issue of mechanical cross-coupling caused by a common backing is addressed. The cause-effect relationship between the particular dynamic behavior of the backing and mechanical cross-coupling is investigated. To overcome this design issue, an approach which employs stop band material is introduced in order to reduce mechanical cross-coupling. It is shown that stop band material as backing has a good prospect to reduce mechanical cross-coupling in compact, air-coupled, low frequency phased array transducers.

Based on the developed approaches in this work, it is possible to design ultrasonic transducers with an increased and more reliable performance. Thus, a more comprehensive surround sensing is possible which can be used to increase safety in automotive, robotic, and industrial applications.

Bibliography

[1] C. Chilowsky and P. Langevin. Procédés et appareils pour la production de signaux sous-marins dirigs et pour la localisation à distance d'obstacles sous-marins. République Françe, Office national de la propriété industrielle 502,913, 1920.

[2] C. Chilowsky and P. Langevin. Production of submarine signals and the location of submarine objects. United States Patent 1,471,547, 1923.

[3] M. J. Wohlgemuth, J. Luo, and C. F. Moss. Three-dimensional auditory localization in the echolocating bat. *Current Opinion in Neurobiology*, 41:78 – 86, 2016.

[4] K. Graff. *A History of Ultrasonics*, volume 15 of *Physical Acoustics*. Academic Press. Inc., Department of Engineering Mechanics, State University, 1981.

[5] J. Curie and P. Curie. Développement, par pression, de l'électricité polaire dans les cristaux hémièdres à faces inclinées. *Comptes Rendus de l'Académie des Sciences*, 91:294–295, 1880.

[6] Deutsches Institut für Normung (German Institute for Standardization). DIN 1320: Akustik - Begriffe (Acoustical terms), 2009.

[7] R. Lerch, G. Sessler, and D. Wolf. *Technische Akustik: Grundlagen und Anwendungen*. Springer Berlin Heidelberg, 2009.

[8] M. Möser. *Engineering Acoustics : An Introduction to Noise Control*. Springer, 2. ed., 2009.

[9] H. E. Bass. Study of sound absorption in air. Technical report, U.S. Army Research Office, 1976.

[10] H. E. Bass and F. D. Shields. Absorption of sound in air: High-frequency measurements. *Journal of the Acoustical Society of America*, 62(3):571–576, 1977.

[11] L. J. Bond, C. Chiang, and C. M. Fortunko. Absorption of ultrasonic waves in air at high frequencies (10-20 MHz). *The Journal of the Acoustical Society of America*, 92(4):2006–2015, 1992.

[12] M. Karl. Verfahren und Einrichtung zur Umfelderfassung eines Bewegungshilfsmittels mittels von pulsförmig ausgesendeten Schallsignalen. Deutsches Patent- und Markenamt, Offenlegungsschrift, DE102011088225A1, 2013.

[13] Z. Gui, X. Hu, and L. Li. Design and analysis of a piezoelectric ultrasonic transducer for distance measurement. In *Proceedings of the 13th IEEE International Symposium on Applications of Ferroelectrics*, pages 335–338, 2002.

[14] W. M. Rubio, F. Buiochi, J. C. Adamowski, and E. C. N. Silva. Modeling of functionally graded piezoelectric ultrasonic transducers. *Ultrasonics*, 49(4):484 – 494, 2009.

[15] J. M. Kocbach. *Finite element modelling of ultrasonic piezoelectric transducers. Influence of geometry and material parameters on vibration response functions and radiated field.* PhD thesis, University of Bergen; Department of Physics, 2000.

[16] R. Sharma, R. Agarwal, A. K. Dubey, and A. Arora. Pragmatics of capacitive micromachined ultrasonic transducer. In *International Conference on Emerging Trends in Computing and Communication Technologies (ICETCCT)*, pages 1–4, 2017.

[17] E. Gelhard. Sensor for distance measurement by ultrasound. United States Patent 4,437,032, 1984.

[18] P. Rapps, P. Knoll, F. Pachner, M. Noll, and M. Fischer. Ultrasonic transducer. United States Patent 5,446,332, 1995.

[19] J. H. Ho, C. C. Cheng, N. T. Tsou, C. S. Chen, J. Shieh, C. K. Lee, and W. J. Wu. Ultrasonic transmitters far field beam pattern altering with boundary conditions design. In *IEEE 16th International Symposium on the Applications of Ferroelectrics*, pages 738–741, 2007.

[20] C.-C. Cheng, C.-Y. Lin, W.-J. Wu, K.-C. Wu, and C.-K. Lee. Highly anisotropic beam patterns for a pot-like ultrasonic sensor with penetrating slots configuration. In *IEEE International Ultrasonics Symposium*, pages 775–778, 2009.

[21] F. P. Bundy. Characteristics of stepped-frequency transducer elements. *The Journal of the Acoustical Society of America*, 20(3):297–304, 1948.

[22] I. Ostrovskii and L. Cremaldi. Split-mode ultrasonic transducer. *The Journal of the Acoustical Society of America*, 134(2):1715–1723, 2013.

[23] T. Wang and C. Lee. Electrically switchable multi-frequency piezoelectric micromachined ultrasonic transducer (pMUT). In *IEEE 29th International Conference on Micro Electro Mechanical Systems (MEMS)*, pages 1106–1109, 2016.

[24] M. Maadi and R. J. Zemp. Self and mutual radiation impedances for modeling of multi-frequency CMUT arrays. *IEEE Transactions on Ultrasonics, Ferroelectrics, and Frequency Control*, 63(9):1441–1454, 2016.

[25] R. Chopra, C. Luginbuhl, F. S. Foster, and M. J. Bronskill. Multifrequency ultrasound transducers for conformal interstitial thermal therapy. *IEEE Transactions on Ultrasonics, Ferroelectrics, and Frequency Control*, 50(7):881–889, 2003.

[26] M. Burtnyk, W. A. N'Djin, L. Persaud, M. Bronskill, and R. Chopra. Acoustic characterization of multi-element, dual-frequency transducers for high-intensity contact ultrasound therapy. *AIP Conference Proceedings*, 1481(1):26–31, 2012.

[27] I. Muttakin, S. M. Nooh, and E. Supriyanto. Spice modeling of hybrid multi-frequency ultrasound transducer. In *Proceedings of the 10th WSEAS International Conference on System Science and Simulation in Engineering*, pages 106–111, Stevens Point, Wisconsin, USA, 2011. World Scientific and Engineering Academy and Society (WSEAS).

[28] I. Muttakin, N. Muhamad Arif, S. M. Nooh, and E. Supriyanto. Analog spice implementation of multi-frequency ultrasound system. *International Journal of Circuits, Systems and Signal Processing*, 6:113–121, 2012.

[29] C. Sun, F. Dai, S. Jiang, and Y. Liu. A novel single-element dual-frequency ultrasound transducer for image-guided precision medicine. In *IEEE International Ultrasonics Symposium*, pages 1–4, 2017.

[30] L. Schmerr. *Fundamentals of Ultrasonic Phased Arrays*. Solid Mechanics and Its Applications. Springer International Publishing, 2014.

[31] B. D. V. Veen and K. M. Buckley. Beamforming: a versatile approach to spatial filtering. *IEEE ASSP Magazine*, 5(2):4–24, 1988.

[32] R. L. Baer and G. S. Kino. Theory for cross coupling in ultrasonic transducer arrays. *Applied Physics Letters*, 44(10):954, 1984.

[33] W. Lee and Y. Roh. Optimal design of a piezoelectric 2D array transducer to minimize the cross talk between active elements. In *IEEE International Ultrasonics Symposium*, pages 2738–2741, 2009.

[34] C. DeSilets. *Transducer Arrays Suitable for Acoustic Imaging*. PhD thesis, Stanford Univ., CA., 1978.

[35] J. Dias. An experimental investigation of the cross-coupling between elements of an acoustic imaging array transducer. *Ultrasonic Imaging*, 4(1):44–55, 1982.

[36] J. D. Larson. Non-ideal radiators in phased array transducers. In *Ultrasonics Symposium*, pages 673–684, 1981.

[37] J. Assaad and C. Bruneel. Influence of interaction between elementary transducer on directivity pattern of an array. *Ultrasonics*, 34(2):107 – 110, 1996.

[38] J. S. Bird, S. Asadov, and P. Kraeutner. Improving arrays for multi-angle swath bathymetry. In *Proceedings of Oceans 2003*, volume 4, pages 2085–2092 Vol.4, 2003.

[39] R. Swartz and J. Plummer. Integrated silicon-PVF2 acoustic transducer arrays. *IEEE Transactions on Electron Devices*, 26(12):1921–1931, 1979.

[40] J. H. Mo, A. L. Robinson, D. W. Fitting, F. L. Terry, and P. L. Carson. A micromachined diaphragm structure for integrated ultrasound transducers. In *Proceedings IEEE Ultrasonics Symposium*, pages 801–804 vol.2, 1989.

[41] J. H. Mo, J. B. Fowlkes, A. L. Robinson, and P. L. Carson. Crosstalk reduction with a micromachined diaphragm structure for integrated ultrasound transducer arrays. *IEEE Transactions on Ultrasonics, Ferroelectrics, and Frequency Control*, 39(1):48–53, 1992.

[42] R. L. Goldberg, M. J. Jurgens, D. M. Mills, C. S. Henriquez, D. Vaughan, and S. W. Smith. Modeling of piezoelectric multilayer ceramics using finite element analysis. *IEEE Transactions on Ultrasonics, Ferroelectrics, and Frequency Control*, 44(6):1204–1214, 1997.

[43] H. Mohamed, D. Polla, E. Ebbini, and S. Zurn. Micromachined piezoelectric ultrasonic imaging transducer. In *Microelectromechanical Systems Conference*, pages 95–98, 2001.

[44] J. T. Yen, C. H. Seo, S. I. Awad, and J. S. Jeong. A dual-layer transducer array for 3-d rectilinear imaging. *IEEE Transactions on Ultrasonics, Ferroelectrics, and Frequency Control*, 56(1):204–212, 2009.

[45] S. Harput and A. Bozkurt. Ultrasonic phased array device for acoustic imaging in air. *IEEE Sensors Journal*, 8(11):1755–1762, 2008.

[46] S. Harput, A. Bozkurt, and F. Y. Yamaner. Ultrasonic phased array device for real-time acoustic imaging in air. In *IEEE Ultrasonics Symposium*, pages 619–622, 2008.

[47] R. J. Kazys, R. Sliteris, and J. Sestoke. Development of air-coupled low frequency ultrasonic transducers and arrays with pmn-32 In *IEEE International Ultrasonics Symposium*, pages 1–4, 2015.

[48] R. J. Kazys, R. Sliteris, and J. Sestoke. Air-coupled low frequency ultrasonic transducers and arrays with pmn-32% pt piezoelectric crystals. *Sensors*, 17(1), 2017.

[49] E. Konetzke, M. Rutsch, M. Hoffmann, A. Unger, R. Golinske, D. Killat, S. N. Ramadas, S. Dixon, and M. Kupnik. Phased array transducer for emitting 40-khz air-coupled ultrasound without grating lobes. In *IEEE International Ultrasonics Symposium*, pages 1–4, 2015.

[50] M. Rutsch, E. Konetzke, A. Unger, M. Hoffmann, S. N. Ramadas, S. Dixon, and M. Kupnik. Extending the receive performance of phased ultrasonic transducer arrays in air down to 40 khz and below. In *IEEE International Ultrasonics Symposium*, pages 1–4, 2015.

[51] X. Jin, I. Ladabaum, F. L. Degertekin, S. Calmes, and B. T. Khuri-Yakub. Fabrication and characterization of surface micromachined capacitive ultrasonic immersion transducers. *Journal of Microelectromechanical Systems*, 8(1):100–114, 1999.

[52] X. Jin, O. Oralkan, F. L. Degertekin, and B. T. Khuri-Yakub. Characterization of one-dimensional capacitive micromachined ultrasonic immersion transducer arrays. *IEEE Transactions on Ultrasonics, Ferroelectrics, and Frequency Control*, 48(3):750–760, 2001.

[53] A. Bozkurt, F. L. Degertekin, A. Atalar, and B. T. Khuri-Yakub. Analytic modeling of loss and cross-coupling in capacitive micromachined ultrasonic transducers. In *IEEE Ultrasonics Symposium*, volume 2, pages 1025–1028, 1998.

[54] M. Hofer, M. Kaltenbacher, R. Peipp, H. Landes, M. Fuldner, and R. Lerch. Cae environment for the design of capacitive micromachined sound and ultrasound transducers. In *IEEE Symposium on Ultrasonics*, volume 2, pages 1975–1978 Vol.2, 2003.

[55] M. Celmer and K. Opieliński. Research and modeling of mechanical crosstalk in linear arrays of ultrasonic transducers. *Archives of Acoustics*, 41(3):599–612, 2016.

[56] M. Celmer, K. Opieliński, and M. Dopierała. Structural model of standard ultrasonic transducer array developed for fem analysis of mechanical crosstalk. *Ultrasonics*, 2017.

[57] S. M. Ji, J. H. Sung, C. Y. Park, and J. S. Jeong. Phase-canceled backing structure for lightweight ultrasonic transducer. *Sensors and Actuators A: Physical*, 260:161 – 168, 2017.

[58] H. C. Yang, J. Cannata, J. Williams, and K. K. Shung. Crosstalk reduction for high-frequency linear-array ultrasound transducers using 1-3 piezocomposites with pseudo-random pillars. *IEEE Transactions on Ultrasonics, Ferroelectrics, and Frequency Control*, 59(10), 2012.

[59] B. T. Khuri-Yakub, G. G. Yaralioglu, B. Bayram, and M. Kupnik. 5f-4 acoustic crosstalk reduction method for cmut arrays. In *IEEE Ultrasonics Symposium*, pages 590–593, 2006.

[60] E. Stytsenko, N. L. Scott, and M. Meijer. Acoustic coupling in linear arrays. In *OCEANS 2016 - Shanghai*, pages 1–7, 2016.

[61] Y. Roh and B. T. Khuri-Yakub. Finite element analysis of underwater capacitor micro-machined ultrasonic transducers. *IEEE Transactions on Ultrasonics, Ferroelectrics, and Frequency Control*, 49(3):293–298, 2002.

[62] Y. Roh and Y. Kim. Analysis and reduction of the cross talk in micro-machined piezoelectric ultrasonic transducers. In *Advances in Nondestructive Evaluation*, volume 270 of *Key Engineering Materials*, pages 1071–1076. Trans Tech Publications, 2004.

[63] B. Cugnet, A.-C. Hladky, and J. Assaad. Numerical technique to reduce cross-coupling in acoustical arrays. *Ultrasonics*, 40(1-8):503 – 506, 2002.

[64] A. Bybi, S. Grondel, J. Assaad, and A.-C. Hladky-Hennion. Extension of the crosstalk cancellation method in ultrasonic transducer arrays from the harmonic regime to the transient one. *Ultrasonics*, 54(2):720 – 724, 2014.

[65] A. Bybi, S. Grondel, J. Assaad, A.-C. Hladky-Hennion, C. Granger, and M. Rguiti. Reducing crosstalk in array structures by controlling the excitation voltage of individual elements: A feasibility study. *Ultrasonics*, 53(6):1135 – 1140, 2013.

[66] A. Bybi, C. Granger, S. Grondel, A.-C. Hladky-Hennion, and J. Assaad. Electrical method for crosstalk cancellation in transducer arrays. *NDT & E International*, 62:115 – 121, 2014.

[67] Q. Meng, Q. Liang, and J. Li. Frequency-hopping pseudo-random pulse width modulation to eliminate crosstalk of sonar sensors in mobile robots. In *IEEE/RSJ International Conference on Intelligent Robots and Systems*, pages 2465–2470, 2006.

[68] S. Zhou, G. L. Wojcik, and J. A. Hossack. An approach for reducing adjacent element crosstalk in ultrasound arrays. *IEEE Transactions on Ultrasonics, Ferroelectrics, and Frequency Control*, 50(12):1752–1761, 2003.

[69] S. Zhou and J. A. Hossack. Reducing inter-element acoustic crosstalk in capacitive micromachined ultrasound transducers. *IEEE Transactions on Ultrasonics, Ferroelectrics, and Frequency Control*, 54(6):1217–1228, 2007.

[70] V. G. Veselago. The electrodynamics of substances with simultaneously negative values of ε and μ. *Soviet Physics Uspekhi*, 10(4):509, 1968.

[71] J. B. Pendry, A. J. Holden, W. J. Stewart, and I. Youngs. Extremely low frequency plasmons in metallic mesostructures. *Phys. Rev. Lett.*, 76:4773–4776, 1996.

[72] R. V. Craster and S. Guenneau, editors. *Acoustic Metamaterials - Negative Refraction, Imaging, Lensing and Cloaking*. Springer, Dordrecht, 2013.

[73] H.-T. Chen, A. J. Taylor, and N. Yu. A review of metasurfaces: Physics and applications. *Reports on Progress in Physics*, 79(7), 2016.

[74] J. Pendry. Negative refraction. *Contemporary Physics*, 45(3):191–202, 2004.

[75] Z. Liu, X. Zhang, Y. Mao, Y. Y. Zhu, Z. Yang, C. T. Chan, and P. Sheng. Locally resonant sonic materials. *Science*, 289(5485):1734–1736, 2000.

[76] M. Strasberg and D. Feit. Vibration damping of large structures induced by attached small resonant structures. *Journal of the Acoustical Society of America*, 99:335–344, 1996.

[77] B. Banerjee. *An Introduction to Metamaterials and Waves in Composites*. CRC Press, 1 ed., 2011.

[78] N. Kaina, F. Lemoult, M. Fink, and G. Lerosey. Ultra small mode volume defect cavities in spatially ordered and disordered metamaterials. *Applied Physics Letters*, 102(14):144104, 2013.

[79] M. Rupin, F. Lemoult, G. Lerosey, and P. Roux. Experimental demonstration of ordered and disordered multiresonant metamaterials for lamb waves. *Phys. Rev. Lett.*, 112:234301, 2014.

[80] C. Sugino, Y. Xia, S. Leadenham, M. Ruzzene, and A. Erturk. A general theory for bandgap estimation in locally resonant metastructures. *Journal of Sound and Vibration*, 406:104 – 123, 2017.

[81] C. C. Claeys, K. Vergote, P. Sas, and W. Desmet. On the potential of tuned resonators to obtain low-frequency vibrational stop bands in periodic panels. *Journal of Sound and Vibration*, 323:1418–1436, 2013.

[82] R. H. Olsson III, I. F. El-Kady, M. F. Su, M. R. Tuck, and J. G. Fleming. Microfabricated {VHF} acoustic crystals and waveguides. *Sensors and Actuators A: Physical*, 145-146:87 – 93, 2008.

[83] Y. Lai, Y. Wu, P. Sheng, and Z.-Q. Zhang. Hybrid elastic solids. *Nature Materials*, 10(8): 620–624, 2011.

[84] Y. Xiao, J. Wen, and X. Wen. Flexural wave band gaps in locally resonant thin plates with periodically attached spring-mass resonators. *Journal of Physics D: Applied Physics*, 45 (19):195401, 2012.

[85] Y. Xiao, J. Wen, and X. Wen. Sound transmission loss of metamaterial-based thin plates with multiple subwavelength arrays of attached resonators. *Journal of Sound and Vibration*, 331(25):5408 – 5423, 2012.

[86] M. Oudich, B. Djafari-Rouhani, Y. Pennec, M. B. Assouar, and B. Bonello. Negative effective mass density of acoustic metamaterial plate decorated with low frequency resonant pillars. *Journal of Applied Physics*, 116(18):184504, 2014.

[87] B. Assouar, M. Oudich, and X. Zhou. Acoustic metamaterials for sound mitigation. *Comptes Rendus Physique*, 17(5):524 – 532, 2016.

[88] C. C. Claeys, P. Sas, and W. Desmet. On the acoustic radiation efficiency of local resonance based stop band materials. *Journal of Sound and Vibration*, 333:3203–3213, 2014.

[89] Y. Song, L. Feng, J. Wen, D. Yu, and X. Wen. Reduction of the sound transmission of a periodic sandwich plate using the stop band concept. *Composite Structures*, 128:428 – 436, 2015.

[90] C. Claeys, E. Deckers, B. Pluymers, and W. Desmet. A lightweight vibro-acoustic metamaterial demonstrator: Numerical and experimental investigation. *Mechanical Systems and Signal Processing*, 70:853 – 880, 2016.

[91] H. Ruiz, C. Claeys, E. Deckers, and W. Desmet. Numerical and experimental study of the effect of microslits on the normal absorption of structural metamaterials. *Mechanical Systems and Signal Processing*, 70-71:904 – 918, 2016.

[92] M. Lewińska, V. Kouznetsova, J. van Dommelen, A. Krushynska, and M. Geers. The attenuation performance of locally resonant acoustic metamaterials based on generalised viscoelastic modelling. *International Journal of Solids and Structures*, 126(Supplement C): 163 – 174, 2017.

[93] Y. Wu, K. Yu, L. Yang, R. Zhao, X. Shi, and K. Tian. Effect of thermal stresses on frequency band structures of elastic metamaterial plates. *Journal of Sound and Vibration*, 413 (Supplement C):101 – 119, 2018.

[94] A. Kruisová, M. Ševčík, H. Seiner, P. Sedlák, B. Román-Manso, P. Miranzo, M. Belmonte, and M. Landa. Ultrasonic bandgaps in 3d-printed periodic ceramic microlattices. *Ultrasonics*, 82:91 – 100, 2018.

[95] H. Peng, P. F. Pai, and H. Deng. Acoustic multi-stopband metamaterial plates design for broadband elastic wave absorption and vibration suppression. *International Journal of Mechanical Sciences*, 103:104 – 114, 2015.

[96] M. Chen, D. Meng, H. Zhang, H. Jiang, and Y. Wang. Resonance-coupling effect on broad band gap formation in locally resonant sonic metamaterials. *Wave Motion*, 63:111 – 119, 2016.

[97] C. Claeys, N. G. Rocha de Melo Filho, L. Van Belle, E. Deckers, and W. Desmet. Design and validation of metamaterials for multiple structural stop bands in waveguides. *Extreme Mechanics Letters*, 12:7–22, 2016.

[98] N. F. Melo, C. Claeys, E. Deckers, B. Pluymers, and W. Desmet. Dynamic metamaterials for structural stopband creation. *SAE Int. J. Passeng. Cars - Mech. Syst.*, 9:1013–1019, 2016.

[99] G. Trainiti, J. Rimoli, and M. Ruzzene. Wave propagation in periodically undulated beams and plates. *International Journal of Solids and Structures*, 75:260 – 276, 2015.

[100] N. Olhoff, B. Niu, and G. Cheng. Optimum design of band-gap beam structures. *International Journal of Solids and Structures*, 49(22):3158 – 3169, 2012.

[101] L. Lu, T. Yamamoto, M. Otomori, T. Yamada, K. Izui, and S. Nishiwaki. Topology optimization of an acoustic metamaterial with negative bulk modulus using local resonance. *Finite Elements in Analysis and Design*, 72:1 – 12, 2013.

[102] T. Matsuki, T. Yamada, K. Izui, and S. Nishiwaki. Topology optimization for locally resonant sonic materials. *Applied Physics Letters*, 104(19):191905, 2014.

[103] J. He and Z. Kang. Achieving directional propagation of elastic waves via topology optimization. *Ultrasonics*, 82:1 – 10, 2018.

[104] J. Li, W. Wang, Y. Xie, B.-I. Popa, and S. A. Cummer. A sound absorbing metasurface with coupled resonators. *Applied Physics Letters*, 109(9):091908, 2016.

[105] X.-P. Wang, L.-L. Wan, T.-N. Chen, A.-L. Song, and X.-W. Du. Broadband reflected wavefronts manipulation using structured phase gradient metasurfaces. *AIP Advances*, 6(6): 065320, 2016.

[106] G. Ma, M. Yang, S. Xiao, Z. Yang, and P. Sheng. Acoustic metasurface with hybrid resonances. *Nat. Mater.*, 13(9):873–878, 2014.

[107] A. Ba, A. Lavie, and A. Leblanc. Soft 3d printed membrane type-acoustic metamaterials. In *23rd International Congress on Sound and Vibration: From Ancient to Modern Acoustics*, 2016.

[108] F. Langfeldt, J. Riecken, W. Gleine, and O. von Estorff. A membrane-type acoustic metamaterial with adjustable acoustic properties. *Journal of Sound and Vibration*, 373:1 – 18, 2016.

[109] X. Wang, H. Zhao, X. Luo, and Z. Huang. Membrane-constrained acoustic metamaterials for low frequency sound insulation. *Applied Physics Letters*, 108(4):041905, 2016.

[110] M. M. Sigalas. Elastic wave band gaps and defect states in two-dimensional composites. *The Journal of the Acoustical Society of America*, 101(3):1256–1261, 1997.

[111] Z.-J. Yao, G.-L. Yu, Y.-S. Wang, and Z.-F. Shi. Propagation of bending waves in phononic crystal thin plates with a point defect. *International Journal of Solids and Structures*, 46 (13):2571 – 2576, 2009.

[112] K.-C. Chuang, Z.-Q. Zhang, and H.-X. Wang. Experimental study on slow flexural waves around the defect modes in a phononic crystal beam using fiber bragg gratings. *Physics Letters A*, 380(47):3963 – 3969, 2016.

[113] M. Gonçalves and F. Margarido. *Materials for Construction and Civil Engineering: Science, Processing, and Design*. Springer International Publishing, 2015.

[114] H. Schroeder. *Lehmbau: Mit Lehm ökologisch planen und bauen*. SpringerLink : Bücher. Springer Fachmedien Wiesbaden, 2013.

[115] *Die Bibel oder die ganze Heilige Schrift des Alten und Neuen Testaments nach der deutschen Übersetzung D. Martin Luthers*. Privilegierte Württembergische Bibelanstalt, Stuttgart.

[116] J. Rösler, H. Harders, and M. Bäker. *Mechanisches Verhalten Der Werkstoffe*. Springer Fachmedien Wiesbaden, 2012.

[117] C. Cherif. *Textile Materials for Lightweight Constructions: Technologies - Methods - Materials - Properties*. Springer Berlin Heidelberg, 2016.

[118] C. Cherif. *Textile Werkstoffe für den Leichtbau: Techniken - Verfahren - Materialien - Eigenschaften*. SpringerLink : Bücher. Springer Berlin Heidelberg, 2011.

[119] H. Schürmann. *Konstruieren mit Faser-Kunststoff-Verbunden*. Springer Berlin Heidelberg, 2007.

[120] J. Halpin. Stiffness and expansion estimates for oriented short fiber composites. *Journal of Composite Materials*, 3(4):732–734, 1969.

[121] J. C. Halpin and J. L. Kardos. The halpin-tsai equations: A review. *Polymer Engineering & Science*, 16(5):344–352, 1976.

[122] R. Foye. The transverse poisson's ratio of composites. *Journal of Composite Materials*, 6 (2):293–295, 1972.

[123] E. Jacquet, F. Trivaudey, and D. Varchon. Calculation of the transverse modulus of a unidirectional composite material and of the modulus of an aggregate. application of the rule of mixtures. *Composites Science and Technology*, 60(3):345 – 350, 2000.

[124] R. Akkerman. Laminate mechanics for balanced woven fabrics. *Composites Part B: Engineering*, 37(2):108 – 116, 2005.

[125] J. Summerscales. The bulk modulus of carbon fibers. *Journal of Materials Science Letters*, 19(1):15–16, 2000.

[126] B. Pal and M. R. Haseebuddin. Analytical estimation of elastic properties of polypropylene fiber matrix composite by finite element analysis. *Advances in Materials Physics and Chemistry*, Vol.02No.01:8, 2012.

[127] R. W. Clough. The finite element method in plane stress analysis. In *Second Conference on Electronic Computation, Pittsburgh*, pages 345–378. American Society of Civil Engineers, 1960.

[128] D. V. Hutton. *Fundamentals of finite element analysis.* McGraw-Hill series in mechanical engineering. McGraw-Hill, 2004.

[129] K. Bathe. *Finite Element Procedures*. Prentice Hall, second ed., 2014.

[130] O. C. Zienkiewicz and R. L. Taylor. *The Finite Element Methode Volume 1: The Basis*. Butterworth-Heinemann, fifth edition ed., 2000.

[131] B. Parlett. *The Symmetric Eigenvalue Problem.* Society for Industrial and Applied Mathematics, 1998.

[132] B. N. Parlett and B. Nour-Omid. Towards a black box lanczos program. *Computer Physics Communications*, 53(1):169 – 179, 1989.

[133] H. Simon. The lanczos algorithm with partial reorthogonalization. *Mathematics of Computation*, 42(165):115–142, 1984.

[134] R. G. Grimes, J. G. Lewis, and S. H. D. A shifted block lanczos algorithm for solving sparse symmetric generalized eigenproblems. *SIAM Journal on Matrix Analysis and Applications*, 15(1):228, 1994.

[135] K. J. Bathe and E. L. Wilson. Large eigenvalue problems in dynamic analysis. *ASCE Journal of the Engineering Mechanics Division*, 98(EM6):9433, 1471–1485, 1972.

[136] K.-J. Bathe and E. L. Wilson. Solution methods for eigenvalue problems in structural mechanics. *International Journal for Numerical Methods in Engineering*, 6(2):213–226, 1973.

[137] K.-T. Kim and K.-J. Bathe. The bathe subspace iteration method enriched by turning vectors. *Computers & Structures*, 186:11 – 21, 2017.

[138] F. Bloch. Über die Quantenmechanik der Elektronen in Kristallgittern. *Zeitschrift für Physik*, 52(7-8):555–600, 1929.

[139] J. Henneberg, A. Gerlach, H. Cebulla, and S. Marburg. The potential of stop band material in multi-frequency ultrasonic transducers. *Journal of Sound and Vibration*, 452:132 – 146, 2019.

[140] B. R. Mace and E. Manconi. Modelling wave propagation in two-dimensional structures using finite element analysis. *Journal of Sound and Vibration*, 318(4):884 – 902, 2008.

[141] B. R. Mace, D. Duhamel, M. J. Brennan, and L. Hinke. Finite element prediction of wave motion in structural waveguides. *The Journal of the Acoustical Society of America*, 117(5): 2835–2843, 2005.

[142] L. Brillouin. *Wave Propagation in Periodic Structures: Electric Filters and Crystal Lattices*. Dover Publications, 1953.

[143] F. Maurin, C. Claeys, E. Deckers, and W. Desmet. Probability that a band-gap extremum is located on the irreducible brillouin-zone contour for the 17 different plane crystallographic lattices. *International Journal of Solids and Structures*, 135:26 – 36, 2018.

[144] M. Ruzzene and F. L. Scarpa. A general FEM technique to model wave propagation in cellular periodic structures. In *Proc. SPIE 5053, Smart Structures and Materials: Active Materials: Behavior and Mechanics,*, volume 5053, pages 414 – 422, 2003.

[145] R. Langley. A note on the force boundary conditions for two-dimensional periodic structures with corner freedoms. *Journal of Sound and Vibration*, 167(2):377 – 381, 1993.

[146] J. W. Baron Rayleigh Strutt. *The Theory Of Sound Vol.2*. Dover Publications, 1896.

[147] J. Henneberg, A. Gerlach, H. Cebulla, and S. Marburg. Locally structured fiber reinforcements: An approach to realize anisotropic directivity pattern in ultrasound transducers. In *SAE Technical Paper*, page 13. SAE International, 2018.

[148] S. Marburg. Developments in structural-acoustic optimization for passive noise control. *Archives of Computational Methods in Engineering*, 9(4):291–370, 2002.

[149] M. Möser. *Technische Akustik (Technical acoustics)*. Springer-Verlag, Berlin Heidelberg New York, 10. ed., 2015.

[150] G. Hübner and A. Gerlach. Zusammenhang der DFEM-Schalleistungsbeschreibung mit der Rayleighschen Schallfelddarstellung ebener Strahler. In *Fortschritte der Akustik / DAGA*, pages 682–683, 1998.

[151] D. Ewins. *Modal testing: theory and practice*. Mechanical engineering research studies. Research Studies Press, 1984.

[152] P. Langer, M. Maeder, C. Guist, M. Krause, and S. Marburg. More than six elements per wavelength: The practical use of structural finite element models and their accuracy in comparison with experimental results. *Journal of Computational Acoustics*, 25(4):1750025, 2017.

[153] *Abaqus 6.14 Online Documentation - Abaqus Analysis User's Guide*. Dassault Systemes, 2014.

[154] S. Köllner. Modellbildung und Simulation von Ultraschallwandlern auf Basis von Verbundwerkstoffen (Modelling and simulation of ultrasonic transducers based on composites). Master's thesis, Karlsruhe Institute of Technology, Department of Mechanical Engineering, 2014.

[155] H. Brinson and L. Brinson. *Polymer Engineering Science and Viscoelasticity: An Introduction*. SpringerLink : Bücher. Springer US, 2008.

[156] Deutsches Institut für Normung (German Institute for Standardization). DIN EN 12127: Textiles - Fabrics - Determination of mass per unit area using small samples, 1997.

[157] F. F. Luz, S. C. Amico, J. Á. Souza, E. S. Barbosa, and A. G. B. de Lima. *Numerical Analysis of Heat and Mass Transfer in Porous Media*, volume 27 of *Advanced Structured Materials*, chapter Resin Transfer Molding Process: Fundamentals, Numerical Computation and Experiments, pages 121–151. Springer, Berlin, Heidelberg, 2012.

[158] I. Gibson, D. Rosen, and B. Stucker. *Additive Manufacturing Technologies*. Springer New York, 2015.

[159] Stratasys. Design with brilliance - game-changing versatility and realism with the world's most advanced full-color multi-material 3D printer, 2017.

[160] A. Leissa. *Vibration of Plates*. NASA SP. Scientific and Technical Information Division, National Aeronautics and Space Administration, 1969.

Part II

Appended Papers

Paper A

SAE Technical Paper 2018-01-1485

Locally Structured Fiber Reinforcements: An Approach to Realize Anisotropic Directivity Pattern in Ultrasound Transducers

J. Henneberg[1,2], A. Gerlach[2], H. Cebulla[3], S. Marburg[1]
[1] Technical University of Munich, Chair of Vibroacoustics of Vehicles and Machines
Boltzmann Str. 15, 85748 Garching, Germany
[2] Robert Bosch GmbH,
Robert-Bosch-Campus 1, 71272 Renningen, Germany
[3] Technical University Chemnitz, Professorship for Textile Technologies
Reichenhainer Str. 31/33, 09126 Chemnitz, Germany

Society of Automotive Engineers (SAE) as the copyright holder

Abstract

Ultrasonic transducers are widely used in automotive and industrial applications for surround sensing. Anisotropic directivity patterns with a narrow-angled beam in the vertical plane and a wide-angled beam in the horizontal plane are needed in automotive applications particularly. Today's ultrasonic transducers for automotive applications are mainly metal based, pot-like ultrasonic transducers. The anisotropic directivity pattern is achieved by increasing the thickness of the vibrating plate-like part of the structure locally. Composites with locally structured fiber reinforcements open up the possibility to design the dynamical behavior of components without changing its contour. Using this new dimension of design to modify the directivity pattern of sound radiating components is less examined in literature. In this work, the possibility of creating an anisotropic directivity pattern by locally structuring the fiber reinforcement is investigated using a generic ultrasonic transducer model. The structuring is realized by sections of carbon fiber reinforced epoxy and sections made of epoxy only. Furthermore, the influence of geometrical and material uncertainties of the fiber reinforcement on the directivity pattern is discussed. The authors identify locally structured fiber reinforcements as a suitable possibility to create an anisotropic directivity pattern of an ultrasonic transducer.

Keywords: ultrasonic transducer; anisotropic directivity pattern; fiber reinforced composites; sensitivity analysis

Introduction

Ultrasonic transducers are widely used in automotive and industrial applications for surround sensing. Due to increasing level of automatic driving and robotic applications, there is a huge need for surround sensing sensors. State of the art ultrasonic transducers for automotive applications are metal based, pot-like structures [1]. The electro-mechanical coupling is realized with piezoelectric ceramic elements. To achieve a good performance in terms of the measurement range, these ultrasonic transducers have an anisotropic directivity pattern. They offer a wide angular aperture in horizontal plane and a narrow angular aperture in vertical plane. Thus, disturbing reflections from the ground are reduced. To achieve an anisotropic directivity pattern, several geometrical designs are suggested in [1]. In former studies [2], a method is presented to increase the anisotropy of an ultrasonic transducer. Therefore, penetrating slots are inserted in the cylindrical side wall. The influence of altering boundary conditions on the beam pattern is investigated in [3]. In [4], a possibility is described how to sharpen the directivity of radiated ultrasonic waves in ultrasonic transducer arrays. In [5], the setup and directivity pattern of a thermoacoustic transducer is investigated. Finite element modeling of an axisymmetric piezoelectric ultrasonic transducer is described in [6]. The radiation of ultrasonic waves into a fluid or solid medium is investigated. Therefore, the different modes and the belonging radiated sound fields are calculated.

In this study, a new concept of ultrasonic transducers based on composite materials is investigated. Instead of metal, a fiber reinforced composite is used to form the pot-like structure of the ultrasonic transducer. The electro-mechanical coupling is realized with a piezoelectric ceramic element as known from state of the art ultrasonic transducers. Fiber reinforced composites offer the possibility to design a particular dynamic behavior of structures by modifying the fiber reinforcement. In literature, a couple of studies regarding sound radiation and sound transmission of composite plate are presented, such as [7, 8, 9]. The present study investigates fiber reinforcements with local structuring in order to obtain an ultrasonic transducer with an anisotropic directivity pattern. The structuring is realized by sections with carbon fiber reinforced epoxy and sections made out of epoxy only. In terms of robustness and feasibility, the sensitivity to material and geometrical uncertainties is an import aspect. Thus, the influence of uncertainties is investigated in finite element simulation. A sensitivity analysis is carried out to identify the influence of different parameters on the sound radiation.

In the following section, the applied methods are presented. As the used material model has high significance for locally structured fiber reinforced composites, a focus is set on this topic. In a next step, the investigated models are introduced. Applying finite element methods, the directivity patterns of different designs and its sensitivity to geometrical and material uncertainties is presented. Subsequently, the finite element model is validated by experiments. In the final section, a conclusion is drawn.

Methods

In this section, the applied methods are presented. To carry out numerical simulations with the finite element method, especially the applied material models of the fiber reinforced composite have high importance. Furthermore, the calculation of the directivity pattern and the experimental testing are discussed.

Material model

Material properties and their appropriate description are key elements to investigate locally structured fiber reinforced composites. Composite materials consist at least out of two different materials. Knowing the properties of each component itself, it is possible to calculate the properties of the composite. Therefore, a homogenization approach is applied, also known as the rule of mixtures (ROM) [10]. The focus of this work is on carbon fiber reinforced epoxy. Carbon fibers show anisotropic behavior. Thus, an orthotropic material model is used to predict the dynamical behavior of the carbon fiber reinforced composite. Firstly, the general behavior of an orthotropic material is described. Afterwards the calculation of the required properties is shown for composites with a unidirectional, non-crimp fabric, cf. Fig. 1, and a balanced, woven fabric, cf. Fig. 3.
The general stress-strain relation in an orthotropic material is described by [10]

$$\begin{pmatrix}\varepsilon_1\\ \varepsilon_2\\ \varepsilon_3\\ \gamma_{12}\\ \gamma_{13}\\ \gamma_{23}\end{pmatrix} = \underbrace{\begin{bmatrix} S_{11} & S_{12} & S_{13} & 0 & 0 & 0\\ S_{12} & S_{22} & S_{23} & 0 & 0 & 0\\ S_{13} & S_{23} & S_{33} & 0 & 0 & 0\\ 0 & 0 & 0 & S_{44} & 0 & 0\\ 0 & 0 & 0 & 0 & S_{55} & 0\\ 0 & 0 & 0 & 0 & 0 & S_{66}\end{bmatrix}}_{[\boldsymbol{S}]} \cdot \begin{pmatrix}\sigma_1\\ \sigma_2\\ \sigma_3\\ \tau_{12}\\ \tau_{13}\\ \tau_{23}\end{pmatrix} , \qquad (1)$$

where $[\boldsymbol{S}]$ denotes the compliance matrix. ε, γ, σ, τ denote the normal strain, shear strain, normal stress, and shear stress. Assuming linear elastic behavior, the relation can be described in accordance to Hooke's law with so called engineering constants [11]

$$\begin{pmatrix}\varepsilon_1\\ \varepsilon_2\\ \varepsilon_3\\ \gamma_{12}\\ \gamma_{13}\\ \gamma_{23}\end{pmatrix} = \begin{bmatrix}\boldsymbol{A} & 0\\ 0 & \boldsymbol{B}\end{bmatrix} \cdot \begin{pmatrix}\sigma_1\\ \sigma_2\\ \sigma_3\\ \tau_{12}\\ \tau_{13}\\ \tau_{23}\end{pmatrix} , \qquad (2)$$

with

$$\boldsymbol{A} = \begin{bmatrix} 1/E_1 & -\nu_{21}/E_2 & -\nu_{31}/E_3\\ -\nu_{12}/E_1 & 1/E_2 & -\nu_{32}/E_3\\ -\nu_{13}/E_1 & -\nu_{23}/E_2 & 1/E_3\end{bmatrix} \qquad (3)$$

and

$$\boldsymbol{B} = \begin{bmatrix} 1/G_{12} & 0 & 0\\ 0 & 1/G_{13} & 0\\ 0 & 0 & 1/G_{23}\end{bmatrix} . \qquad (4)$$

Applying the relation $\frac{\nu_{ij}}{E_i} = \frac{\nu_{ji}}{E_j}$, known as the Maxwell-Betti reciprocity relation [10], leads to

$$\mathbf{A} = \begin{bmatrix} 1/E_1 & -\nu_{12}/E_1 & -\nu_{13}/E_1\\ -\nu_{12}/E_1 & 1/E_2 & -\nu_{23}/E_2\\ -\nu_{13}/E_1 & -\nu_{23}/E_2 & 1/E_3\end{bmatrix} . \qquad (5)$$

Thus, 9 material properties of the composite are needed to describe the orthotropic material stress-strain behavior, the Young's moduli E_1, E_2, E_3, the Possion's ratios ν_{12}, ν_{13}, ν_{23}, and the shear moduli G_{12}, G_{13}, G_{23}. The composite density ρ is calculated with the material properties of the single components applying the ROM.

Unidirectional, non-crimp fabric

Unidirectional, non-crimp fabrics are layers with only one axis of fiber orientation. All fibers are orientated in one direction. Therefore, unidirectional, non-crimp fabrics made of carbon fibers show highly anisotropic material properties within one layer. According to the notation of directions implied by Eq. (1), the orientation of the fiber axis is defined coinciding with the direction indicated by 1. Due to the symmetry, normal to direction 1, the number of independent material properties is reduced from 9 to 6 for this composite material. Therefore, it is assumed that $E_2^{\mathrm{UD}} = E_3^{\mathrm{UD}}$, $\nu_{12}^{\mathrm{UD}} = \nu_{13}^{\mathrm{UD}}$, and $G_{12}^{\mathrm{UD}} = G_{13}^{\mathrm{UD}}$. By applying $G_{23}^{\mathrm{UD}} = \frac{E_2^{\mathrm{UD}}}{2(1+\nu_{23}^{\mathrm{UD}})}$, the number of independent material parameters are reduced to 5. Thus, the material model becomes a transversal isotropic material model.

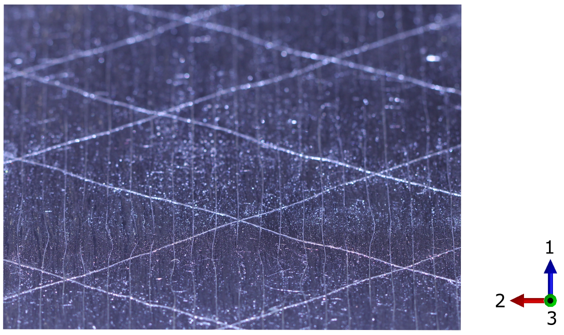

Figure 1: Unidirectional, non-crimp fabric with fiber orientation in direction 1. The thin filaments in shape of a rhombus are sewing filaments which fix the carbon filament to a fabric. The influence on the material properties is neglected.

The mechanical properties can be achieved by applying a rheological model. Fig. 2 shows exemplary the rheological model to obtain the Young's modulus in direction 1. It assumes a parallel circuit out of a spring representing the Young's modulus parallel to the fiber axis $E_{\mathrm{F},\|}$ and a spring representing the Young's modulus of the matrix material E_{M}.

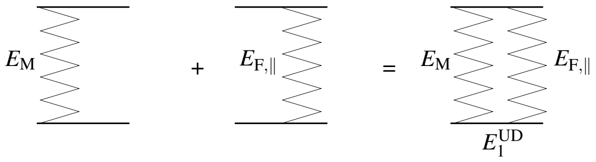

Figure 2: Rheological model of the Young's modulus in direction parallel to the fiber axis for a unidirectional, non-crimp fabric.

The Young's modulus is then calculated by [10]

$$E_1^{\mathrm{UD}} = \Phi E_{\mathrm{F},\|} + (1-\Phi)E_{\mathrm{M}} , \qquad (6)$$

with Φ denoting the overall fiber volume fraction of the composite. The Young's modulus transverse to the fiber direction is calculated using the semi-empircal approach of Puck by [10]

$$E_2^{\mathrm{UD}} = \frac{E_{\mathrm{M}}}{1-\nu_{\mathrm{M}}^2} \frac{1+0.85\Phi^2}{(1-\Phi)^{1.25} + \frac{E_{\mathrm{M}}}{(1-\nu_{\mathrm{M}}^2)E_{\mathrm{F},\perp}}} . \qquad (7)$$

The Poisson's ratio is calculated applying the ROM

$$\nu_{12}^{\mathrm{UD}} = \Phi \nu_{\mathrm{F},12} + (1-\Phi)\nu_{\mathrm{M}} . \qquad (8)$$

The transverse Poisson's ratio ν_{23}^{UD} is obtained by the approach of Foye given in [12]

$$\nu_{23}^{\mathrm{UD}} = \Phi \nu_{\mathrm{F},23} + (1-\Phi)\nu_{\mathrm{M}} \left[\frac{\left(1+\nu_{\mathrm{M}} - \nu_{12}^{\mathrm{UD}} \frac{E_{\mathrm{M}}}{E_1^{\mathrm{UD}}}\right)}{\left(1-\nu_{\mathrm{M}}^2 + \nu_{\mathrm{M}}\nu_{12}^{\mathrm{UD}} \frac{E_{\mathrm{M}}}{E_1^{\mathrm{UD}}}\right)} \right] . \qquad (9)$$

The shear moduli G_{12}^{UD} and G_{13}^{UD} are obtained with the semi-empirical approach of Förster [10]

$$G_{12}^{\mathrm{UD}} = G_{13}^{\mathrm{UD}} = G_{\mathrm{M}} \frac{1+0.4\Phi^{0.5}}{(1-\Phi)^{1.45} + \frac{G_{\mathrm{M}}}{G_{\mathrm{F},12}}\Phi} \,. \tag{10}$$

To obtain the shear modulus $G_{\mathrm{F},12}$ for anisotropic materials, in [13] the following relation is given:

$$G_{\mathrm{F},12} = \frac{\sqrt{E_{\mathrm{F},\parallel}E_{\mathrm{F},\perp}}}{2(1+\sqrt{\nu_{\mathrm{F},12}\nu_{\mathrm{F},21}})} \,. \tag{11}$$

In order to retrieve $\nu_{\mathrm{F},21}$, the Maxwell-Betti relation is applied. Thus, it can be calculated using

$$\nu_{\mathrm{F},21} = \nu_{\mathrm{F},12}\frac{E_{\mathrm{F},\perp}}{E_{\mathrm{F},\parallel}} \,. \tag{12}$$

Due to the assumption of a transversal isotropic material, G_{23}^{UD} is determined by

$$G_{23}^{\mathrm{UD}} = \frac{E_2^{\mathrm{UD}}}{2(1+\nu_{23}^{\mathrm{UD}})} \tag{13}$$

as mentioned before.

Balanced, woven fabric

Woven fabrics are textiles formed on a loom. Three fundamental types of weave construction exist: plain weave, twill weave and satin weave. The investigations in the present study are conducted with a plain weave. It is formed by shedding after every weft insertion. Thus, the warp yarn alternates between lifting and lowering after every weft yarn. By this, the warp and weft yarn are crimped [14]. This has a major effect on the mechanical properties of the woven fabric especially for anisotropic materials like carbon fiber. Balanced, woven fabrics have a ratio of 1 between warp and weft yarn in terms of volume and weight. Thus, the properties in warp and in weft direction are equal. Balanced, woven fabrics show less anisotropic behavior within one layer compared to unidirectional, non-crimp fabrics. The required material properties are reduced from 9 to 6 engineering constants, because of $E_1^{\mathrm{WF}} = E_2^{\mathrm{WF}}$, $\nu_{13}^{\mathrm{WF}} = \nu_{23}^{\mathrm{WF}}$, and $G_{13}^{\mathrm{WF}} = G_{23}^{\mathrm{WF}}$. Please note, it is not a transversal isotropic material model as $G_{12}^{\mathrm{WF}} = \frac{E_1^{\mathrm{WF}}}{2(1+\nu_{12}^{\mathrm{WF}})}$ does not apply [15]. Fig. 3 shows a balanced, plain weave made of carbon fiber.

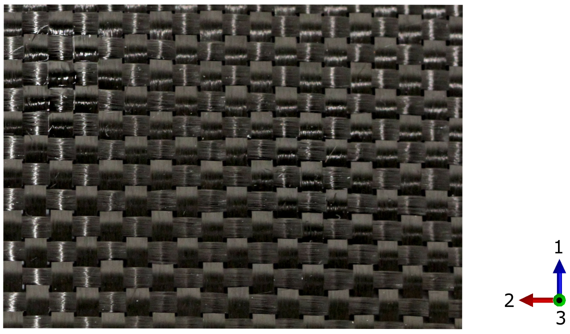

Figure 3: Balanced, plain weave made out of carbon with warp yarn in direction 1 and weft yarn in direction 2.

An orthotropic material model, developed in [16], is applied. Fig. 4 shows the rheological model of the composite to calculate the Young's modulus in direction 1 for a balanced, woven fabric. It assumes a series and parallel circuit of fiber and matrix material properties. The model consists of two springs in series, one of which representing the Young's modulus of the matrix (E_{M}). The second spring in series describes the Young's modulus perpendicular to the fiber axis ($E_{\mathrm{F},\perp}$). In parallel to this series, the Young's modulus of the fiber parallel to its axis ($E_{\mathrm{F},\parallel}$) is assigned.

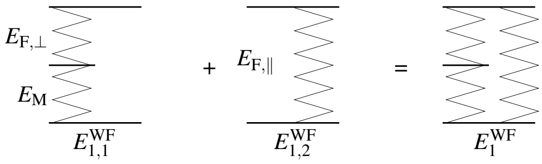

Figure 4: Rheological model to calculate the Young's modulus E_1^{WF} [16].

Applying the ROM, the series of springs is calculated by

$$E_{1,1}^{\mathrm{WF}} = \frac{E_{\mathrm{M}}E_{\mathrm{F},\perp}}{\Phi_{1,1}E_{\mathrm{M}} + (1-\Phi_{1,1})E_{\mathrm{F},\perp}} \,, \tag{14}$$

where $\Phi_{1,1}$ denotes the fiber volume fraction of fibers with an axis orientation perpendicular to the direction 1. In a balanced, woven fabric, it is calculated by

$$\Phi_{1,1} = \frac{\frac{\Phi}{2}}{1-\frac{\Phi}{2}} \,, \tag{15}$$

with Φ representing the overall fiber volume fraction of the composite. The Halpin-Tsai method introduces a semi-empirical approach to take non-uniform strain in the matrix into account [17]. Thus, a correction factor β is inserted into Eq. (14), resulting in

$$E_{1,1}^{\mathrm{WF}} = \frac{\beta E_{\mathrm{M}}E_{\mathrm{F},\perp}}{\Phi_{1,1}\beta E_{\mathrm{M}} + (1-\Phi_{1,1})E_{\mathrm{F},\perp}} \,. \tag{16}$$

Due to the crimp of fibers in a woven fabric, the fiber axis is only in some parts of the fabric parallel to the direction 1. This results in a reduced stiffness in direction 1 for anisotropic materials like carbon. This is considered by introducing a factor of stiffness reduction $\eta \in [0,1]$. The second part of the parallel circuit, cf. Fig. 4, is then calculated by

$$E_{1,2}^{\mathrm{WF}} = \eta E_{\mathrm{F},\parallel} \,. \tag{17}$$

The resulting Young's modulus for the direction 1 is finally calculated by

$$E_1^{\mathrm{WF}} = \frac{\Phi}{2}E_{1,2}^{\mathrm{WF}} + (1-\frac{\Phi}{2})E_{1,1}^{\mathrm{WF}} \,. \tag{18}$$

In direction 3, there exists only a series circuit out of fibers perpendicular to its axis and matrix. Thus, E_3^{WF} is calculated in equivalent to $E_{1,1}^{\mathrm{WF}}$ by

$$E_3^{\mathrm{WF}} = \frac{\beta E_{\mathrm{M}}E_{\mathrm{F},\perp}}{\Phi\beta E_{\mathrm{M}} + (1-\Phi)E_{\mathrm{F},\perp}} \,. \tag{19}$$

Applying the ROM, the Poisson's ratio ν_{12}^{WF} is obtained in the same manner like the Young's moduli by

$$\nu_{12,1}^{\mathrm{WF}} = \frac{\nu_{\mathrm{M}}\nu_{\mathrm{F},21}}{\Phi_{1,1}\nu_{\mathrm{M}} + (1-\Phi_{1,1})\nu_{\mathrm{F},12}} \tag{20}$$

and

$$\nu_{12,2}^{\mathrm{WF}} = \eta\,\nu_{\mathrm{F},12} \tag{21}$$

resulting in

$$\nu_{12}^{\mathrm{WF}} = \frac{\Phi}{2}\nu_{12,2}^{\mathrm{WF}} + (1-\frac{\Phi}{2})\nu_{12,1}^{\mathrm{WF}} \,. \tag{22}$$

To obtain the Poisson's ratio $\nu_{13} = \nu_{23}$, the approach given in [15] is applied. The properties of a balanced, woven fabric are mimicked by unidirectional layers. Thus, Poisson's ratio is calculated by

$$\nu_{13}^{\mathrm{WF}} = E_1^{\mathrm{WF}} \left(\frac{1}{E_1} \frac{E_1(\nu_{12} + \nu_{23} + \nu_{12}\nu_{23}) + \nu_{12}^2}{E_1 + (1 + 2\nu_{12})E_2} \right)^{\mathrm{UD}} . \tag{23}$$

The in-plane shear modulus is obtained in the same way as the Young's moduli.

$$G_{12}^{\mathrm{WF}} = \frac{\beta G_{\mathrm{M}} G_{\mathrm{F},12}}{\Phi \beta G_{\mathrm{M}} + (1 - \Phi) G_{\mathrm{F},12}} . \tag{24}$$

A method to calculate the transverse shear moduli is presented in [15]. It uses equivalent properties of a unidirectional reinforced laminate to obtain G_{13}^{WF} by

$$G_{13}^{\mathrm{WF}} = G_{23}^{\mathrm{WF}} = (\frac{1 + \nu_{23}^{UD}}{E_2^{UD}} + \frac{1}{2G_{12}})^{-1} . \tag{25}$$

Even though, there are certain inaccuracies shown in [15] for the approach given in Eq. (25), the study of [16] shows that the transverse shear modulus has small influence on the dynamical behavior of composites with comparable mode shapes and frequency ranges investigated in the presented study.

Prediction of material properties

To predict the dynamical behavior, material properties of the single raw materials as well as the fiber volume fraction are needed. While the Young's moduli E_M and $E_{\mathrm{F},\|}$ are usually given by the manufacturer, $E_{\mathrm{F},\perp}$ is mostly unknown. For carbon fibers, the ratio of $\frac{E_{\mathrm{F},\|}}{E_{\mathrm{F},\perp}} = 12$ gives an appropriate assumption [16]. In order to predict the fiber-volume ratio, material properties of the fiber reinforcement and geometrical parameters of the structure are needed. A common material property of fabrics is the areal density $\tilde{\rho}_{\mathrm{Fa}}$, also known as area weight. It describes the mass per area of two dimensional structures [18]. Knowing the density of carbon fiber ρ_{F} and the thickness of the structure t_{St}, the fiber volume fraction Φ is calculated by [16]

$$\Phi = \frac{n \tilde{\rho}_{\mathrm{Fa}}}{\rho_{\mathrm{F}} t_{\mathrm{St}}} , \tag{26}$$

where n denotes the number of layers in the structure. The maximum number of layers in the structure is limited by the integer quotient

$$n_{\max} = \frac{t_{\mathrm{St}}}{t_{\mathrm{Fa}}} , \tag{27}$$

with t_{Fa} describing the thickness of the fabric layer.

In the following investigations, the material properties given in table 1 are used.

Table 1: Input parameters for the micro mechanical modeling of the composite.

Epoxy	
E_{M}	3815 MPa
ν_{M}	0.33
ρ_{M}	1.14 $\frac{\mathrm{g}}{\mathrm{cm}^3}$
Balanced, woven fabric	
$E_{\mathrm{F},\|}$	230 GPa
$\nu_{\mathrm{F},12}$	0.33
$\nu_{\mathrm{F},23}$	0.45
ρ_{F}	1.77 $\frac{\mathrm{g}}{\mathrm{cm}^3}$
$\tilde{\rho}_{\mathrm{Fa}}$	204 $\frac{\mathrm{g}}{\mathrm{m}^2}$
t_{Fa}	0.30 mm
η	0.826
Unidirectional, non-crimp fabric	
$E_{\mathrm{F},\|}$	242 GPa
$\nu_{\mathrm{F},12}$	0.33
$\nu_{\mathrm{F},23}$	0.45
ρ_{F}	1.77 $\frac{\mathrm{g}}{\mathrm{cm}^3}$
$\tilde{\rho}_{\mathrm{Fa}}$	396 $\frac{\mathrm{g}}{\mathrm{m}^2}$
t_{Fa}	0.50 mm

Far-field directivity pattern

The directivity pattern of the ultrasonic transducer is calculated in the far-field. This is done performing the Rayleigh integral [19, 20]. The ultrasonic transducer is assumed as a radiator embedded in a flat, infinite, and rigid baffle. For this assumption, the Rayleigh integral gives an exact solution [21]. These boundary conditions are suitable to approximate the directivity pattern for an ultrasonic transducer which is embedded in a car bumper in the final application. In [22], three conditions are mentioned to apply far-field assumptions. Thus, the distance (R) from the radiator to the field point has to be much greater than the dimension (l) of the radiator

$$R \gg l . \tag{28}$$

Furthermore, the condition

$$\frac{l}{\lambda} \ll \frac{R}{l} \tag{29}$$

must be fulfilled in order to keep the error caused by phase shifts smaller than $\frac{\pi}{4}$. Finally, the distance between the radiator and field point should be large compared to the wavelength

$$R \gg \lambda . \tag{30}$$

The Rayleigh integral for a plane surface like a plate can by expressed for $e^{i\omega t}$ harmonic time dependence by [23]

$$p(\vec{y}) = \int_{\Gamma} -i\ \omega\ \rho_{\mathrm{f}}\ G(\vec{x},\vec{y})\ v_{\mathrm{f}}(\vec{x})\ \mathrm{d}\Gamma(\vec{x}) \tag{31}$$

$$\text{with } G(\vec{x},\vec{y}) = \frac{e^{-i\ k\ r}}{2\ \pi\ r} \text{ and } r = |\vec{x} - \vec{y}| , \tag{32}$$

where Γ, ρ_{f}, ω, v_{f}, k, i denote the radiating surface, fluid density, circular frequency, fluid particle velocity, wavenumber, and imaginary unit. In [24], it is shown that the particle velocity distribution on the surface of the structure can be used to estimate the radiated far-field sound pressure. An approximation of the sound pressure in far-field radiated by a plane surface, expressed in spherical coordinates (R, ϑ, φ) is given in [22]

$$
p(R,\vartheta,\varphi) = \frac{i\,\omega\,\rho_{\mathrm{f}}}{2\pi R} e^{-ikR} \cdot \ldots
\cdot \int_{-l_y\backslash 2}^{l_y\backslash 2} \int_{-l_x\backslash 2}^{l_x\backslash 2} e^{i\,k(x_{\mathrm{Q}} \sin\vartheta \cos\varphi + y_{\mathrm{Q}} \sin\vartheta \sin\varphi)}\, v(x_{\mathrm{Q}}, y_{\mathrm{Q}})\, \mathrm{d}x_{\mathrm{Q}}\, \mathrm{d}y_{\mathrm{Q}}\,. \tag{33}
$$

The directivity pattern of the ultrasonic transducer should offer a wide angular aperture in horizontal plane and a narrow angular aperture in vertical plane. In Fig. 5, the final application of an ultrasonic transducer (a) in a car bumper (b) is shown with indication of the vertical (c) and the horizontal (d) angle of aperture. The angle of aperture is defined as the angle at which the sound pressure level is reduced to -6 dB. The referenced sound pressure for the sound pressure level is the maximum radiated sound pressure of the ultrasonic transducer. The angle is defined between a reference axis and a field point axis. The reference axis is perpendicular to the sound radiating surface going through its center point, while the field point axis is defined as the vector between field point and surface center point. As a drop of the sound pressure level to -6 dB occurs twice, the angle of aperture is calculated as sum of the absolute values these two angles on both sides of the maximum.

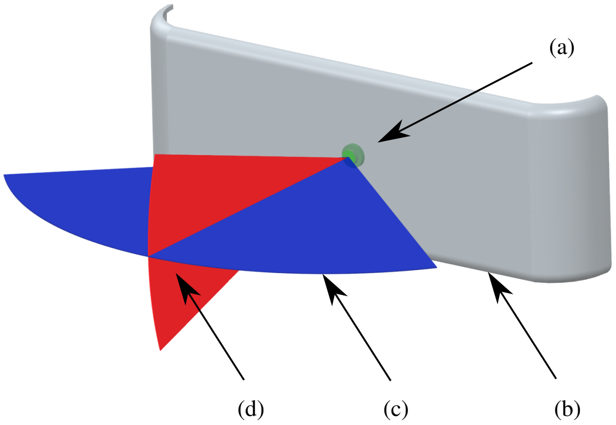

Figure 5: Ultrasonic transducer (a) in final application in a car bumper (b). Narrow angle of aperture in vertical direction (c) and wide angle of aperture in horizontal direction (d).

As an indicator for the anisotropy of the directivity pattern, an anisotropy factor α is defined by

$$
\alpha = \frac{\phi_{\mathrm{H},-6\ \mathrm{dB}}}{\phi_{\mathrm{V},-6\ \mathrm{dB}}}\,, \tag{34}
$$

where $\phi_{\mathrm{H},-6\ \mathrm{dB}}$ and $\phi_{\mathrm{V},-6\ \mathrm{dB}}$ indicate the angle of aperture in horizontal and vertical direction, cf. Fig. 5.

Experimental setup

The vibrational behavior of the ultrasonic transducer is characterized with a non-contact measurement using a scanning laser Doppler vibrometer. Thus, the resonance frequency and the operational deflection shape (ODS) are identified. Free-free boundary conditions are suitable to obtain reproducible results from experimental testing which are comparable to simulation results. To approximate this boundary condition, the sensor head is placed on two horizontally tighten yarns, cf. Fig. 6. The ultrasonic transducer is characterized in sound radiation mode. Consequently, the excitation is realized with an electrical voltage applied to the piezoelectric ceramic. A noise similar, periodic signal, so called pseudo random, is applied in the range from 40 kHz to 60 kHz. The advantage of this signal type is the absence of leakage [25]. All frequencies of the spectrum are excited simultaneously.

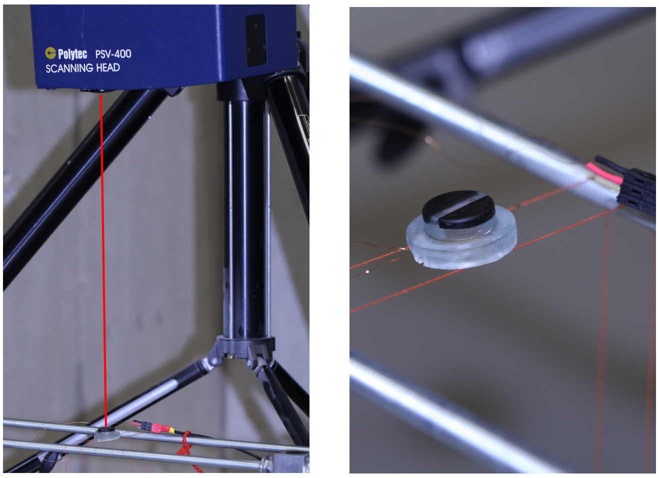

(a) (b)

Figure 6: Experimental test setup to characterize the surface velocity of the specimen. (a) Overview of measurement setup. (b) Specimen placed on horizontal tighten yarn to approximate free-free boundary conditions.

To obtain the eigenfrequencies and eigenvectors of the measured structure, an experimental modal analysis is performed. The agreement between simulation and experimental testing is determined using the modal assurance criterion (MAC). The MAC is a common method to quantify the comparison of mode shapes [26]. It is calculated by

$$
\mathrm{MAC} = \frac{\left| \sum_{\mathrm{j}=1}^{\mathrm{n}} \left(\varPhi_{\mathrm{Sim}}\right)_{\mathrm{j}} \left(\varPhi_{\mathrm{Exp}}\right)_{\mathrm{j}}^{*} \right|^{2}}{\left(\sum_{\mathrm{j}=1}^{\mathrm{n}} \left(\varPhi_{\mathrm{Sim}}\right)_{\mathrm{j}} \left(\varPhi_{\mathrm{Sim}}\right)_{\mathrm{j}}^{*} \right) \cdot \left(\sum_{\mathrm{j}=1}^{\mathrm{n}} \left(\varPhi_{\mathrm{Exp}}\right)_{\mathrm{j}} \left(\varPhi_{\mathrm{Exp}}\right)_{\mathrm{j}}^{*} \right)}\,, \tag{35}
$$

where $\varPhi_{\mathrm{Sim}}$ and $\varPhi_{\mathrm{Exp}}$ denote the elements of the eigenvectors $\underline{\varPhi}_{\mathrm{Sim}}$ and $\underline{\varPhi}_{\mathrm{Exp}}$ of simulation and experiment. The conjugate complex value is identified by *. The MAC is a scalar value $\mathrm{MAC} \in [0,1]$. Correlated modes should attain a MAC value greater than 0.9, while the MAC value for uncorrelated modes should be less than 0.05 [26].

Model description

In this section, the investigated test cases and the belonging models are presented. The models comprise the virtual models of the finite element simulation as well as the physical models of the experimental testing.

Test cases

The dynamical behavior is studied in a generic model representing the head of an ultrasonic transducer. It consists of three parts: the sensor head, a piezoelectric ceramic, and a circuit board, cf. Fig. 7. The sensor head contains sections of epoxy and sections of carbon fiber reinforced epoxy. The top surface of the plate-like structure, cf. Fig. 7 (a), is the sound radiating and receiving intersection in final applications. Even though, this plate-like structure is not a membrane within the meaning of a mechanical definition, it is often called membrane, cf [1, 27]. This is due to the similar usage of membranes in microphones and loudspeakers. Fig. 7 shows the reference model in cross-section.

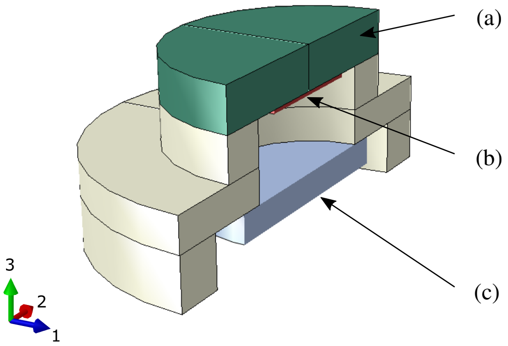

Figure 7: Reference model without locally structured fiber reinforcement in cross-section. (a) Fiber reinforced plate-like structure. (b) Piezoelectric ceramic. (c) Circuit board.

The sensor head does not contain local structuring of the fiber reinforcement. The fiber reinforcement is realized with a balanced, plain weave of carbon fiber in the plate-like structure. The electromechanical transformation is achieved by a piezoelectric ceramic. It is placed on the inside of the plate-like structure. Thus, sound can be radiated by applying an electrical voltage to the piezoelectric ceramic. This operating mode is called radiation mode or emission mode. In contrast, in receiving mode, the plate-like structure is excited by a sound pressure. Consequently, an electrical voltage results between the electrodes of the piezoelectric ceramic. The circuit board is jointed to the next level where the inner diameter increases. This has a stiffening effect on the sensor head.

To obtain an anisotropic directivity pattern, the carbon fiber reinforcement is locally structured as shown in Fig. 8. The first geometry of structuring contains two semicircular sections where no fiber reinforcement is present, cf. Fig. 8 (a) and (b). Model (a) is reinforced with a balanced, woven fabric of carbon fiber. Warp and weft yarn of the woven fabric are orientated in direction 1 and direction 2. A unidirectional, non-crimp fabric is used to reinforce model (b). The fibers are orientated parallel to direction 2. The second geometry of locally structured fiber reinforcements is realized by a stripe shaped section of epoxy in the center of the plate-like structure. The fiber reinforcement of model (c) is done similar to model (a). In case of model (d), the fiber orientation axis of the unidirectional, non-crimp fabric is parallel to the stripe of epoxy, coinciding with direction 1. The contour of the structured models are equal to the reference model. The thickness of the plate-like structure is 2.5 mm. In cases of model (a) and (b), the radius of the semicircular epoxy section is 6.0 mm. Regarding model (c) and (d), the width of the epoxy stripe is set to 4.0 mm.

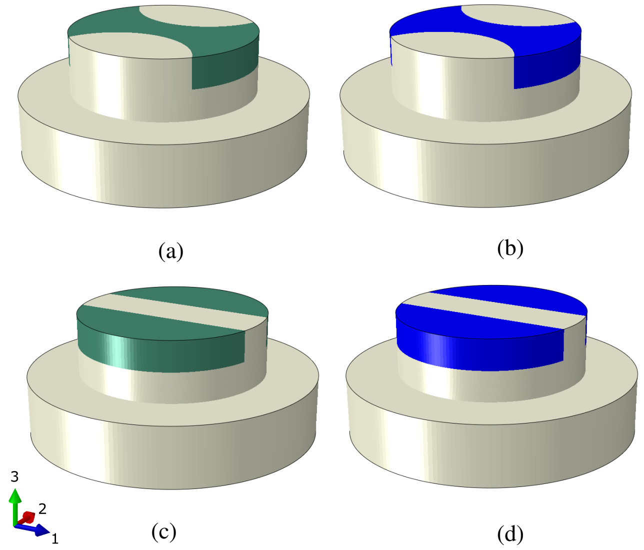

Figure 8: Models with locally structured fiber reinforcement in order to achieve an anisotropic directivity pattern. (a) Balanced, woven fabric with semicircular structuring at the outer area. (b) Unidirectional, non-crimp fabric with semicircular structuring at the outer area. Axis of fiber orientation in direction 2. (c) Balanced, woven fabric with section of epoxy only in the middle. (d) Unidirectional, non-crimp fabric with section of epoxy only in the middle. Axis of fiber orientation in direction 1.

Finite element model

The dynamical behavior is investigated in simulation with a finite element model. These simulations are carried out with the commercial software Simulia Abaqus 2017. The sensor is modeled with 20-node brick elements. To avoid mesh dependencies in the results, the guidelines given in [28] are considered. A maximum element edge length of 0.5 mm is applied. The piezoelectric ceramic is modeled with 20-node brick elements with piezoelectric properties. The contacts between sensor head and piezoelectric ceramic, and sensor and circuit board are realized by tie constraints with a surface to surface formulation. Thus, an idle joint is assumed.

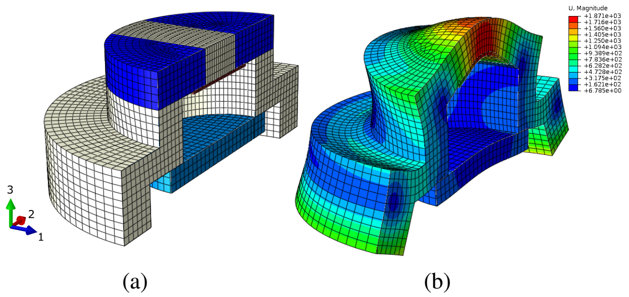

Figure 9: Finite element model of ultrasonic transducer head. (a) The mesh is realized with 20-node brick elements. (b) Mode shape of interest.

Free-free mechanical boundary conditions are applied to the model. In order to obtain the eigenfrequencies and the belonging mode shapes, a modal analysis is performed initially. In this case, a short circuit is applied to the piezoelectric ceramic. Especially, the mode with a mode shape where the plate-like structure is bended, cf. Fig. 9 (b), is focused. Afterwards, a harmonic analysis is carried out. In this case, an excitation is realized by applying an altering voltage of 100 V to the electrodes of the piezoelectric ceramic. Due to the different designs, the eigenfrequency and resonance frequency vary between the different test cases shown in Fig. 7 and Fig. 8. The corresponding eigenfrequencies and resonance frequencies are shown in table 2. In a post processing step, the directivity pattern is calculated at the resonance frequency out of the results gained from the harmonic analysis. The Rayleigh integral is performed on the surface at the top of the plate-like structure.

Table 2: Eigenfrequencies and resonance frequencies of the different models, cf. Fig. 7 and Fig. 8.

	Eigenfrequency [kHz]	Resonance frequency [kHz]
Reference model	45.6	45.3
Model a	43.8	43.7
Model b	42.5	42.4
Model c	42.9	42.8
Model d	43.2	43.1

Physical models

Physical models are required to validate the results from the finite element simulation. Furthermore, the feasibility of the proposed solutions can be proved. The specimens of the generic sensor head are prepared with a resin transfer molding process. The fiber reinforcement is cut and then placed in a molding tool. Cutting and handling requires high effort, as the fabric is small. Thus, it tends to break easily, particularly if the cutting and handling is done manually instead of fully automated. After placing the fiber reinforcement, the tool is closed and resin is injected. As soon as the resin is cured, the fiber reinforced composite can be demolded. In a following process, the piezoelectric ceramic is jointed with epoxy into the sensor head. The electrical contacts are realized by soldering wires on the piezo. In a final step, the circuit board is jointed to the sensor head.

Results

In this section, results from finite element simulation and experimental testing are presented and discussed.

Directivity pattern

The directivity pattern is calculated by performing the Rayleigh integral as described in the previous section. The reference model is set up with a non structured fiber reinforcement as mentioned above, cf. Fig. 7. Thus, the material properties in the plate-like structure are equal in the whole area.

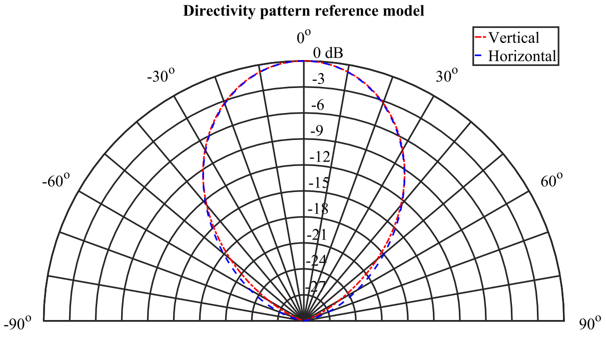

Figure 10: Polar plot of the directivity pattern of the reference model, cf. Fig. 7, at resonance frequency 45.3 kHz.

Fig. 10 shows the directivity pattern of the reference model in a polar plot. The angle of aperture is equal in vertical and horizontal direction. The reduction of the sound pressure level to -6 dB arises at 55° in both directions. Thus, the anisotropy factor α of the reference is unity as expected.

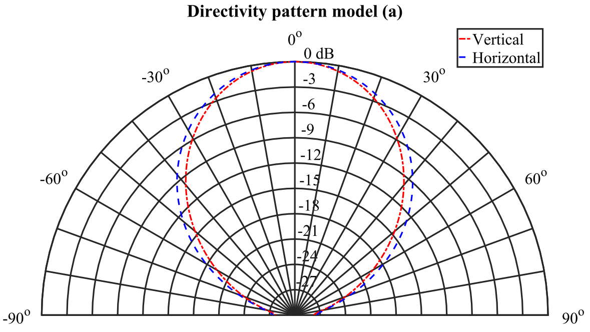

Figure 11: Polar plot of the directivity pattern of the structure model a, cf. Fig. 8 (a), at resonance frequency 43.7 kHz.

Structuring the fiber reinforcement of the reference model with two semicircular sections, cf. Fig. 8 (a), the directivity pattern shows a slight anisotropy, cf. Fig. 11. The anisotropy factor results in $\alpha = 1.10$. The angles of aperture increase to 68° in horizontal direction and 62° in vertical direction.

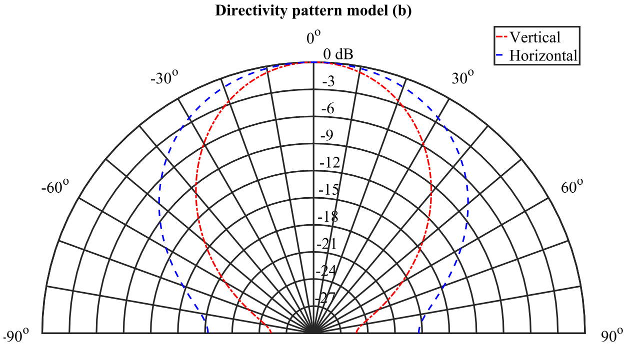

Figure 12: Polar plot of the directivity pattern of the structure model b, cf. Fig. 8 (b), at resonance frequency 42.4 kHz.

Replacing the balanced, woven fabric with a unidirectional, non-crimp fabric, cf. Fig. 8 (b), the gained anisotropy of the directivity pattern is much higher while keeping the same geometry of the fiber reinforcement, cf. Fig. 12. This is caused due to the higher anisotropy of the unidirectional, non-crimp fabric itself. The horizontal angle of aperture increases to 90°, while the vertical angle remains at 62°. Consequently, the anisotropy factor raises to $\alpha = 1.45$.

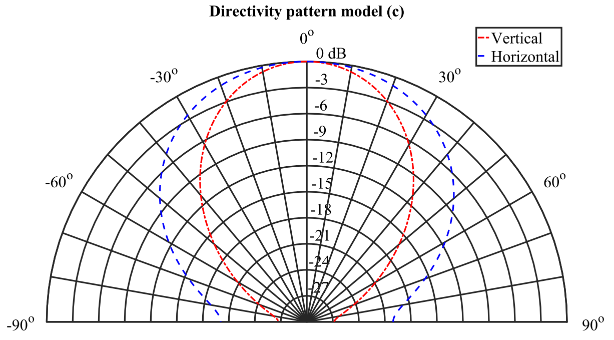

Figure 13: Polar plot of the directivity pattern of the structure model c, cf. Fig. 8 (c), at resonance frequency 42.8 kHz.

Dividing the fiber reinforcement in two separate parts and inserting a stripe of epoxy only, cf. Fig. 8 (c), results in a highly anisotropic directivity pattern, even using a balanced, woven fabric. Compared to the results in Fig. 12, the angles of aperture are narrower, with 89° in horizontal and 58° in vertical direction. The anisotropy factor results in $\alpha = 1.53$, cf. Fig. 13.

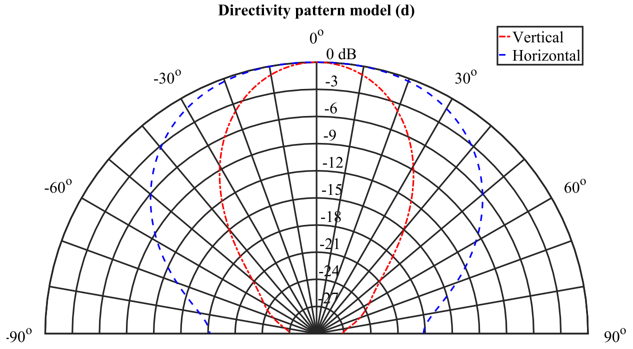

Figure 14: Polar plot of the directivity pattern of the structure model d, cf. Fig. 8 (d), at resonance frequency 43.1 kHz

Using the same geometrical design as in the previous model and inserting a unidirectional, non-crimp fabric, cf. Fig. 8 (d), increases the anisotropy of the directivity pattern again. The horizontal angle of aperture, 100°, is almost twice the vertical one, 51°, cf. Fig. 14 . Comparing Fig. 10 with Figs. 11 and 13, it is apparent, that an anisotropic directivity pattern can be achieved by local structuring of the fiber reinforcement. Replacing the balanced, woven fabric with a unidirectional, non-crimp fabric, results in a higher anisotropy of the directivity pattern, as shown in Figs. 12 and 14. Locally structured fiber reinforcements are identified as a suitable solution to realize ultrasonic transducers which have a wide angular aperture in horizontal plane and a narrow one in vertical plane.

Sensitivity and uncertainties

The aim of a sensitivity analysis is to identify the influence of various parameters on a certain output. The output can vary depending on the objective which is investigated. In this study, the objectives are the eigenfrequency of the ultrasonic transducer and the anisotropy factor α of the directivity patterns. Thus, the robustness of the design with regard to uncertain parameters is considered. As the models c and d show higher anisotropy factors, the sensitivity analysis is focused on these designs. In case of the reference model, the investigated geometrical uncertain parameter is the thickness of the plate-like structure. In cases of models with locally structured fiber reinforcement, additional geometrical uncertainties of the fiber layers are investigated. Thus, the sensitivity to changes in the width of the epoxy stripe and the angle of fiber orientation are studied. Furthermore, the influence of the angle of fiber orientation is investigated with different fiber volume fractions. To quantify the influence of material properties, the Young's modulus of the carbon fiber parallel to its fiber axis $E_{\mathrm{F},\parallel}$, cf. Eq. (6), is varied. Default parameters for the finite element model are set in accordance to the values presented in table 1 and in section "Test cases".

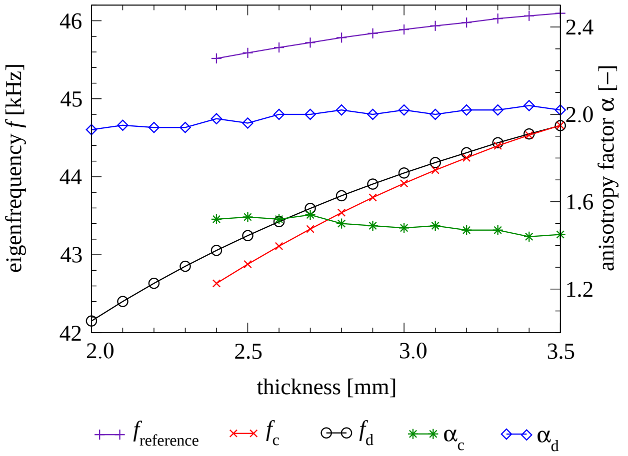

Figure 15: Sensitivity to changes in thickness of the plate-like structure. Eigenfrequency of the reference model ($f_{\mathrm{reference}}$), eigenfrequency of model c (f_{c}), eigenfrequency of model d (f_{d}), anisotropy factor of model c (α_{c}), anisotropy factor of model d (α_{d}), cf. Fig. 8.

Firstly, the sensitivity to changes of the thickness of the plate-like structure is investigated. Therefore, the number of layers of the fiber reinforcement is held constant. In cases of a balanced, woven fabric, 8 layers are assumed. The thickness varies within a range from 2.4 mm to 3.5 mm. For unidirectional, non-crimp fabrics, 4 layers are applied in the model. Thus, the thickness is changed in the range from 2.0 mm to 3.5 mm. Taking Eq. (26) into account, it is obvious that the fiber volume fraction changes for different thicknesses of the structure. Fig. 15 shows the results obtained from finite element simulation. The sensitivity of the eigenfrequency to changes in the thickness of the plate-like structure increases by applying a locally structured fiber reinforcement compared to the reference model. A balanced, woven fabric shows a higher sensitivity in comparison with a unidirectional, non-crimp fabric. The influence on the anisotropy factor α is only small. It decreases in case of rising thickness for model (b), cf. Fig. 8, while using a unidirectional, non-crimp fabric leads to the opposite behavior. Referenced to 2.5 mm thickness, the increase to 3.5 mm changes the anisotropy factor less than -6 % in case of a balanced, woven fabric reinforcement and less than 5 % in case of a unidirectional, non-crimp fabric reinforcement.

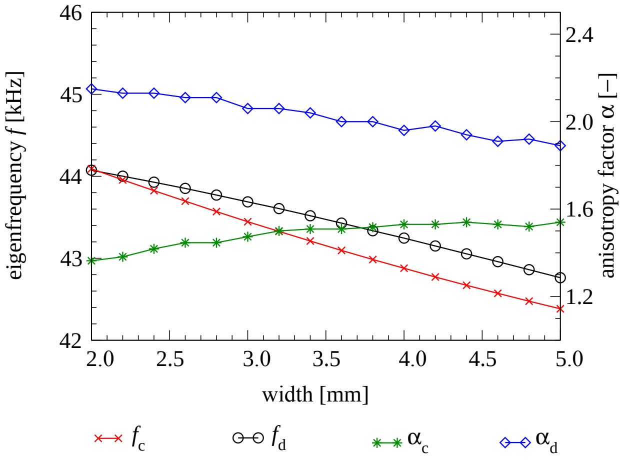

Figure 16: Sensitivity to width of the epoxy stripe. Eigenfrequency of model c (f_c), eigenfrequency of model d (f_d), anisotropy factor of model c (α_c), anisotropy factor of model d (α_d), cf. Fig. 8.

A geometrical parameter present only in composites with locally structured fiber reinforcement is the width of stripe made of epoxy. Fig. 16 shows the results from the sensitivity analysis investigating the influence of the width. In general, a wider stripe of epoxy results in a lower eigenfrequency. This is due to a lower overall stiffness of the plate-like structure. As for changes in thickness, the sensitivity of balanced, woven fabric reinforcement is higher than of structures with reinforcements of unidirectional, non-crimp fabric. In the first case, widen up the stripe of epoxy has only small influence on the anisotropy factor α. Increasing the width from 4.0 mm to 5.0 mm, the anisotropy factor rises less than 1 %. The fiber reinforcement with unidirectional, non-crimp fabric shows the opposite behavior. Increasing the width of the epoxy stripe from 4.0 mm to 5.0 mm, the anisotropy factor decreases by approximately 4 %.

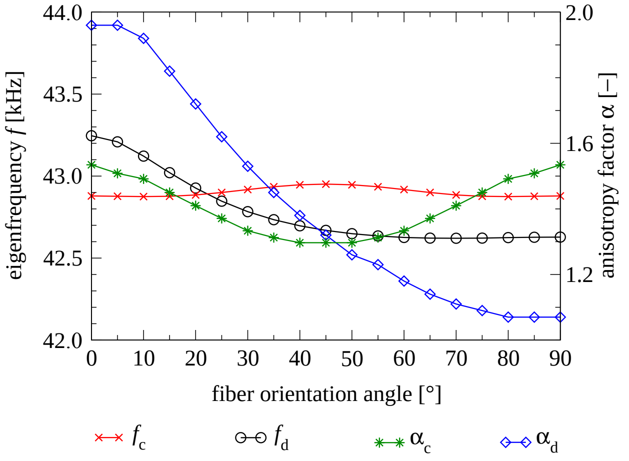

Figure 17: Influence of the angle of fiber orientation. Eigenfrequency of model c (f_c), eigenfrequency of model d (f_d), anisotropy factor of model c (α_c), anisotropy factor of model d (α_d), cf. Fig. 8.

Due to the orthotropic material behavior, the angle of fiber orientation has significant influence on the dynamical behavior of the ultrasonic transducer. As the woven fabric is balanced, the fiber reinforcement is equal in direction 1 and 2, cf. section "Balanced, woven fabric". Thus, the material behavior shows axial symmetry in the range from 0° to 90° with axis of symmetry at 45° fiber orientation angle. For unidirectional reinforcement, there is no axis symmetry observed in this range. Fig. 17 shows the eigenfrequency and the anisotropy factor α depending on the angle of fiber orientation. At 0° fiber orientation angle, the axis of the unidirectional fiber reinforcement is parallel to the orientation of the epoxy stripe. Similar to that definition, the warp yarn in a woven fabric is parallel to the stripe shaped epoxy section. The influence on the eigenfrequency of the balanced, woven fabric reinforced structure is quite small. Changing the angle of fiber orientation from 0° to 45°, the eigenfrequency increases by only 72 Hz which is less than 0.2 %. The influence on the anisotropy factor α is much higher. In the same range, it decreases by 15 % from 1.53 to 1.30. The sensitivity of the unidirectional, non-crimp fabric is even higher. Nevertheless, the drop in eigenfrequency is only small. It decreases from 43.3 kHz at 0° to 42.6 kHz at 90° which is less than 2 %. Meanwhile, the anisotropy is highly sensitive to the angle of fiber orientation. It decreases by more than 45 % from 1.96 to 1.07.

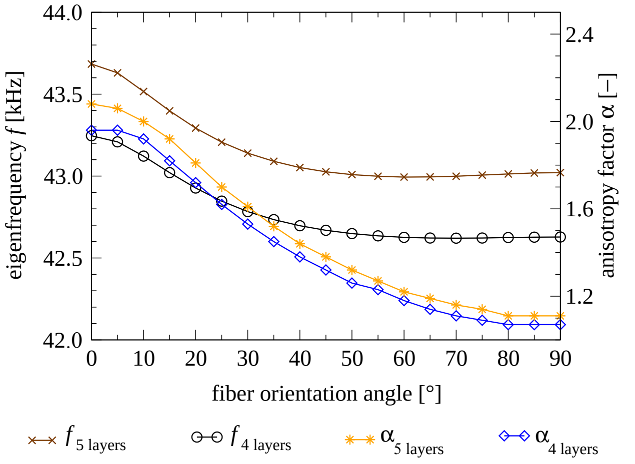

Figure 18: Influence of the angle of fiber orientation at different fiber volume fractions. Eigenfrequency of model d with 5 layers of fabric ($f_{5\ \text{layers}}$), eigenfrequency of model d with 4 layers of fabric ($f_{4\ \text{layers}}$), anisotropy factor of model d with 5 layers of fabric ($\alpha_{5\ \text{layers}}$), anisotropy factor of model d with 4 layers of fabric ($\alpha_{4\ \text{layers}}$), cf. Fig. 8.

The sensitivity analysis on the fiber orientation angle is performed once again with a unidirectional, non-crimp fabric. This time, an additional layer of fabric is inserted. Thus, the fiber volume fraction increases from 35 % to 44 %. Due to the increased fiber volume fraction, the Young's modulus in direction, parallel to the fiber axis,cf. Eq. (6) and the longitudinal-transverse shear modulus, cf. Eq. (10) increase by approximately 24 %. The Young's modulus perpendicular to the fiber axis, cf. Eq. (7) and the transverse-transverse shear modulus, cf. Eq. (13) increase by approximately 16 %. The density of the composite material increases by only 4 %. Thus, the eigenfrequency of the plate-like structure rises. The anisotropy of the directivity pattern increases as well. In general, the relation between eigenfrequency and anisotropy factor, and fiber orientation angle remains similar for different fiber volume fractions.

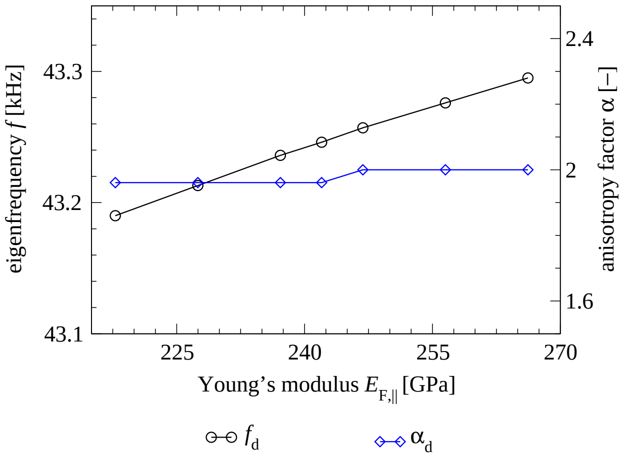

Figure 19: Sensitivity to changes of Young's modulus of the fiber reinforcement. Young's modulus parallel to fiber axis $E_{\mathrm{F},\|}$ is varied by ±10 % of the nominal value. Eigenfrequency of model d (f_d), anisotropy factor of model d (α_d), cf. Fig. 8.

Finally, the sensitivity to uncertainties in the Young's modulus of the fiber reinforcement is investigated. Therefore, the Young's modulus $E_{F,\|}$ parallel to the axis of the fiber is varied in a range of ±10 % of the nominal value, given in table 1. As seen in Fig. 19, the sensitivity to changes of Young's moduli is very small as the difference in eigenfrequency is less than ± 0.2 %. The influence on the anisotropic factor α is negligible.

Concluding the sensitivity analysis, it reveals that the thickness of the plate-like structure and the width of the epoxy stripe have the highest influence on the eigenfrequency, while the influence on the anisotropy factor of the directivity pattern is rather small. High sensitivity of the directivity pattern is identified for the angle of fiber orientation both for balanced, woven fabric and unidirectional, non-crimp fabric. Especially, the anisotropy factor of a fiber reinforcement with unidirectional, non-crimp fabric is highly sensitive to changes in the angle of fiber orientation.

Experimental testing

The results from finite element simulation are validated by experimental testing. Therefore, the physical model according to model setup (d), cf. Fig.8 is characterized. Performing an experimental modal analysis, the eigenfrequencies are obtained. The eigenfrequency of interest is retrieved at 45.6 kHz. The finite element simulation shows the eigenfrequency at 43.2 kHz. Thus, the difference between simulation and experiment is less than 5 %. The agreement between simulation and experimental testing is determined using the MAC, cf. Eq. (35). As the radiated sound pressure is characterized by the surface velocity of the plate-like structure, the mode shapes of this intersection are compared. Fig. 20 shows the component in direction 3 of the mode shapes in finite element simulation and in the experiment. The determined MAC is 0.93. Hence, a good agreement between finite element simulation and experiment is achieved.

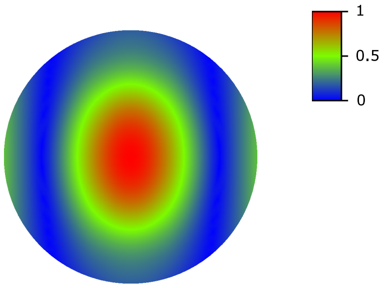

Simulation: Eigenfrequency 43.2 kHz

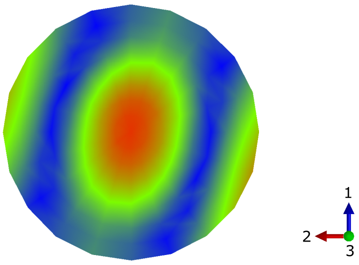

Experiment: Eigenfrequency 45.6 kHz

Figure 20: Mode shapes of finite element simulation and experiment of model d, cf. Fig. 8 (d). Displacement normalized component in direction 3 is shown.

To get an additional comparability between finite element simulation and experimental testing, the velocity distribution in the operational deflection shape is compared along the horizontal and vertical axis of the ultrasonic transducer. As in experimental results the orientation of the resulting ellipse, cf. Fig. 20 is rotated, the orientation of the horizontal and vertical axis is rotated also. Thus, they coincide with the major and minor axis of the ellipse. In Fig. 21, the magnitude of the complex velocity, normalized to its maximum, is plotted versus the normalized diameter of the sound radiating plate-like structure of the ultrasonic transducer. The results show good accordance between finite element simulation and experiment both in horizontal and vertical direction.

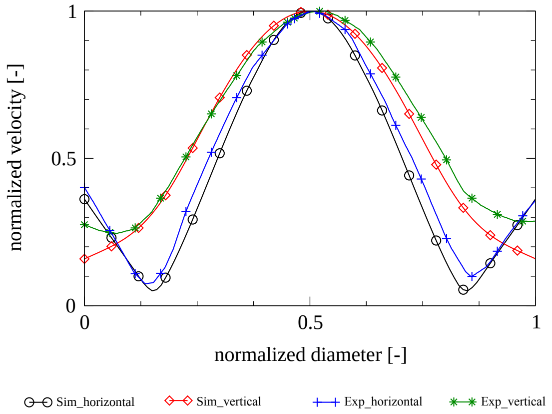

Figure 21: Surface velocity distribution along vertical and horizontal axis of the ultrasonic transducer. Comparison between finite element simulation and experimental testing.

Conclusion

The authors present a new approach to realize ultrasonic transducers with an anisotropic directivity pattern based on locally structured, fiber reinforced composites. In a generic model, representing the sensor head, the dynamical behavior is investigated. In finite element simulation, a homogenization approach is applied to predict the material properties of the composite using the material properties of the single components. The dynamical behavior is studied in a modal analysis and a harmonic analysis. Based on the results of the harmonic analysis, the directivity pattern is calculated applying the Rayleigh integral. It is shown that locally structured fiber reinforcements offer a suitable solution to realize ultrasonic transducers with anisotropic directivity pattern. Depending on the local structuring and the type of fabric, the anisotropy varies strongly. In general, both balanced, woven fabric and unidirectional, non-crimp fabric are suitable to accomplish different sound radiation properties in horizontal and vertical direction. In a sensitivity analysis, the influence of geometrical and material uncertainties is investigated with regard to changes in eigenfrequency and anisotropy of the directivity pattern. As major influences on the eigenfrequency, the thickness of the plate-like structure and the width of the epoxy stripe are identified. The anisotropy of the directivity pattern is mainly influenced by the angle of fiber orientation. In experimental testing, the results from finite element simulation are validated by calculating the MAC and comparing the surface velocity of the sound radiating surface. The results show good accordance between finite element simulation and experiment. The authors conclude that locally structured fiber reinforcements are suitable to realize an ultrasonic transducer with anisotropic directivity pattern.

References

[1] Rapps, P., Knoll, P., Pachner, F., Noll, M. and Fischer, M. “Ultrasonic transducer”. United States Patent 5,446,332, 1995

[2] Cheng, C.-C., Lin, C.-Y., Wu, W.-J., Wu, K.-C. and Lee, C.-K. “Highly anisotropic beam patterns for a pot-like ultrasonic sensor with penetrating slots configuration”. In “2009 IEEE International Ultrasonics Symposium”, pages 775–778. 2009. doi:10.1109/ULTSYM.2009.5441488

[3] Ho, J. H., Cheng, C. C., Tsou, N. T., Chen, C. S., Shieh, J., Lee, C. K. and Wu, W. J. “Ultrasonic transmitters far field beam pattern altering with boundary conditions design”. In “2007 Sixteenth IEEE International Symposium on the Applications of Ferroelectrics”, pages 738–741. 2007. doi:10.1109/ISAF.2007.4393387

[4] Hiyama, M., Emura, T. and Kumagai, M. “Sharpening directivity of ultrasonic range sensor using multiple transmitters by different amplitude and pulse width method”. In “Proceedings Fourth Annual Conference on Mechatronics and Machine Vision in Practice”, pages 73–78. 1997. doi:10.1109/MMVIP.1997.625288

[5] Nishioka, T., Teshima, Y., Mano, T., Sakai, K., Asada, T., Matsukawa, M., Ohta, T. and Hiryu, S. “Ultrasound radiation from a three-layer thermoacoustic transformation device”. Ultrasonics, 57:84 – 89, 2015. doi:10.1016/j.ultras.2014.10.019

[6] Kocbach, J. M. Finite element modelling of ultrasonic piezoelectric transducers. Influence of geometry and material parameters on vibration response functions and radiated field. Ph.D. thesis, University of Bergen; Department of Physics, 2000

[7] Jiang, C., Chang, Y. and Kam, T. “Optimal design of rectangular composite flat-panel sound radiators considering excitation location”. Composite Structures, 108(Supplement C):65 – 76, 2014. doi:https://doi.org/10.1016/j.compstruct.2013.09.005

[8] Niu, B., Olhoff, N., Lund, E. and Cheng, G. “Discrete material optimization of vibrating laminated composite plates for minimum sound radiation”. International Journal of Solids and Structures, 47(16):2097 – 2114, 2010. doi: http://dx.doi.org/10.1016/j.ijsolstr.2010.04.008

[9] Täger, O., Dannemann, M. and Hufenbach, W. A. “Analytical study of the structural-dynamics and sound radiation of anisotropic multilayered fibre-reinforced composites”. Journal of Sound and Vibration, 342:57 – 74, 2015. doi: https://doi.org/10.1016/j.jsv.2014.12.040

[10] Schürmann, H. Konstruieren mit Faser-Kunststoff-Verbunden. Springer Berlin Heidelberg, 2007

[11] Dassault Systemes. Abaqus 6.14 Online Documentation - Abaqus Analysis User’s Guide, 2014

[12] Foye, R. “The transverse poisson’s ratio of composites”. Journal of Composite Materials, 6(2):293–295, 1972. doi: 10.1177/002199837200600209

[13] Summerscales, J. “The bulk modulus of carbon fibers”. Journal of Materials Science Letters, 19(1):15–16, 2000. doi:10.1023/A:1006731210592

[14] Cherif, C. Textile Werkstoffe für den Leichtbau: Techniken - Verfahren - Materialien - Eigenschaften. SpringerLink : Bücher. Springer Berlin Heidelberg, 2011

[15] Akkerman, R. “Laminate mechanics for balanced woven fabrics”. Composites Part B: Engineering, 37(2):108 – 116, 2005. doi:http://dx.doi.org/10.1016/j.compositesb.2005.08.004

[16] Köllner, S. Modellbildung und Simulation von Ultraschallwandlern auf Basis von Verbundwerkstoffen (Modelling and simulation of ultrasonic transducers based on composites). Master’s thesis, Karlsruhe Institute of Technology, Department of Mechanical Engineering, 2014

[17] Halpin, J. “Stiffness and expansion estimates for oriented short fiber composites”. Journal of Composite Materials, 3(4):732–734, 1969. doi:10.1177/002199836900300419

[18] Deutsches Institut für Normung e. V. “DIN EN 12127: Textiles - Fabrics - Determination of mass per unit area using small samples”, 1997

[19] Baron Rayleigh Strutt, J. W. The Theory Of Sound Vol.2. Dover Publications, 1896

[20] Koopmann, G. H. and Fahnline, J. B. Designing Quiet Structures : A Sound Power Minimization Approach. Elsevier Science, 1997

[21] Fritze, D., Marburg, S. and Hardtke, H.-J. “Estimation of radiated sound power: A case study on common approximation methods”. Acta Acustica united with Acustica, 95(5):833–842, 2009. doi:10.3813/AAA.918214

[22] Möser, M. Technische Akustik (Technical acoustics). Springer-Verlag, Berlin Heidelberg New York, 10. aufl. edition, 2015

[23] Marburg, S. "Developments in structural-acoustic optimization for passive noise control". Archives of Computational Methods in Engineering, 9(4):291–370, 2002. doi:10.1007/BF03041465

[24] Hübner, G. and Gerlach, A. "Zusammenhang der DFEM-Schalleistungsbeschreibung mit der Rayleighschen Schallfelddarstellung ebener Strahler". In "Fortschritte der Akustik / DAGA", 1998

[25] Polytec GmbH, Polytec-Platz 1-7, 76337 Waldbronn, Germany. Theory Manual Polytec Scanning Vibrometer PSV Theory, As of Software 9.1 edition

[26] Ewins, D. Modal testing: theory and practice. Mechanical engineering research studies. Research Studies Press, 1984

[27] Winner, H., Hakuli, S. and Wolf, G. Handbuch Fahrerassistenzsysteme: Grundlagen, Komponenten und Systeme für aktive Sicherheit und Komfort. ATZ/MTZ-Fachbuch. Vieweg+Teubner Verlag, 2012

[28] Langer, P., Maeder, M., Guist, C., Krause, M. and Marburg, S. "More than six elements per wavelength: The practical use of structural finite element models and their accuracy in comparison with experimental results". Journal of Computational Acoustics, 25(4):1750025, 2017. doi: 10.1142/S0218396X17500254

Contact Information

Corresponding author: Johannes Henneberg
Email address: Johannes.Henneberg@de.bosch.com

Acknowledgments

The authors gratefully acknowledge Robert Bosch GmbH Germany for the funding of this research.

Paper B

Journal of Sound and Vibration 452 (2019) 132–146

Contents lists available at ScienceDirect

Journal of Sound and Vibration

journal homepage: www.elsevier.com/locate/jsvi

The potential of stop band material in multi-frequency ultrasonic transducers

J. Henneberg [a,c,*], A. Gerlach [a], H. Cebulla [b], S. Marburg [c]

[a] Robert Bosch GmbH, Robert-Bosch-Campus 1, 71272 Renningen, Germany
[b] Technical University Chemnitz, Reichenhainer Str. 31/33, 09126 Chemnitz, Germany
[c] Technical University of Munich, Boltzmann Str. 15, 85748 Garching, Germany

ARTICLE INFO

Article history:
Received 2 August 2018
Revised 6 February 2019
Accepted 31 March 2019
Available online 4 April 2019
Handling Editor: O Gottlieb

Keywords:
Multi-frequency transducer
Stop band material
Acoustic metamaterial
Band gap behavior

ABSTRACT

Ultrasonic transducers play a major role in surround sensing for automotive and industrial applications. The development of autonomous driving functions is one of the top challenges for mobility solutions of the 21st century. In this context, surround sensing systems with high performance serve as a key enabler. This leads to an increasing number of sensors which are desired to operate in parallel or in shorter intervals. Hence, measurements should be conducted with two different frequencies to discriminate the sensor signals. Known multi-frequency ultrasonic transducers mostly employ multiple electro-mechanical coupling elements which require more complex sensor electronics.

To overcome this issue, the authors present a study on multi-frequency ultrasonic transducers using only one electro-mechanical coupling element. In order to achieve suitable sound radiation properties at two well separated operating frequencies, spatially distributed stop band material is employed. As a result, the operational deflection shape can be controlled at a certain frequency. In finite element simulation, the relation between spatially distributed stop band material and the resulting operational deflection shapes is investigated. The sound radiation behavior is estimated using the numerical results from a harmonic analysis as input for the Rayleigh integral. In experimental investigations, the presented approach is validated. Finite element simulation and experimental testing show good accordance. Based on the results of the presented study, it is possible to realize a multi-frequency ultrasonic sensor with one electro-mechanical transducer element only and suitable sound radiation behavior at multiple operating frequencies.

© 2019 The Authors. Published by Elsevier Ltd. This is an open access article under the CC BY license (http://creativecommons.org/licenses/by/4.0/).

1. Introduction

In recent years, the development of automatic and autonomous driving function gained rising attention. This requires a more detailed and reliable surround sensing of the environment than for manual driving. Since decades, ultrasonic sensors are widely used in surround sensing applications in automotive and industrial sectors. The distance between the sensor and the object is detected by pulse-echo operation [1]. In order to get a comprehensive resolution of the environment, the number of applied ultrasonic sensors increases continuously. To operate the sensors in shorter intervals or in parallel, it is desired to use multiple operating frequencies. Thus, a signal discrimination is possible by frequency filtering.

---

[*] Corresponding author. Robert Bosch GmbH, Robert-Bosch-Campus 1, 71272 Renningen, Germany.

E-mail addresses: Johannes.Henneberg@de.bosch.com, johannes.henneberg@tum.de (J. Henneberg).

https://doi.org/10.1016/j.jsv.2019.03.026

0022-460X/© 2019 The Authors. Published by Elsevier Ltd. This is an open access article under the CC BY license (http://creativecommons.org/licenses/by/4.0/).

In literature, a couple of approaches to realize ultrasonic sensors with multiple operating frequencies are presented. In 1948, a stepped-frequency transducer consisting of multiple magnetostrictive nickel elements is presented by Ref. [2]. The single elements are loosely coupled to form a stack. Via a common electrical winding, the simultaneous excitation of the elements is possible. The aim of that study is to attain transducers with a broader frequency response. However, depending on the damping of the system, the approach would offer also a possibility to form multi-frequency transducers. It is found that the stepped-frequency transducers with multiple elements suffer from a lack of efficiency compared to single-frequency equivalents. In Ref. [3], a split-mode ultrasonic transducer is investigated. A structure with a two-dimensional periodicity of poled domains is created in a ferroelectric wafer with free surfaces. As a result, an ultrasonic transducer with multiple acousto-electric resonances is obtained. A piezoelectric micromachined ultrasonic transducer (PMUT) with multiple electrodes is presented in Ref. [4]. Due to multiple electrodes, the device provides high sensitivity at multiple frequencies coinciding with the first, third and fifth fundamental frequency of the transducer. Capacitive micromachined ultrasonic transducers (CMUT) are employed in Ref. [5]. A CMUT array with acoustic elements of different dimensions is designed having multiple operating frequencies. An approach using only one electro-mechanical coupling element is presented in Ref. [6]. The transmission of ultrasound is possible at multiple frequencies in the range of several MHz by adding an appropriate front layer. It is used for interstitial ultrasound thermal therapy. In the same context of medical ultrasonic therapy, a dual-frequency lead zirconate titanate (PZT)-transducer array with fundamental frequency (4.1 MHz) and third harmonic (13.3 MHz) is characterized in Ref. [7]. Ref. [8] presents a hybrid multi-frequency ultrasonic transducer. It consists of different electro-mechanical coupling elements. One of which is a piezoelectric ceramic while the other one is made of PVDF. By hybridization of both characteristic properties, the transducers enable the usage of multiple resonance frequencies. In Ref. [9], also two electro-mechanical coupling mechanisms are combined. Thus, a CMUT as well as a PMUT electro-mechanical coupling is realized in one element. The transducer can be operated at two operating frequencies. Suitable sound radiation properties for surround sensing can be expected with the obtained mode shapes at both frequencies.

However, all presented approaches suffer at least from one of the following lacks:

- The approach is not suitable for surround sensing applications. Especially the sound radiation behavior is not appropriate at various operating frequencies. It should show directivity pattern without distinctive side lobes. Hence, they are similar to monopole or dipole behavior at all operating frequencies.
- Multiple electro-mechanical coupling elements are used to realize multi-frequency transducers. This leads to more complex electronics required for surround sensing and is mostly undesired.

To overcome these issues, the present study investigates a novel approach employing spatially distributed stop band material in order to obtain a multi-frequency transducer with only one electro-mechanical coupling element and suitable sound radiation properties at two distinctive operating frequencies. Stop band materials attract attention within vibroacoustics recently [10]. Basically, it is possible to attain structures which do not allow free wave propagation in certain frequency ranges. These frequency ranges are called stop bands or band gaps [11,12]. In 2000, a phononic crystal with particular high sound transmission loss at certain frequencies is presented by Ref. [13]. The phononic crystal consists of rubber coated lead spheres which are embedded in epoxy. In Ref. [14], it is shown that stop bands caused by periodic, resonant structures show good prospect for low frequencies. Furthermore, the band gap behavior can be simply tuned by the periodic resonator. In Ref. [15], it is shown that stop bands can also be attained with randomly arranged resonant structures. However, the spacing between the resonators is required to be at a subscale of the wavelength corresponding to the desired band gap. Due to their ability to generate frequency ranges without wave propagation, stop band materials are predestined to increase sound transmission loss of structures. This is investigated in several studies, e.g. Refs. [16–22]. The possibility of waveguiding Lamb modes within a certain frequency is studied numerically and experimentally in Ref. [23]. In Ref. [24], the propagation of flexural waves in thin plates is investigated. It is shown that wave propagation can be attenuated by locally attached spring-mass resonators. The behavior of different excitations is investigated with regard to the vibration transmission. In Ref. [25], similar structures are investigated with regard to the sound transmission loss. In Ref. [26], the authors show the good prospect of stop band material in order to reduce mechanical cross-coupling in phased-array transducers.

In this study, stop band material is investigated with a rather different purpose. The operational deflection shape of a plate like structure representing a generic model of an ultrasonic transducer is modified within a certain frequency range. Therefore, sections with and without stop band behavior are spatially distributed. Stop band material shows the advantage that only a certain frequency range is effected by the particular dynamic behavior. Outside of the stop band, the influence on the dynamic behavior of the plate like structure is only small. Hence, certain operating frequencies can be tuned mainly independently from each other. This approach opens up the possibility to achieve a multi-frequency transducer having only one electro-mechanical coupling element and suitable sound radiating behavior at multiple operating frequencies. Thus, the drawback of known multi-frequency ultrasonic transducer concepts can be overcome.

This work is structured as follows: initially, we focus on the methods applied in this study. The generic model to investigate the dynamic behavior is presented in Section 3. The approach is investigated numerically with a finite element model as well as in experiments with a physical model. The results are presented in Section 4. In Section 5, the approach is transferred to the ultrasonic frequency range. Finally, a conclusion is drawn.

2. Methods

In this section, the employed methods are presented briefly. First, the Rayleigh integral is discussed in order to estimate the radiated sound pressure field generated by the plate vibration. Afterwards, the wave finite element method (WFEM) applying periodicity conditions is presented. With this approach, it is possible to characterize the wave propagation behavior in periodic structures. Finally, the experimental validation using laser Doppler vibrometer is described.

2.1. Sound radiation

The sound radiation behavior of sound transducers is usually characterized by the directivity pattern. This can be calculated in the far-field employing the Rayleigh integral [27,28]. It provides an exact solution under the following conditions:

- the radiating surface is flat,
- the radiator is embedded in a flat, infinite, and rigid baffle.

These assumptions are suitable in order to obtain a reasonable approximation of the directivity pattern for ultrasonic transducers embedded in a mounting structure like a car bumper. This is discussed in several studies like Refs. [29,30]. However, in Ref. [31] it is shown that the Rayleigh integral produces reasonable results even for more complex structures. The assumption of a baffled plate holds for the investigated structures and the ultrasonic transducers for surround sensing applications in automotive and robotic industries.

In order to fit the far-field assumption, three conditions must be fulfilled [32]. Firstly, the distance (R) between the radiator and the field point has to be much greater than the dimension (l) of the radiator

$$R \gg l \, . \tag{1}$$

Secondly, the condition

$$\frac{R}{l} \gg \frac{l}{\lambda} \tag{2}$$

must be fulfilled. Consequently, the error caused by phase shifts is small [33]. Finally, the wavelength (λ) should be small compared to the distance between the radiator and field point

$$\lambda \ll R \, . \tag{3}$$

For $e^{i\omega t}$ harmonic time dependence, the Rayleigh integral for a plane surface can be expressed by Ref. [34].

$$p(\vec{y}) = \int_{\Gamma} - i\omega\rho_{\mathrm{f}} G(\vec{x},\vec{y}) v_{\mathrm{f}}(\vec{x}) \, \mathrm{d}\Gamma(\vec{x}) \tag{4}$$

with

$$G(\vec{x},\vec{y}) = \frac{e^{-ikr}}{2\pi r} \text{ and } r = |\vec{x} - \vec{y}| \, , \tag{5}$$

where $\Gamma, k, \omega, v_{\mathrm{f}}, \rho_{\mathrm{f}}, i$ denote the radiating surface, wavenumber, circular frequency, fluid particle velocity, fluid density, and imaginary unit. The particle velocity distribution on the surface of the structure can be used to estimate the radiated far-field sound pressure as shown in Ref. [35]. In spherical coordinates (R, ϑ, φ), the Rayleigh integral can be approximated for the sound pressure in the far-field by Ref. [32].

$$p(R,\vartheta,\varphi) = \frac{i\omega\rho_{\mathrm{f}}}{2\pi R} e^{-ikR} \int_{-l_y\backslash 2}^{l_y\backslash 2} \int_{-l_x\backslash 2}^{l_x\backslash 2} e^{ik(x_{\mathrm{Q}} \sin\vartheta \cos\varphi + y_{\mathrm{Q}} \sin\vartheta \sin\varphi)} \, v(x_{\mathrm{Q}}, y_{\mathrm{Q}}) \, \mathrm{d}x_{\mathrm{Q}} \, \mathrm{d}y_{\mathrm{Q}} \, . \tag{6}$$

The transformation from Cartesian to spherical coordinates is realized by

$$\begin{aligned} x &= R\sin(\vartheta)\cos(\varphi), \\ y &= R\sin(\vartheta)\sin(\varphi), \\ z &= R\cos(\varphi). \end{aligned} \tag{7}$$

Analyzing the directivity pattern in polar plots, it is possible to identify the sound radiation behavior of the investigated generic model.

2.2. Dispersion in periodic infinite structures

The wave propagation behavior in a periodic structure can be characterized by the dispersion relations in a unit cell. The Floquet Bloch theorem offers a possibility to handle periodic structure and to determine the wave propagation properties [36]. A freely propagating wave can be described for $e^{i\omega t}$ harmonic time dependence with angular frequency ω by

$$\psi = We^{i(\omega t - k_x x - k_y y)}, \tag{8}$$

with W describing the wave mode through the thickness of the structure, ψ being a response variable, and k_x, k_y being the components of the wavenumber in $x-$ and $y-$direction, respectively. This can be obtained by employing finite element methods. The motion is described by a finite number of generalized displacements $\mathbf{q}$.

In case of two-dimensional periodicity in $x-$ and $y-$direction, $\mathbf{q} = \begin{bmatrix}\mathbf{q}_1 & \mathbf{q}_2 & \mathbf{q}_3 & \mathbf{q}_4\end{bmatrix}^{\mathrm{T}}$ contains the generalized displacements at nodes 1 to 4, cf. Fig. 1. The Bloch theorem states that the relation between the generalized displacements can be described by Ref. [37].

$$\begin{aligned} \mathbf{q}_2 &= \lambda_x \mathbf{q}_1, \\ \mathbf{q}_3 &= \lambda_y \mathbf{q}_1, \\ \mathbf{q}_4 &= \lambda_x \lambda_y \mathbf{q}_1, \end{aligned} \tag{9}$$

with

$$\begin{aligned} \lambda_x &= e^{-ik_x \cdot r_x} \quad \text{and} \quad \mu_x = k_x r_x, \\ \lambda_y &= e^{-ik_y \cdot r_y} \quad \text{and} \quad \mu_y = k_y r_y, \end{aligned} \tag{10}$$

where $r_{x,y}$ and $\mu_{x,y}$ represent the length of the periodic lattice and the propagation constant in the direction of periodicity, respectively. Introducing the reduction matrix by

$$\Lambda_{\mathrm{R}} = \begin{bmatrix}\mathbf{I} & \lambda_x \mathbf{I} & \lambda_y \mathbf{I} & \lambda_x \lambda_y \mathbf{I}\end{bmatrix}^{\mathrm{T}}, \tag{11}$$

the generalized displacement vector can be described dependent on $\mathbf{q}_1$ by

$$\mathbf{q} = \Lambda_{\mathrm{R}} \mathbf{q}_1. \tag{12}$$

In the absence of damping, the generalized displacements are related to the generalized forces by

$$\left[\mathbf{K} - \omega^2 \mathbf{M}\right] \mathbf{q} = \mathbf{f}, \tag{13}$$

with $\mathbf{K}$, $\mathbf{M}$, and $\mathbf{f}$ being the stiffness matrix, mass matrix, and force vector, respectively. Inserting Eq. (12) into Eq. (13) leads to

$$\left[\mathbf{K} - \omega^2 \mathbf{M}\right] \Lambda_{\mathrm{R}} \mathbf{q}_1 = \mathbf{f}. \tag{14}$$

Assuming no external forces, the sum of nodal forces connected to node 1 is zero. Thus,

$$\Lambda_{\mathrm{L}} \mathbf{f} = 0, \tag{15}$$

with

$$\Lambda_{\mathrm{L}} = \begin{bmatrix}\mathbf{I} & \lambda_x^{-1} \mathbf{I} & \lambda_y^{-1} \mathbf{I} & \lambda_x^{-1} \lambda_y^{-1} \mathbf{I}\end{bmatrix}, \tag{16}$$

can be written. Premultiplying Eq. (14) with Λ_{L} leads to a reduced eigenvalue problem with

$$\Lambda_{\mathrm{L}} \left[\mathbf{K} - \omega^2 \mathbf{M}\right] \Lambda_{\mathrm{R}} \mathbf{q}_1 = 0. \tag{17}$$

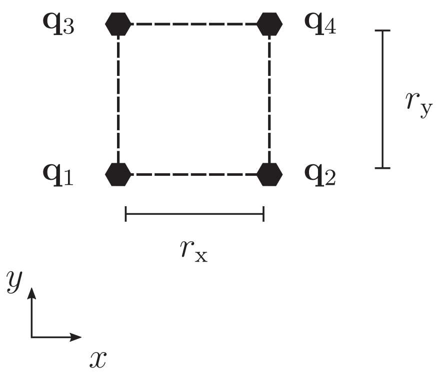

Fig. 1. Generalized displacements **q** at various points in case of two-dimensional periodicity, based on [37].

The solution of the eigenvalue problem from Eq. (17) is a function of the propagation constants μ_x, μ_y. $\omega(\mu_x, \mu_y)$ characterizes the free wave propagation in the structure. It has to be solved for any combination of the propagation constants within the first Brillouin zone (BZ) with $\mu_x, \mu_y = [-\pi, \pi]$ [11]. Usually, the results are depicted in three-dimensional plots showing the dispersion surfaces. Thus, it is possible to identify omni-directional band gaps where no free wave propagation is possible. In case of symmetric unit cells, the calculation can be reduced to the irreducible Brillouin zone (IBZ) or to the contour of the IBZ. The three-dimensional plot of dispersion surfaces is then reduced to a two-dimensional plot of dispersion curves. This is discussed in detail in Ref. [10]. A detailed elaboration of the theory, known as wave finite element method, can be found in Refs. [37–39].

2.3. Experimental investigation

Experimental investigation is employed to validate the results of the generic model obtained from finite element simulations. In order to achieve a generic model which is comparable to a real ultrasonic transducer, fixed boundary conditions are required, cf. Section 3. These are realized by jointing the investigated structure to a backing with high stiffness and large mass compared to the structure. The velocity perpendicular to the sound radiating surface is measured at 351 scanning points with a non-contact measurement using a scanning laser Doppler vibrometer. The excitation is realized with an alternating current electric voltage of 10 V which is applied between the electrodes of the piezoelectric ceramic. Using a so called pseudo-random signal, all frequencies in the range from 0.3 kHz to 25 kHz are excited simultaneously. Furthermore, no leakage effects are introduced by this signal [40]. The obtained resonance frequencies and the related operational deflection shape (ODS) from experimental testing are then employed to validate the numerical simulations.

3. Models

In this section, the investigated models are presented. First, the generic model representing the ultrasonic transducer is discussed. The used finite element model is presented afterwards. Finally, the physical model used for experimental validation of the numerical results is described.

3.1. Generic model

A generic model is used in order to investigate the approach of using spatially distributed stop band material to attain multi-frequency transducers. It consists of a rectangular plate like structure with a sound radiating surface, a piezoelectric ceramic realizing the electro-mechanical coupling, and 112 resonators forming two sections of stop band material, cf. Fig. 2 (a) (II). The plate like structure and the resonators are made of plastics. Different configurations of the plate boundary conditions are realized with blocks of aluminum. In the first configuration CON1 only the shorter edges of the plate like structure are fixed, cf. Fig. 2 (a). This configuration is comparable to ultrasound transducers presented in Ref. [41]. A second configuration CON2 is achieved by additional, partial fixing of the long edges of the plate like structure, cf. Fig. 2 (b). Using two different configurations of the boundary conditions, it is possible to ensure that the behavior at the second operating frequency is caused by the band gap behavior of the structure. If this is the case, the second operating frequency should be mainly independent of the plate like structure boundary conditions. With regard to automotive applications, smaller and more complex transducer geometries are relevant. The authors presented a study with such geometries in Ref. [29]. However, the investigation of the generic model offers the possibility to separate the effects introduced by the stop band material from other geometrical effects. Once proofed, the principle of spatially distributed stop band material can be transferred without difficulty.

3.2. Finite element model

The dynamic behavior of the generic model is investigated in a finite element (FE) simulation. The employed model, cf. Fig. 3, consists of 20-node brick elements with quadratic interpolation functions (Element type in Abaqus: C3D20) [42]. In order to avoid mesh dependencies, the guidelines given in Ref. [43] are applied. The calculations are carried out with the commercial software Simulia Abaqus 2017. The contact between different parts is modeled as tie constraint with a surface-to-surface formulation. All materials are assumed to have linear elastic behavior according to Hooke's law. Table 1 shows the material properties applied in the FE-simulation. The piezoelectric ceramic is similar to PZT-5a [44]. Hence, the material properties are comparable to that presented in Ref. [45]. In a harmonic analysis, the forced response function is calculated. As a result, resonance frequencies can be identified. The excitation is realized by applying an electric voltage to the piezoelectric ceramic. Afterwards, the calculated surface velocity of the plate like structure is used to obtain the radiated sound field using the Rayleigh integral.

3.3. Physical model setup

The experimental validation of the approach requires a physical model, cf. Fig. 4. The plate like structure and the resonators are manufactured as a monolithic using additive manufacturing techniques. PolyJet [47] technology offers the possibility to produce fully filled, solid structures. In a following step, the piezoelectric ceramic is jointed to the downside of the plate like

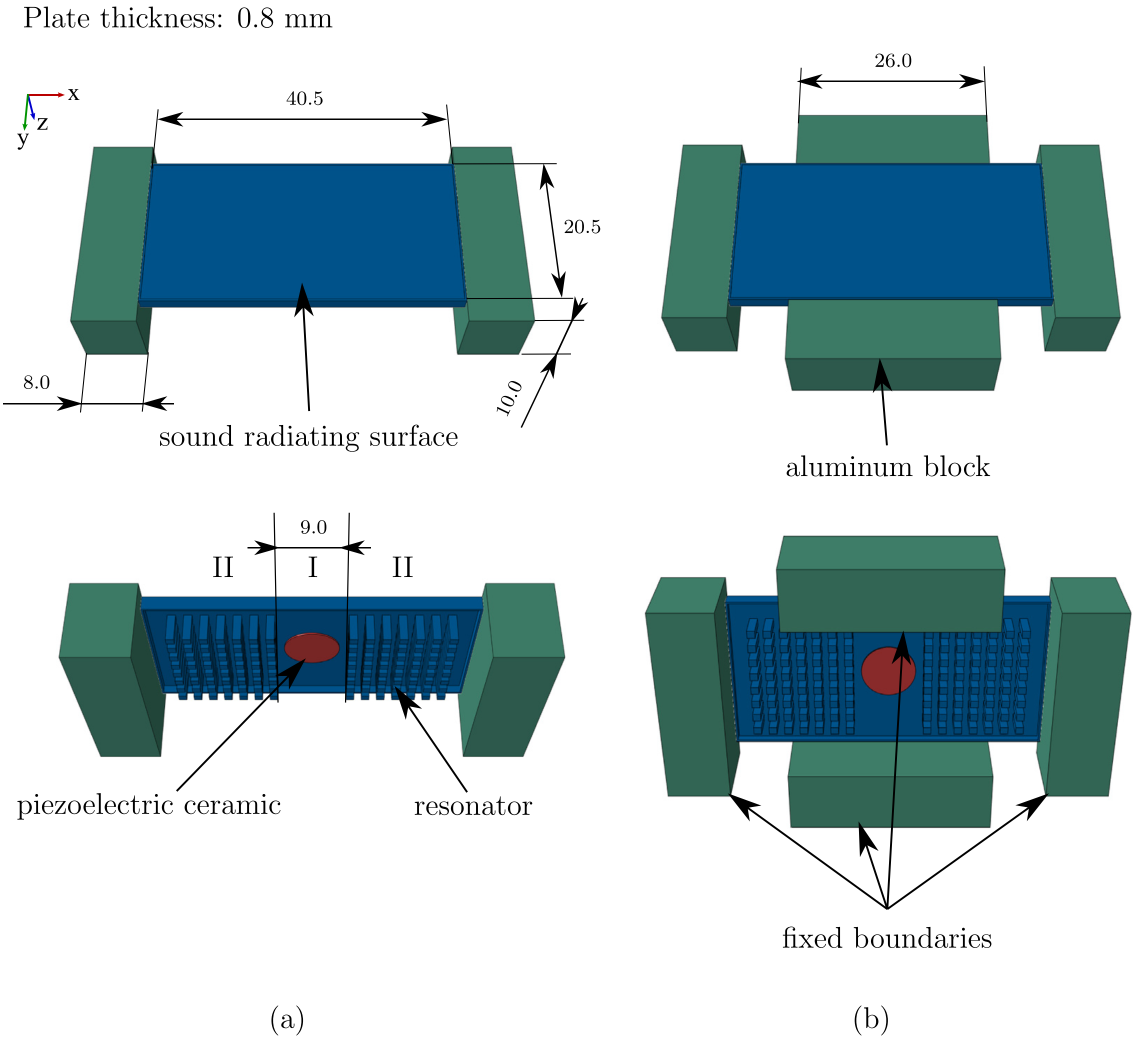

Fig. 2. Generic model to investigate the behavior of spatially distributed stop band material. It consists of a plate like structure with a middle section (I) containing the piezoelectric ceramic and two outer sections (II) with 2 × 56 resonators on the downside forming the stop band material. The top side of the generic model represents the sound radiating surface of an ultrasonic transducer. Two different configurations CON1 (a) and CON2 (b) are realized by assembling aluminum blocks. Thus, different boundary conditions of the plate like structure are realized. The dimensions of the generic model are given in mm.

Table 1
Material parameters of aluminum and the photopolymer VeroWhitePlus RGD 835 [46].

	VeroWhite	Aluminum
Density [$\frac{g}{cm^3}$]	1.17	2.69
Poisson's ratio [−]	0.33	0.33
Young's modulus [MPa]	3200	70000

structure. The assembly is finished by jointing the aluminum blocks according to configuration CON1, cf. Fig. 2 (a), to the plate like structure. In order to realize the fixed boundaries, the entire assembly is jointed to a backing having a large mass and high stiffness compared to the plate like structure. After the experimental investigation of the test structure, additional aluminum blocks are added to the plate like structure. Hence, configuration CON2, cf. Fig. 2 (b), is realized using the same specimen. Testing one and the same structure with both configurations, allows the comparison of the results without additional influences from manufacturing and assembling of the plate like structure and the piezoelectric ceramic.

4. Results

In this section, the results obtained from the numerical simulations and experiments are presented. First, the operational deflection shapes of the two configurations are compared. The sound radiation behavior at certain resonance frequencies is depicted using polar plots. Finally, the numerical results are validated by experimental results. Therefore, the ODSs between

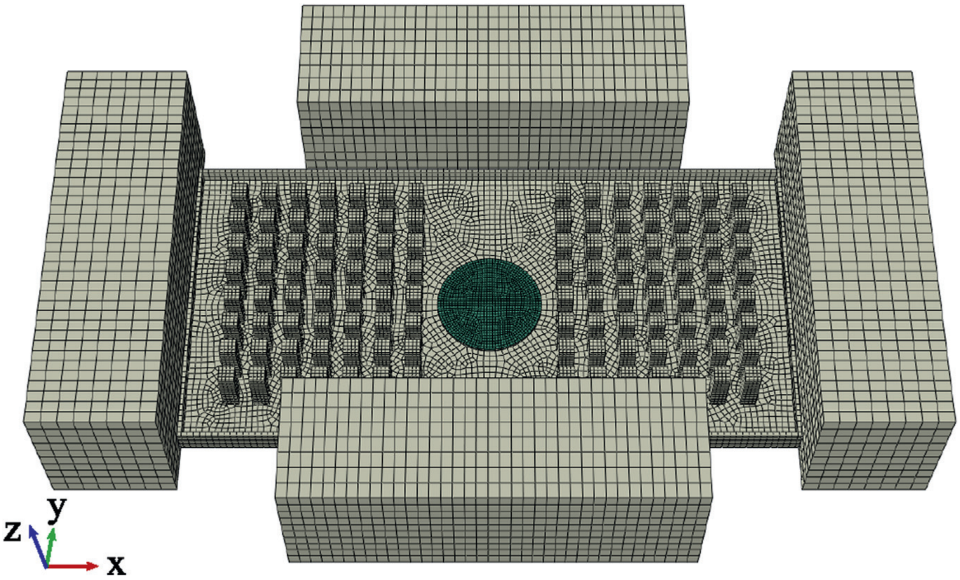

Fig. 3. Finite element model of configuration CON2. It consists of 20 node brick elements with quadratic interpolation functions.

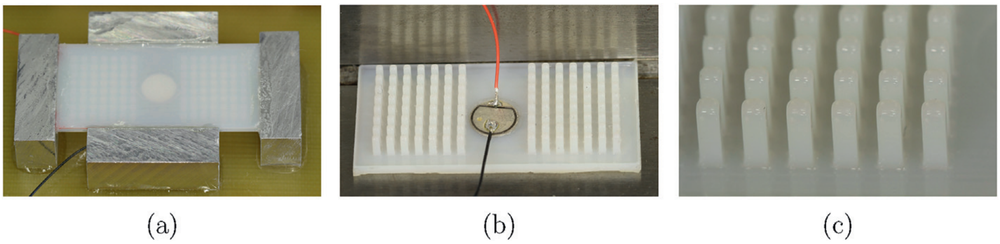
(a)
(b)
(c)

Fig. 4. Physical model for experimental validation. (a) Assembly of the configuration CON2 with fixed boundary conditions at all edges. (b) Downside of the plate like structure with resonators as one part and jointed piezoelectric ceramic in the center. (c) Detailed view of resonators.

numerical simulations and experiments are compared.

4.1. Operational deflection shape and stop band behavior

The operational deflection shape of the plate surface characterizes the sound radiation behavior. In order to generate the desired directivity pattern with small side lobes, the ODS should be similar to the first normal mode. This could be either the

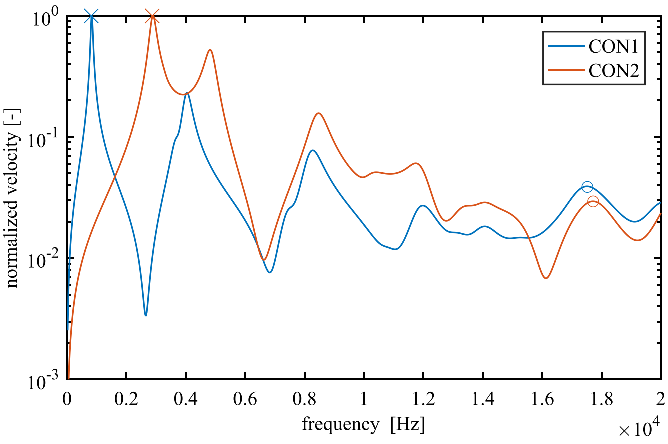

Fig. 5. Frequency response function of normalized velocity at the center point of the sound radiating surface. First and second operating frequencies are identified by × and ∘, respectively. The first operating frequency is influenced by the boundary conditions. In contrary, the second one is mainly independent of the additional boundary conditions in configuration CON2. Other peaks in the frequency response function correspond to ODSs which do not show suitable sound radiation behavior for surround sensing purposes.

entire structure or only a part of the structure while the rest remains in equilibrium position. Achieving the first case is rather trivial. The operating frequency coincides with the first eigenfrequency of the plate like structure. Due to the different boundary conditions in configurations CON1 and CON2, the lowest operating frequencies are obtained at 0.83 kHz and 2.9 kHz, respectively. These can be identified in the frequency response function (FRF) shown in Fig. 5 highlighted by × . The corresponding ODSs are depicted in Fig. 6.

An ODS where a part of the structure behaves similar to the first normal mode while the rest remains in equilibrium position is achieved at higher frequencies. This frequency is highlighted by ∘ in Fig. 5 for each configuration. At 17.5 kHz and 17.7 kHz in configurations CON1 and CON2, respectively, the middle section of the plate like structure shows an ODS where almost all nodes move with the same phase. The outer sections, consisting of stop band material, remain almost without displacement, cf. Fig. 6. The additional boundary conditions in configuration CON2 have only small influence on the resulting operating frequency. Hence, the operating frequency OF2 is mainly independent of the additional boundary conditions. This ODS seems suitable to serve as a second operating point. The ODS of both configurations are pretty similar. However, at the boundary of the plate like

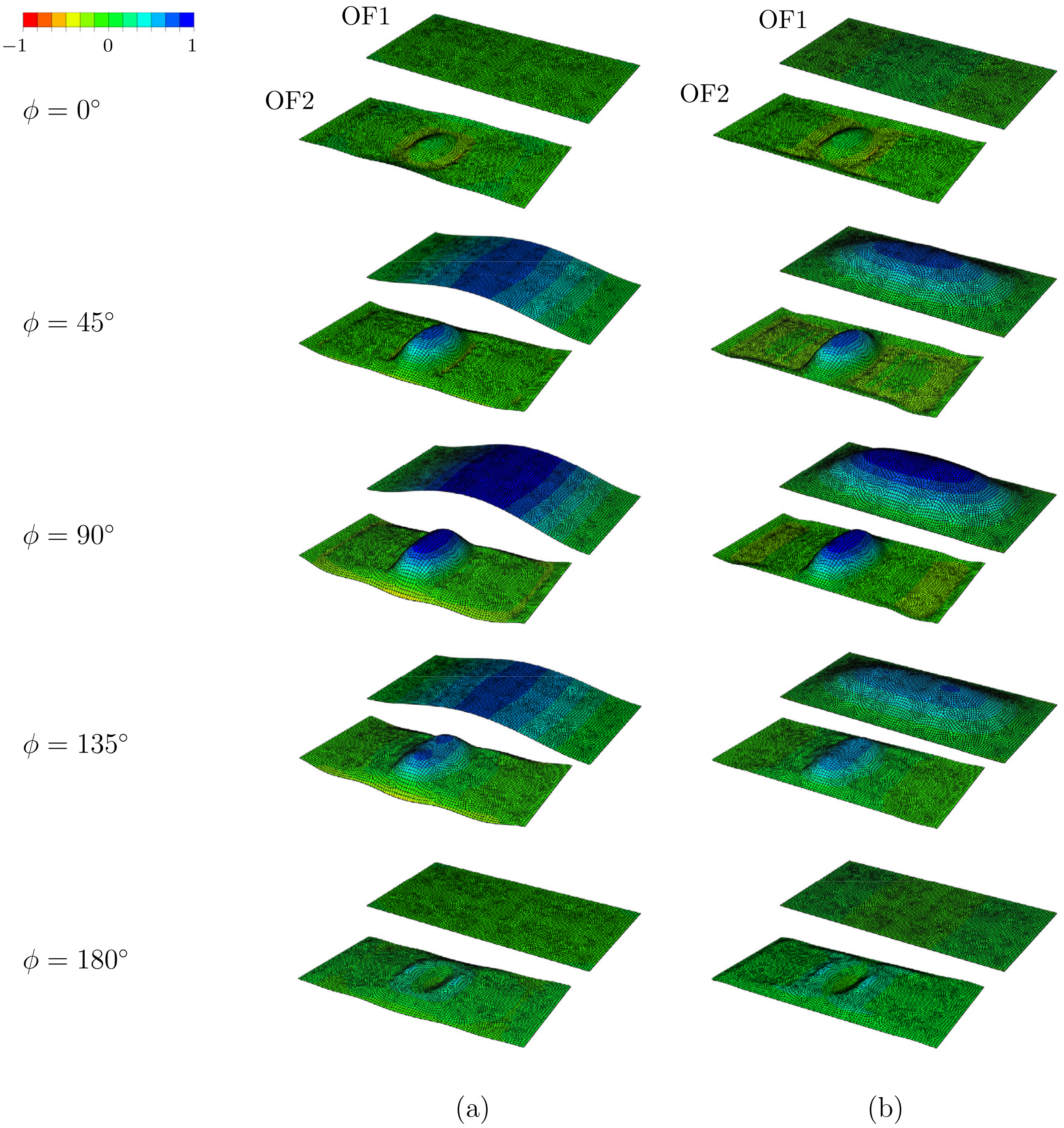

Fig. 6. Operational deflection shape at first (OF1) and second operating frequency (OF2) of the sound radiating surface obtained from finite element simulation. The coloring shows the normalized displacement perpendicular to the undeformed surface. For a better understanding, the phase angels are shown from 0° to 180° in steps of 45°. In case of the second operating frequency, the operational deflection shapes are similar in configuration CON1 (a) and configuration CON2 (b) at all phase angels ϕ. The middle section shows high displacement while the outer sections remain almost in equilibrium position.

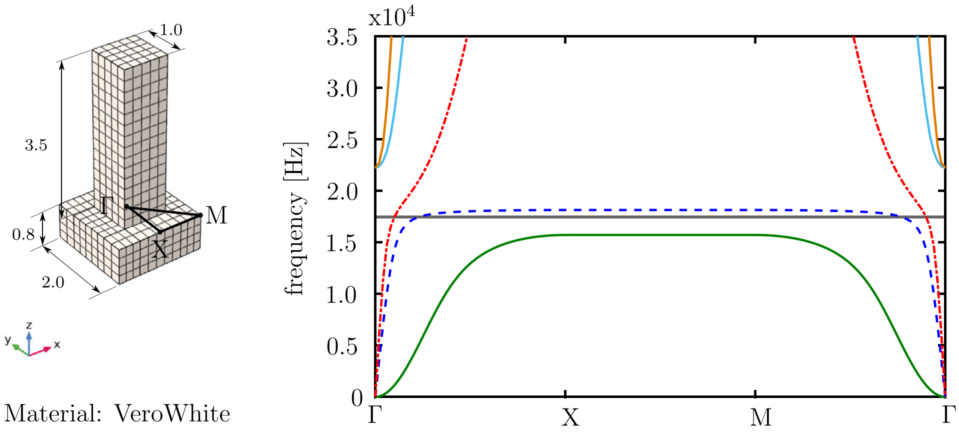

Fig. 7. Unit cell of the stop band material and dispersion curves to identify stop bands for configurations CON1 and CON2. The dispersion curves are related to different wave types. Stop band behavior is found for shear waves (– –) and bending waves (——). Longitudinal waves (- - -) can pass the unit cell at all frequencies. The dimensions of the unit cell are given in mm.

structure a difference in the ODS can be found. This is due to the missing boundary conditions in configuration CON1.

In order to characterize the band gap behavior of the outer plate sections, the dispersion curves are investigated. Fig. 7 shows the unit cell consisting of a plate like structure and a beam with quadratic cross-section. In order to identify band gaps, the propagation constants are set to fit the contour of the IBZ ΓXM [11]. This is suitable due to the symmetry of unit cell as shown in Ref. [10]. The dispersion diagram shows that a partial stop band is achieved with this type of band gap material. In Ref. [26], a similar unit cell is investigated. It is shown that a band gap is obtained for shear (– –) and bending waves (——) while longitudinal waves (- - -) can pass the unit cell at all frequencies, cf. Fig. 7.

It is found that the second operating frequency of the transducer emerges within the stop band where bending waves can not propagate freely through the outer section of the plate like structure. Consequently, the behavior of the plate like structure at the second operating frequency can be interpreted as follows:

A harmonic dynamic excitation of the plate like structure is introduced in the center using the piezoelectric ceramic. The excitation frequency coincides with the stop band frequency of outer section. Due to the particular dynamic behavior of this section, the bending wave is reflected at the boundary of the stop band material. Thus, the dynamic behavior mainly depends on the stop band material.

4.2. *Directivity patterns*

The sound radiation behavior is a criterion to assess the usability of the presented approach to achieve multi-frequency transducers. The directivity pattern should exhibit an even form without distinctive side lobes. Hence, they are desired to behave similar to monopole or dipole characteristics. The directivity pattern is obtained applying the Rayleigh integral to the sound radiating surface of the generic model. The visualization is usually done in polar plots, cf. Fig. 8. At the first operating frequency, both configurations radiate sound without any side lobes. The directivity patterns at the second operating frequency differ slightly between the two configurations. In case of configuration CON1, the sound pressure level shows a drop to −6 dB in $x-$direction at the center point. In configuration CON2, this drop is reduced to −3 dB. This can be ascribed to lower displacements of the structure at the outer sections due to the additional boundary conditions. In $y-$direction, configuration CON1 shows monopole behavior. In contrast, a characteristic similar to a dipole is found in configuration CON2 in $y-$direction. In this case, the sound pressure levels shows a drop to −14 dB at an angle of ±71°. However, in test both cases the directivity pattern does not show distinctive side lobes.

4.3. *Experimental results*

From experimental testing, the resonance frequencies and the related ODS are obtained. Comparing these results with results from numerical simulation, it is possible to validate the employed FE-model. Table 2 shows the operating frequency from FE-simulation and experimental testing. Regarding the first operating frequency, the deviation between simulation and experiment is less than 4% in both configurations. Thus, a suitable accuracy of the applied finite element model is validated.

Considering the second operating frequency, the deviation from numerical results increases to almost 15%. However, the ODSs of the second operating frequency exhibit equal behavior in FE-simulation and experimental testing, cf. Fig. 9. As the second operating frequency is equal for both configurations CON1 and CON2, it is experimentally proved that the additional fixation of the plate like structure has no influence on the second operating frequency for in the investigated configurations.

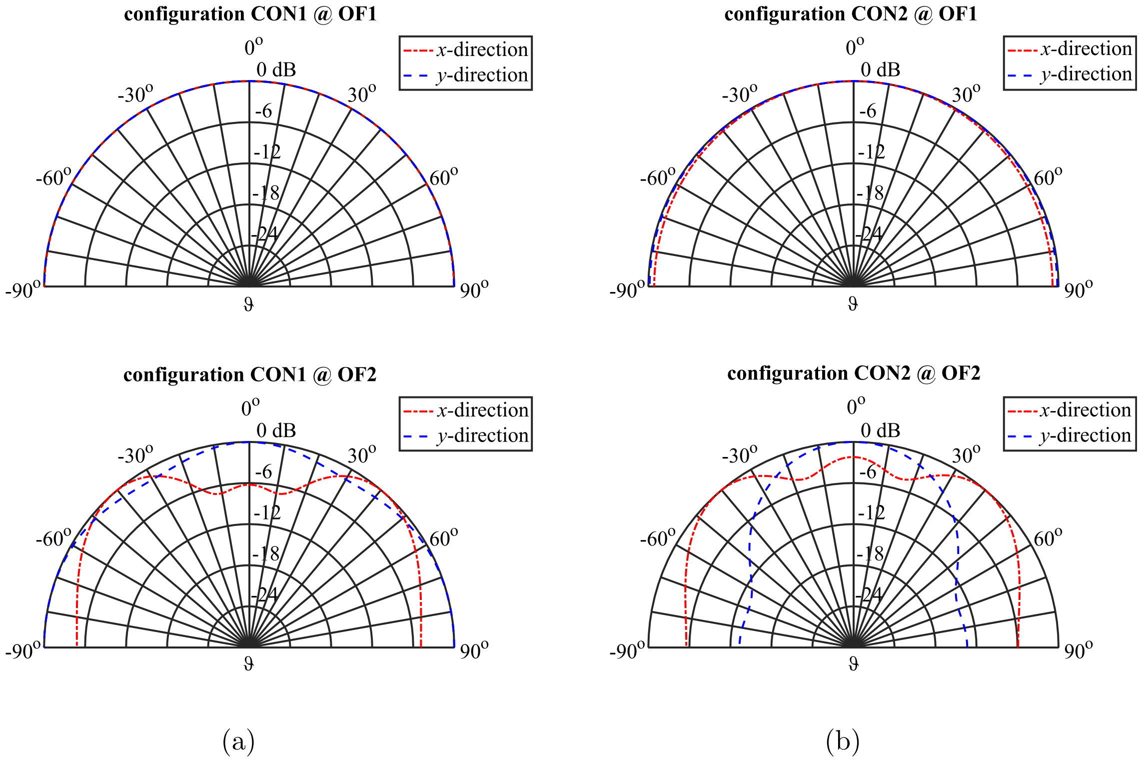

Fig. 8. Directivity patterns of configurations CON1 (a) and CON2 (b) at the first (OF1) and second (OF2) operating frequency. The polar plots show the sound pressure level in $x-$ and $y-$direction which are defined by $\varphi = 0°$ and $\varphi = 90°$, respectively.

Table 2
Results from numerical simulation and experiment.

		Simulation [kHz]	Experiments [kHz]
CON1	1^{st} operational frequency	0.83	0.8
	2^{nd} operational frequency	17.5	20.1
CON2	1^{st} operational frequency	2.9	2.8
	2^{nd} operational frequency	17.7	20.2

4.4. Discussion

Summarizing the results, the dynamic behavior can be divided into two categories. In the first category, the excitation frequency does not coincide with the frequency of the stop band. In this case, the vibrational behavior of the plate like structure is similar to that known from classical plate theory. Thus, the boundary conditions have significant influence on the resonance frequencies and the corresponding ODSs. In the second category, the excitation frequency is in the range of the stop band. In this case, a particular dynamic behavior of the system is found. This leads to ODSs where a part of the structure behaves similar to the first normal mode while the rest remains in equilibrium position. The behavior can be interpreted as follows. The wave is excited by the piezoelectric ceramic. In section 1, the wave is freely propagated. In contrast, no free wave propagation is possible in section 2 due to the coincidence of the excitation frequency and the frequency range of the stop band. Thus, the wave gets reflected at the edge of section 2. Hence, it becomes clear that the operating frequency OF2 is found within the frequency range of the stop band for bending waves. By the geometrical design of zone I, the resulting ODS as well as the operating frequency laying within the stop band can be adjusted.

Investigating two different configurations, it is shown that the effect is caused by the stop band behavior of the structure rather than by the boundary conditions. These findings could also be transferred to other applications where certain dynamic behavior is desired independently from the boundary conditions. Hence, the same design could be used in various applications without influencing the dynamic behavior. In the present test case, this effect leads to a suitable sound radiation for both configurations. The results of the directivity pattern in this study must be seen in the context of the generic model. As the directivity pattern strictly depends on the operating frequency and the dimensions of the radiator, the results of the generic model can not be transferred directly to real transducer applications. However, the results are suitable to estimate the potential of spatially distributed stop band material. Due to the additional boundary conditions in

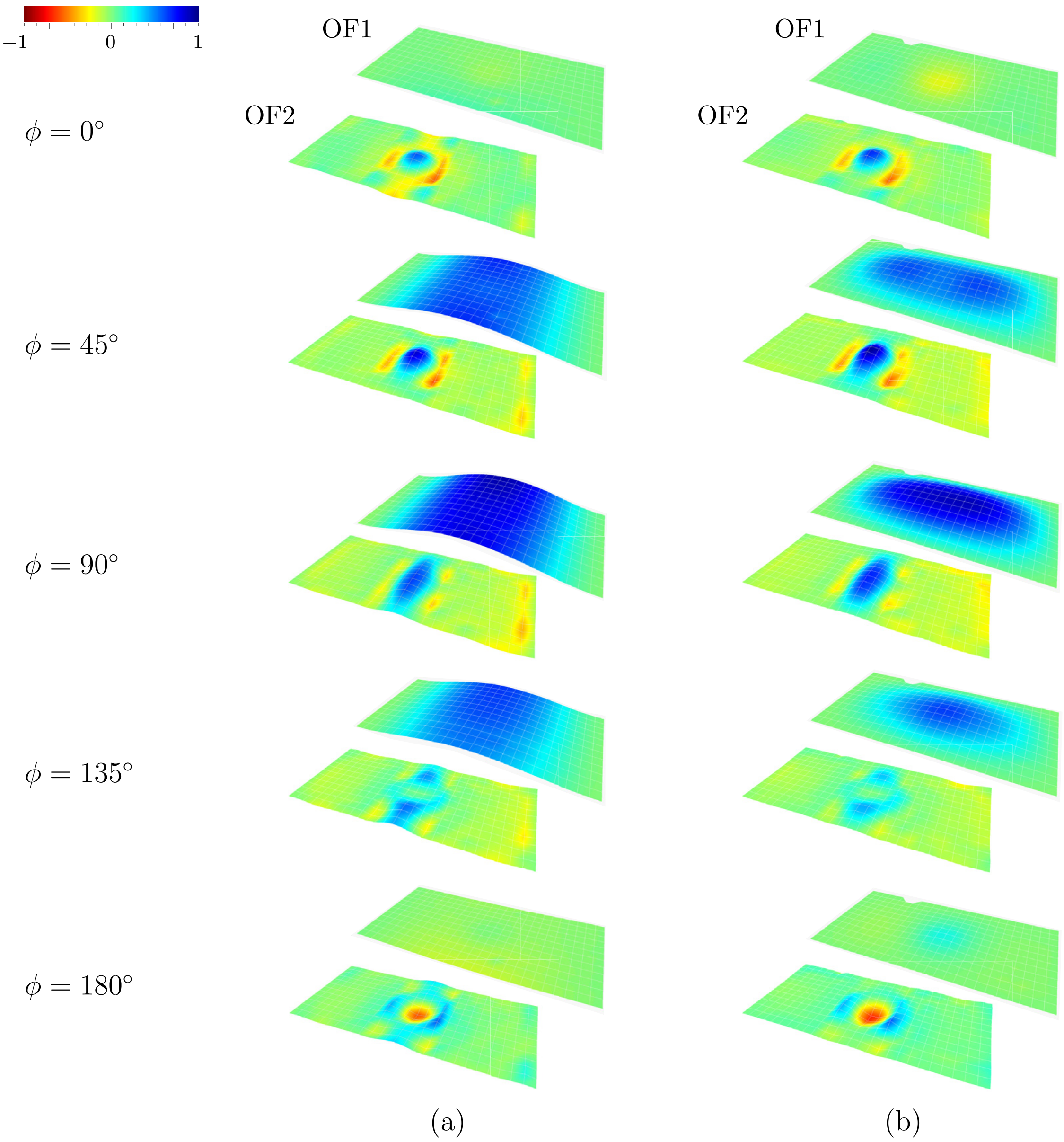

Fig. 9. Operational deflection shape at first (OF1) and second operating frequency (OF2) of the sound radiating surface obtained from experimental testing. The results are similar to that presented in Fig. 6. The coloring shows the normalized displacement perpendicular to the undeformed surface. For a better understanding, the phase angels are shown from 0° to 180° in steps of 45°. In case of the second operating frequency, the operational deflection shapes are similar in configurations CON1 (a) and CON2 (b) at all phase angels ϕ. The middle section shows high displacement while the outer sections remain almost in equilibrium position.

configuration CON2, a more even directivity pattern is obtained. Hence, this configuration is more suitable to build multi-frequency ultrasonic transducers. In order to achieve more even directivity patterns at the second operating frequency, fixed boundary conditions along all edges should be considered. The investigation shows that the operating frequencies are not coupled to each other. Hence, it is possible to tune the operating frequencies mainly independently from each other.

Furthermore, the piezoelectric ceramic could be surrounded entirely by stop band material. In this case, the waves would be reflected as well when traveling in y−direction which would reduce the displacement of the outer section of the plate like structure. As a result, this would generate a more even directivity pattern. Employing the presented approach, it would be possible to achieve ultrasonic transducers with more than two operating frequencies. Therefore, various types of stop band material should be spatially distributed. Exhibiting stop bands at different frequency bands, multiple operating frequencies could be achieved with suitable sound radiation behavior. In experimental investigation, the results from numerical simulation are validated. Good accordance is found for the first operating frequency in both configurations. The second operating frequency obtained in experimental testing shows higher deviation from the simulation results. This can be ascribed to a lack of accuracy in additive manufacturing processes resulting in resonators with a larger cross-section at the plate side and smaller cross-section at the free end, cf. Fig. 4 (c). Consequently, the center frequency of the stop band is increased in experimental testing in comparison

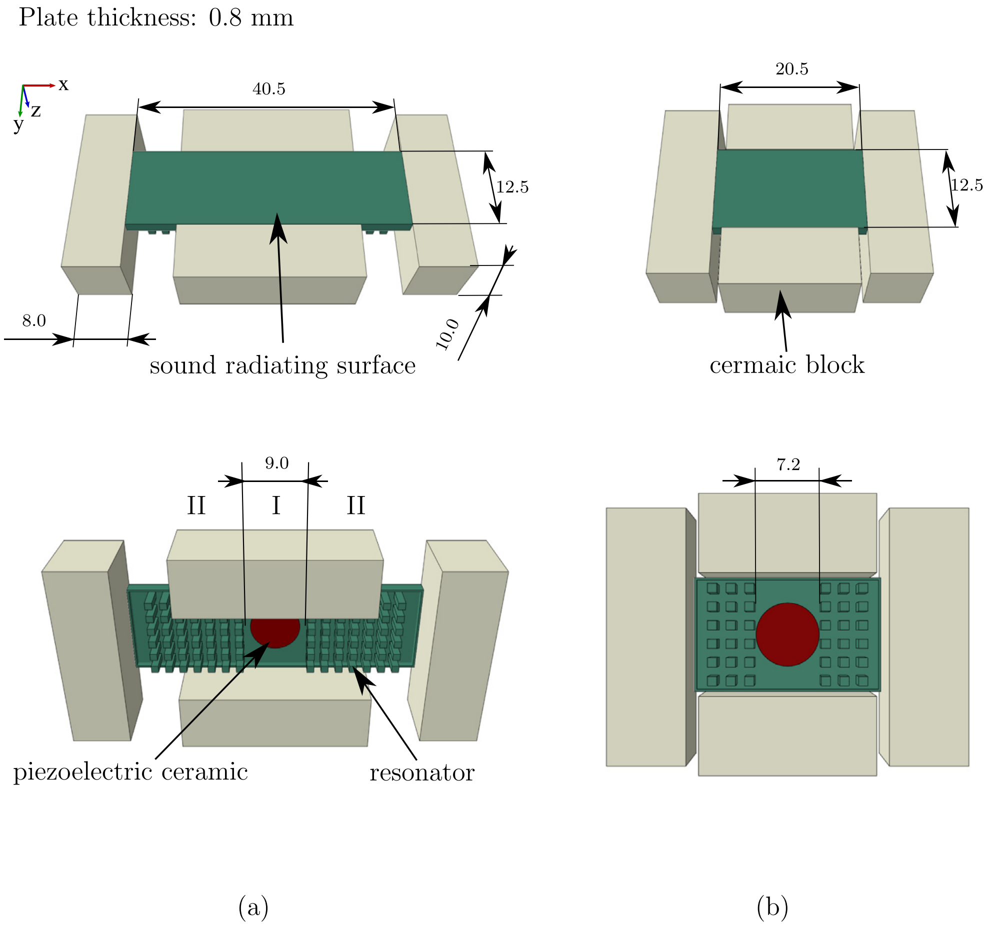

Fig. 10. Models of ultrasonic transducers with multiple operating frequencies in ultrasonic range. (a) CON3 with dimensions similar to the dimensions of the generic model, cf. Fig. 2. (b) CON4 with reduced length in x–direction and reduced width of section 1. The dimensions of the models are given in mm.

to numerical simulation. Finally, this results in an increased second operating frequency. However, the comparison of the ODSs from numerical simulation and experimental testing shows good accordance for both configurations. It is shown that spatially distributed stop band material is a suitable approach to achieve multi-frequency ultrasonic transducers. Thus, it is possible to overcome the drawbacks of known multi-frequency ultrasonic transducer concepts.

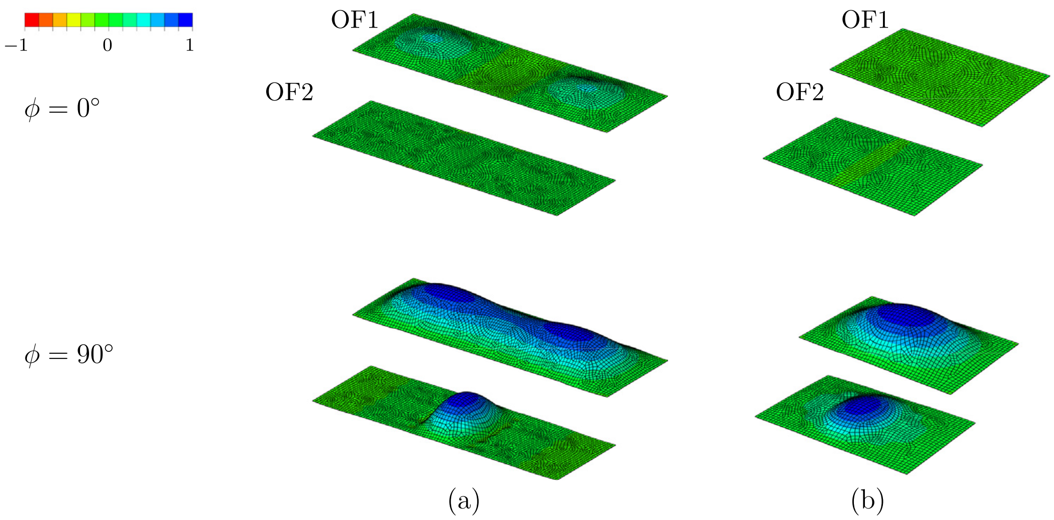

Fig. 11. Operational deflection shape at first (OF1) and second operating frequency (OF2) of the sound radiating surface obtained from finite element simulation. The coloring shows the normalized displacement perpendicular to the undeformed surface. For the sake of brevity, only the phase angles 0° and 90° are shown.

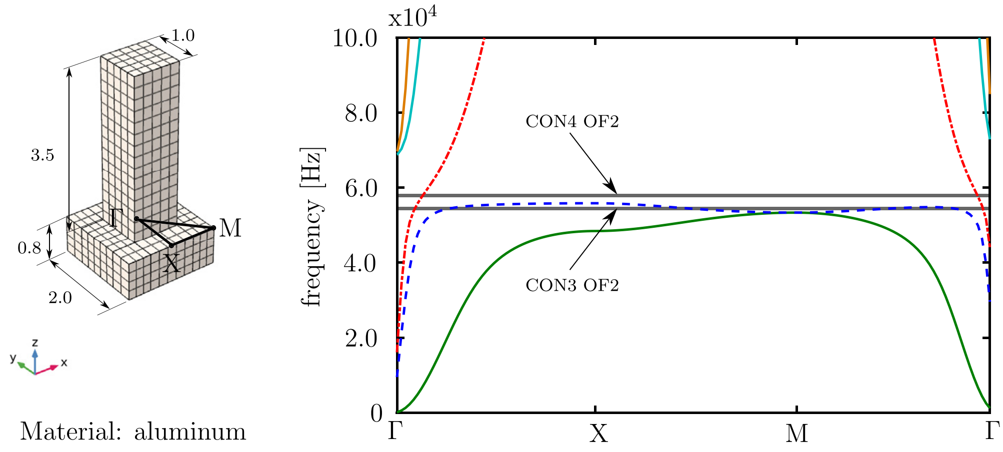

Fig. 12. Unit cell of the stop band material and dispersion curves to identify stop bands for configuration CON3 and CON4. The dispersion curves are related to different wave types. Stop band behavior is found for shear waves (– –) and bending waves (——). Longitudinal waves (- - -) can pass the unit cell at all frequencies. The dimensions of the unit cell are given in mm.

5. Transfer to ultrasonic frequency range

For practical use, the previously presented results need to be transferred to the ultrasonic frequency range. This can be achieved by changing the material as well as by adjusting the geometry of the transducer. In this section, two additional configurations are presented with both operating frequencies in the ultrasonic range (> 16 kHz [48]). Configurations CON3 and CON4 are introduced in Fig. 10.

In contrast to CON1 and CON2, the configurations for the ultrasonic frequency range are made of aluminum. Due to the high ratio from Young's modulus to mass density, the operating frequency increases compared to the previous configurations which were made of plastics. In order to realize proper boundary conditions of the plate like structure, the blocks are considered to consist of ceramic material. The geometrical design of configuration CON3 is similar to the one of CON2. Only the plate width in $y-$direction is reduced and the corresponding resonators are removed. This is necessary to ensure that the ODS of a part of

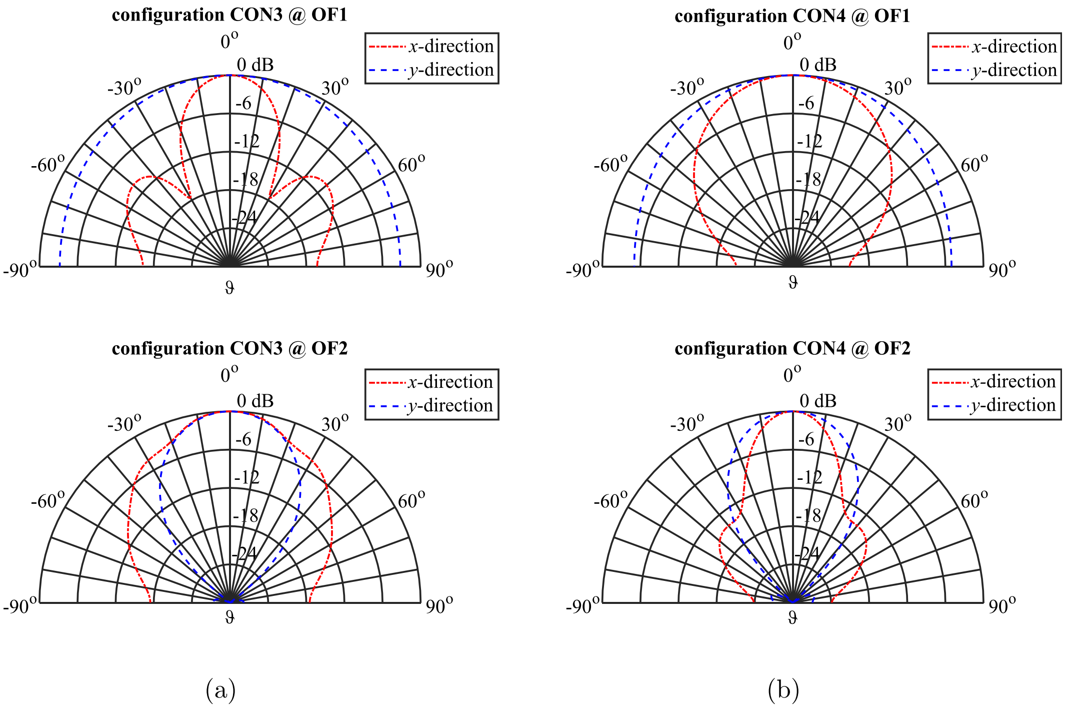

(a)

(b)

Fig. 13. Directivity patterns of configurations CON3 (a) and CON4 (b) at the first (OF1) and second (OF2) operating frequency. The polar plots show the sound pressure level in $x-$ and $y-$direction which are defined by $\varphi = 0°$ and $\varphi = 90°$, respectively.

the structure behaves similar to the first normal mode if the OF2 is increased. In configuration CON4, the length of the plate in $x-$direction is reduced additionally and the corresponding resonators are removed. Thus, the OF1 is increased.

The operational deflection shapes of both operating frequencies are shown in Fig. 11. OF1 arises at 18.9 kHz and 23.7 kHz for CON3 and CON4, respectively. The second operating frequency OF2 is achieved at 55.2 kHz and 58.5 kHz for CON3 and CON4, respectively. Thus, the results found for the generic model in the previous sections can be reproduced numerically also in the ultrasonic range. Fig. 12 shows the dispersion curves for the configurations CON3 and CON4. OF2 coincides with the stop band for bending waves in a similar way as found in the generic model. The dimensions of zone I are different in configurations CON3 and CON4. As a result, the second operating frequency OF2 differs between configurations CON3 and CON4. However, both are found in the frequency range of the stop band for the bending waves. The resulting directivity patterns show suitable sound radiation behavior for the use in surround sensing applications, cf. Fig. 13. Thus, it is shown, that spatially distributed stop band material is a suitable approach to achieve multi-frequency ultrasonic transducers.

6. Conclusion

A study on multi-frequency ultrasonic transducers with spatially distributed stop band material has been presented. The desired ultrasonic transducer is required to work at different operating frequencies using only one electro-mechanical coupling element. The directivity pattern of the radiated sound field needs to be even and should not show distinctive side lobes. In a generic model, the effect of spatially distributed stop band material is investigated in order to fulfill these requirements. The approach is studied with different boundary conditions of the generic model. Finite element simulation is employed to identify the operating frequencies and the belonging ODSs. The results are used to calculate the directivity pattern of the radiated sound field using the Rayleigh integral. In experimental testing, the results of the numerical simulation are validated. The obtained ODSs show good accordance between simulation and experiment.

The authors conclude that:

(i) spatially distributed stop band material is identified as a suitable solution to achieve multi-frequency ultrasonic transducers using only one electro-mechanical coupling element,
(ii) the second operating frequency is related to the frequency of the stop band,
(iii) the second operating frequency achieved by the introduction of spatially distributed stop band material and the belonging ODSs are mainly independent of additional boundary conditions in configurations CON1 and CON2,
(iv) suitable sound radiation behavior is achieved at two well separated operating frequencies, and
(v) distinctive operating frequencies can be tuned mainly independently from each other.

The presented approach offers a possibility to design multi-frequency ultrasonic transducers with only one electro-mechanical coupling element and suitable sound radiation properties at the same time. Thus, the previously discussed drawbacks of known concepts can be overcome. This is a major contribution to increase the surround sensing performance and reliability of ultrasonic transducers.

Acknowledgements

The authors gratefully acknowledge Robert Bosch GmbH Germany for the funding of this research.

Appendix A. Supplementary data

Supplementary data to this article can be found online at https://doi.org/10.1016/j.jsv.2019.03.026.

References

[1] R. Lerch, G. Sessler, D. Wolf, Technische Akustik: Grundlagen und Anwendungen (Technical acoustics: Basics and applications), Springer Berlin Heidelberg, 2009.
[2] F.P. Bundy, Characteristics of stepped-frequency transducer elements, J. Acoust. Soc. Am. 20 (3) (1948) 297–304.
[3] I. Ostrovskii, L. Cremaldi, Split-mode ultrasonic transducer, J. Acoust. Soc. Am. 134 (2) (2013) 1715–1723.
[4] T. Wang, C. Lee, Electrically switchable multi-frequency piezoelectric micromachined ultrasonic transducer (pmut), in: 2016 IEEE 29th International Conference on Micro Electro Mechanical Systems (MEMS), 2016, pp. 1106–1109.
[5] M. Maadi, R.J. Zemp, Self and mutual radiation impedances for modeling of multi-frequency CMUT arrays, IEEE Trans. Ultrason. Ferroelectr. Freq. Contr. 63 (9) (2016) 1441–1454.
[6] R. Chopra, C. Luginbuhl, F.S. Foster, M.J. Bronskill, Multifrequency ultrasound transducers for conformal interstitial thermal therapy, IEEE Trans. Ultrason. Ferroelectr. Freq. Contr. 50 (7) (2003) 881–889.
[7] M. Burtnyk, W.A. N'Djin, L. Persaud, M. Bronskill, R. Chopra, Acoustic characterization of multi-element, dual-frequency transducers for high-intensity contact ultrasound therapy, AIP Conf. Proc. 1481 (1) (2012) 26–31.
[8] I. Muttakin, S.M. Nooh, E. Supriyanto, Spice modeling of hybrid multi-frequency ultrasound transducer, in: Proceedings of the 10th WSEAS International Conference on System Science and Simulation in Engineering, World Scientific and Engineering Academy and Society (WSEAS), Stevens Point, Wisconsin, USA, 2011, pp. 106–111.
[9] C. Sun, F. Dai, S. Jiang, Y. Liu, A novel single-element dual-frequency ultrasound transducer for image-guided precision medicine, in: 2017 IEEE International Ultrasonics Symposium (IUS), 2017, pp. 1–4.

[10] F. Maurin, C. Claeys, E. Deckers, W. Desmet, Probability that a band-gap extremum is located on the irreducible brillouin-zone contour for the 17 different plane crystallographic lattices, Int. J. Solids Struct. 135 (2018) 26–36.
[11] L. Brillouin, Wave Propagation in Periodic Structures: Electric Filters and Crystal Lattices, Dover Publications, 1953.
[12] Z.-J. Yao, G.-L. Yu, Y.-S. Wang, Z.-F. Shi, Propagation of bending waves in phononic crystal thin plates with a point defect, Int. J. Solids Struct. 46 (13) (2009) 2571–2576.
[13] Z. Liu, X. Zhang, Y. Mao, Y.Y. Zhu, Z. Yang, C.T. Chan, P. Sheng, Locally resonant sonic materials, Science 289 (5485) (2000) 1734–1736.
[14] C.C. Claeys, K. Vergote, P. Sas, W. Desmet, On the potential of tuned resonators to obtain low-frequency vibrational stop bands in periodic panels, J. Sound Vib. 323 (2013) 1418–1436.
[15] M. Rupin, F. Lemoult, G. Lerosey, P. Roux, Experimental demonstration of ordered and disordered multiresonant metamaterials for lamb waves, Phys. Rev. Lett. 112 (2014) 234301.
[16] C.C. Claeys, P. Sas, W. Desmet, On the acoustic radiation efficiency of local resonance based stop band materials, J. Sound Vib. 333 (2014) 32033213.
[17] Y. Song, L. Feng, J. Wen, D. Yu, X. Wen, Reduction of the sound transmission of a periodic sandwich plate using the stop band concept, Compos. Struct. 128 (2015) 428–436.
[18] B. Assouar, M. Oudich, X. Zhou, Acoustic metamaterials for sound mitigation, C. R. Phys. 17 (5) (2016) 524–532 (phononic crystals/Cristaux phononiques).
[19] C. Claeys, E. Deckers, B. Pluymers, W. Desmet, A lightweight vibro-acoustic metamaterial demonstrator: numerical and experimental investigation, Mech. Syst. Signal Process. 70 (2016) 853–880.
[20] H. Ruiz, C. Claeys, E. Deckers, W. Desmet, Numerical and experimental study of the effect of microslits on the normal absorption of structural metamaterials, Mech. Syst. Signal Process. 70–71 (2016) 904–918.
[21] X. Wang, H. Zhao, X. Luo, Z. Huang, Membrane-constrained acoustic metamaterials for low frequency sound insulation, Appl. Phys. Lett. 108 (4) (2016) 041905.
[22] N.G. Rocha de Melo Filho, L. Sangiuliano, C. Claeys, E. Deckers, W. Desmet, Vibro-acoustic metamaterials for increased STL in acoustic resonance driven environments, in: Proceedings: Noise and Vibration Emerging Methods, 2018, p. 13. no. 171978.
[23] T.-C. Wu, T.-T. Wu, J.-C. Hsu, Waveguiding and frequency selection of lamb waves in a plate with a periodic stubbed surface, Phys. Rev. B 79 (2009) 104306.
[24] Y. Xiao, J. Wen, X. Wen, Flexural wave band gaps in locally resonant thin plates with periodically attached spring-mass resonators, J. Phys. D Appl. Phys. 45 (19) (2012) 195401.
[25] Y. Xiao, J. Wen, X. Wen, Sound transmission loss of metamaterial-based thin plates with multiple subwavelength arrays of attached resonators, J. Sound Vib. 331 (25) (2012) 5408–5423.
[26] J. Henneberg, A. Gerlach, H. Storck, H. Cebulla, S. Marburg, Reducing mechanical cross-coupling in phased array transducers using stop band material as backing, J. Sound Vib. 424 (2018) 352–364.
[27] J.W. Baron Rayleigh Strutt, The Theory of Sound, vol. 2, Dover Publications, 1896.
[28] G.H. Koopmann, J.B. Fahnline, Designing Quiet Structures: A Sound Power Minimization Approach, Elsevier Science, 1997.
[29] J. Henneberg, A. Gerlach, H. Cebulla, S. Marburg, Locally structured fiber reinforcements: an approach to realize anisotropic directivity pattern in ultrasound transducers, in: SAE Technical Paper, No. 2018-01-1485, SAE International, 2018, p. 13.
[30] C.-C. Cheng, C.-Y. Lin, W.-J. Wu, K.-C. Wu, C.-K. Lee, Highly anisotropic beam patterns for a pot-like ultrasonic sensor with penetrating slots configuration, in: 2009 IEEE International Ultrasonics Symposium, 2009, pp. 775–778.
[31] D. Fritze, S. Marburg, H.-J. Hardtke, Estimation of radiated sound power: a case study on common approximation methods, Acta Acustica United Acustica 95 (5) (2009) 833–842.
[32] M. Möser, Technische Akustik (Technical Acoustics), tenth ed., Springer-Verlag, Berlin Heidelberg New York, 2015.
[33] M. Möser, Engineering Acoustics: an Introduction to Noise Control, second ed., Springer, 2009.
[34] S. Marburg, Developments in structural-acoustic optimization for passive noise control, Arch. Comput. Methods Eng. 9 (4) (2002) 291–370.
[35] G. Hübner, A. Gerlach, Zusammenhang der DFEM-Schalleistungsbeschreibung mit der Rayleighschen Schallfelddarstellung ebener Strahler (The relation between DFEM sound power description and Rayleigh sound field depicturing of plane sound sources), in: Fortschritte der Akustik/DAGA, 1998, pp. 682–683.
[36] F. Bloch, Über die Quantenmechanik der Elektronen in Kristallgittern (About quantum mechanics of electrons in crystal lattices), Z. Phys. 52 (7–8) (1929) 555–600.
[37] B.R. Mace, E. Manconi, Modelling wave propagation in two-dimensional structures using finite element analysis, J. Sound Vib. 318 (4) (2008) 884–902.
[38] M. Ruzzene, F.L. Scarpa, A general FEM technique to model wave propagation in cellular periodic structures, in: Proc. SPIE 5053, Smart Structures and Materials 2003: Active Materials: Behavior and Mechanics, vol. 5053, 2003, pp. 414–422.
[39] R. Langley, A note on the force boundary conditions for two-dimensional periodic structures with corner freedoms, J. Sound Vib. 167 (2) (1993) 377–381.
[40] Polytec GmbH, Polytec-Platz 1-7, 76337 Waldbronn, Germany, Theory Manual Polytec Scanning Vibrometer PSV Theory, as of Software 9.1 Edition.
[41] M. Abele, K. Bendel, A. Gerlach, M. Liebler, Schallwandler mit zumindest einem Piezoelement ((Ultrasonic transducers with at least one piezo element), German Patent: DE102010062990A1 (June 2012).
[42] Dassault Systemes, Abaqus 2017 Online Documentation - Abaqus Analysis User's Guide, 2017.
[43] P. Langer, M. Maeder, C. Guist, M. Krause, S. Marburg, More than six elements per wavelength: the practical use of structural finite element models and their accuracy in comparison with experimental results, J. Comput. Acoust. 25 (4) (2017) 1750025.
[44] M.W. Hooker, Properties of PZT-Based Piezoelectric Ceramics between -150 and 250°C, Tech. rep., NASA Langley Research Center, 1998.
[45] E. Heinonen, J. Juuti, S. Leppävuori, Characterization and modelling of 3D piezoelectric ceramic structures with ATILA software, J. Eur. Ceram. Soc. 25 (12) (2005) 2467–2470 elecroceramics IX.
[46] Stratasys Ltd, Material Data Sheet - VeroWhitePlus (RGD835), 2016.
[47] Stratasys, Design with Brilliance - Game-Changing Versatility and Realism with the World's Most Advanced Full-Color Multi-Material 3D Printer, 2017.
[48] Deutsches Institut für Normung, (German Institute for Standardization), DIN 1320 Akustik Begriffe (Acoustical Terms), Dec. 2009.

Paper C

Journal of Sound and Vibration 424 (2018) 352–364

Contents lists available at ScienceDirect

Journal of Sound and Vibration

journal homepage: www.elsevier.com/locate/jsvi

Reducing mechanical cross-coupling in phased array transducers using stop band material as backing

J. Henneberg [a,c,*], A. Gerlach [a], H. Storck [a], H. Cebulla [b], S. Marburg [c]

[a] Robert Bosch GmbH, Robert-Bosch-Campus 1, 71272 Renningen, Germany
[b] Technical University Chemnitz, Professorship for Textile Technologies, Reichenhainer Str. 31/33, 09126 Chemnitz, Germany
[c] Technical University of Munich, Chair of Vibroacoustics of Vehicles and Machines, Boltzmann Str. 15, 85748 Garching, Germany

ARTICLE INFO

Article history:
Received 21 September 2017
Revised 31 January 2018
Accepted 15 March 2018
Available online 30 March 2018

Dedicated to Professor Franz Holzweißig on the occasion of his 90th birthday.

Keywords:
Local resonator
Tuned resonator
Stop band material
Acoustic metamaterial
Phased array transducer
Cross-coupling

ABSTRACT

Phased array transducers are widely used for acoustic imaging and surround sensing applications. A major design challenge is the achievement of low mechanical cross-coupling between the single transducer elements. Cross-coupling induces a loss of imaging resolution. In this work, the mechanical cross-coupling between acoustic transducers is investigated for a generic model. The model contains a common backing with two bending elements bonded on top. The dimensions of the backing are small; thus, wave reflections on the backing edges have to be considered. This is different to other researches. The operating frequency in the generic model is set to a low kHz range. Low operating frequencies are typical for surround sensing applications. The influence of the backing on cross-coupling is investigated numerically. In order to reduce mechanical cross-coupling a stop band material is designed. It is shown numerically that a reduction in mechanical cross-coupling can be achieved by using stop band material as backing. The effect is validated with experimental testing.

© 2018 The Authors. Published by Elsevier Ltd. This is an open access article under the CC BY license (http://creativecommons.org/licenses/by/4.0/).

1. Introduction

Phased array structures of acoustic transducers are used for acoustic imaging in medical applications and for nondestructive testing. Furthermore, there are applications for 3D surround sensing. Depending on the field of use, the typical operating frequency varies in a range from lower kHz for surround sensing [1,2] up to several MHz for nondestructive testing [3] and medical applications [4]. One of the characteristic properties of these structures is the cross-coupling between single transducers. It mainly describes the undesired behavior that array elements are not working independently [5]. In several studies it has been shown that cross-coupling influences the performance of a phased array by changing its beam pattern and resulting in a loss of resolution [5–8]. In Ref. [5] a quantitative theory for cross-coupling in ultrasonic transducer arrays is presented. Surface waves in the backing and in the load medium in front of the transducers are indicated as reason for cross-coupling. This theory assumes a series of uniformly distributed, unbacked transducer elements. The cross-coupling is caused by interaction through a semi-infinite substrate, the solid load medium. In Ref. [9] a basic model and influence of cross-coupling with focus on cross-coupling included signals is given. Lamb wave A0 mode has been identified as the responsive effect for cross-coupling in a CMUT-array (capacitive micromachined ultrasonic transducer) with first order resonance at 2.3 MHz [10]. An air-coupled, low frequency phased array is presented in the studies [11]. The ultrasonic transducers are realized with piezoelectric crystals. As

---

[*] Corresponding author. Robert Bosch GmbH, Robert-Bosch-Campus 1, 71272 Renningen, Germany.
E-mail addresses: Johannes.Henneberg@de.bosch.com, johannes.henneberg@tum.de (J. Henneberg).

https://doi.org/10.1016/j.jsv.2018.03.021
0022-460X/© 2018 The Authors. Published by Elsevier Ltd. This is an open access article under the CC BY license (http://creativecommons.org/licenses/by/4.0/).

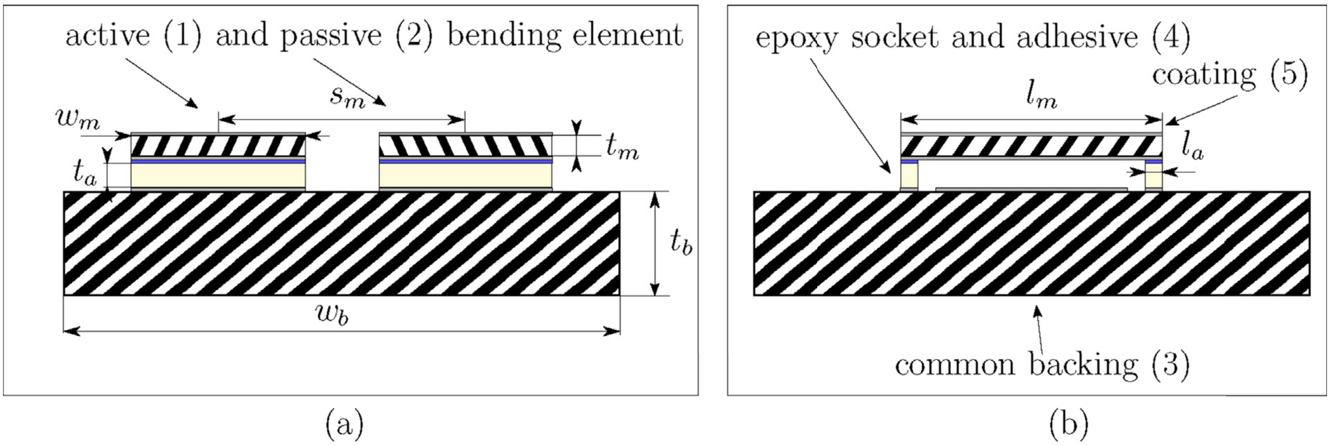

Fig. 1. Investigated generic model with 2 bending elements on a common backing. (a) frontal view, (b) side view.

the used setup with piezoelectric elements and foam as spacer does not cause high cross-coupling, it is not further investigated. In Refs. [12,13] cross-coupling is investigated in a finite element model of a linear, piezoceramic based phased array transducer.

In this study, we investigate the cross-coupling of a generic transducer array model with a low operating frequency at 5.2 kHz. We focus especially on mechanical cross-coupling caused by the common backing without extra lossy regions. The realization of extra lossy regions between every transducer element requires high effort in real structures. Thus, a design without extra lossy regions is desired. Cross-coupling caused by the common backing is the dominating effect in air-coupled transducer arrays. The dimensions of the backing are small, thus wave reflections on the edges of the backing have to be taken into account in simulations of the whole model. This is different to other researches. The design of the backing is a major challenge in phased array transducers with low operating frequency. To overcome this problem, we show that stop band materials can be used to reduce mechanical cross-coupling caused by common backing in phased array structures. Stop band materials, also known as acoustic metamaterials, consist out of periodic structure with particular dynamic behavior in a certain frequency range. Hence it is clarified that stop band material describes a structural but not a material behavior.

In recent years, stop band materials received a growing attention. In analogy to photonic crystals, Ref [14] presents a study with experimental investigation on sonic crystals to design band gap behavior. Therefore, rigid spheres of lead were coated with rubber and placed in an epoxy plate. Stop band materials can decrease acoustical [15] as well as vibrational [16] responses of components in certain frequency bands. Thus, bragg scattering and local resonant structures can be used. As Bragg scattering is based on destructive interference effects [17], a periodic lattice is required. In contrary, resonant stop bands can be achieved by ordered and disordered structures. This is shown for an electromagnetic metamaterial in Ref. [18] and for an acoustic metamaterial in Ref. [19]. However, the scale of the stop band material should be smaller than the wavelength to be attenuated. In this study, ordered periodic resonant structures are investigated. In Ref. [15], it is shown that resonant stop bands have a good prospect for low frequency stop bands. In Ref. [20], it is shown that propagation of flexural waves in thin plates can be attenuated by locally attached spring-mass resonators. In Ref. [21], a possible application for microfabricated phononic crystal waveguides is named but not investigated in detail. The intention is to route and bend acoustic signals from large electro-acoustic transducers to be emitted and detected through small apertures. By this, the resolution of phased array structures can be increased.

Initially we focus on a generic model to investigate the relation between dynamical behavior of the backing and cross-coupling. In finite element simulation, we analyze the dependence of cross-coupling on the backing thickness. Afterwards, we investigate an extended model with stop band material as backing. In simulation as well as in experimental testing, the effect of locally resonant structures with regard to mechanical cross-coupling is shown. Finally, a conclusion is drawn.

2. Cross-coupling in phased array transducer

In this section we give an overview of the investigated generic model. The calculation of cross-coupling is defined and its mechanism is shown for the generic model.

2.1. Generic model setup

In analogy to CMUT-arrays, a generic model is set up with two bending elements bonded on a square, common backing. Each bending element forms an electrode of a capacitive transducer. The counter-electrodes are realized on the common backing. To achieve electrical conductivity, the bending elements and the backing are coated with aluminum (5). The cross-section of this generic model is shown in Fig. 1. The two bending elements (1 + 2) are made of carbon fiber reinforced plastic (CFRP) coated with aluminum. They are bonded with a cyanoacrylate adhesive to epoxy sockets (4) on a common epoxy backing (3).

The dimensions are given in Table 1. This setup is comparable with the setup up given in Ref. [10]. The main differences are

Table 1
Dimensions of the generic setup to investigate the influence of backing thickness on cross-coupling in phased array transducers.

Parameter		Symbol	Value	Parameter		Symbol	Value
Backing	thickness	t_b	1.0–16.0 mm	Bending element	thickness	t_m	0.5 mm
	width	w_b	70.0 mm		width	w_m	6.0 mm
Epoxy socket	thickness	t_a	30 μm		spacing	s_m	24.0 mm
	length	l_a	4.6 mm		length	l_m	30.0 mm

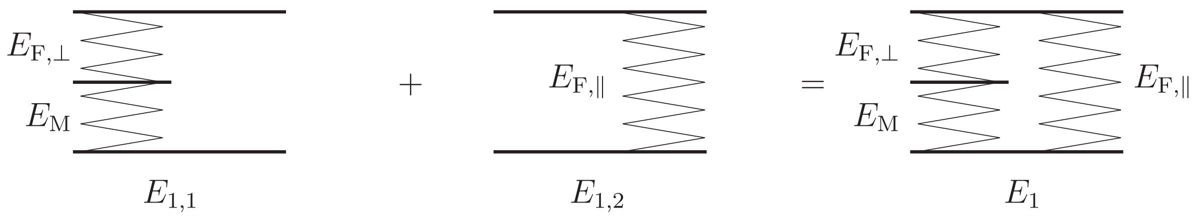

Fig. 2. Rheological model of CFRP along direction 1 according to [22].

- the ratio between bending element thickness and backing thickness,
- the rectangular shape of the bending element,
- the first resonance frequency is much lower and
- there is no extra lossy region.

These differences lead to a different dynamic behavior. Especially the missing extra lossy region causes wave reflection on the edges of the backing. Taking this into account is important to overcome design challenges for the backing in air-coupled phased array transducers with low operating frequency.

All investigations are based on this generic model. The operating frequency in this generic model is set to approximately 5 kHz which is much lower than in surround sensing applications. This finally relieve the specimen preparation for experimental testing. The results can be transferred to higher frequency ranges easily.

2.2. Material model

Composite materials such as CFRP require higher effort to be simulated in a proper way. They consist at least of two different materials and show non-isotropic behavior. Homogenization is a common approach to model these material. By this, the material behavior is described with surrogate parameters which represent the global behavior of the homogenized material. We apply an orthotropic material model which is developed in Ref. [22]. The rheological model assumes a series and parallel circuit of fiber (index$_\mathrm{F}$) and matrix (index$_\mathrm{M}$) material properties. This model is given in Fig. 2.

Eq. (1) describes the behavior as a series circuit of properties of the matrix material and the fiber perpendicular to its axis ($\perp$). $\Phi_{1,1}$ denotes the fiber volume ratio of the fibers perpendicular to its axis within the series circuit, see Fig. 2 $E_{1,1}$. The nonuniform strain in the matrix is considered by Halpin-Tsai method with the semi-empirical factor β [23,24]. Furthermore Eq. (2) describes the material properties of the fiber along its axis ($\|$). The ondulation of woven fabric is taken into account by $\eta \in [0,1]$ which lowers the Young's modulus due to the anisotropic material properties of carbon fibers.

$$E_{1,1} = \frac{\beta \cdot E_\mathrm{M} \cdot E_{\mathrm{F},\perp}}{\Phi_{1,1} \cdot \beta \cdot E_\mathrm{M} + (1 - \Phi_{1,1}) \cdot E_{\mathrm{F},\perp}} \tag{1}$$

$$E_{1,2} = \eta \cdot E_{\mathrm{F},\|} \tag{2}$$

The theory assumes a balanced woven fabric. Thus, the resulting Young's modulus for direction 1 is calculated as given in Eq. (3), where Φ denotes the overall fiber volume ratio of the composite.

$$E_1 = \frac{\Phi}{2} \cdot E_{1,2} + (1 - \frac{\Phi}{2}) \cdot E_{1,1} \tag{3}$$

Young's modulus, shear modulus and Poisson's ratio are calculated for each direction in a similar way as shown above. The entire description of the applied micro-mechanical material model is extensive. The development of the material model is not within the scope of this study. For this reason, the authors refer to literature eg. Refs. [22–25].

The epoxy backing and socket are modeled with an isotropic material behavior. All resulting material parameters are given in Table 2.

Table 2
Material parameters.

	Epoxy backing	Epoxy socket		CFRP
Density [$\frac{g}{cm^3}$]	1.14	4.3		1.32
Damping [–]	0.035	0.010		0.056
Poisson's ratio [–]	0.33	0.38	$\nu 12$	0.15
			$\nu 13$	0.45
			$\nu 23$	0.45
Young's modulus [MPa]	3500	6094	E1	33424
			E2	33424
			E3	4976
Shear modulus [MPa]			G12	1974
			G13	1715
			G23	1715

2.3. Finite element simulation

In finite element simulation, the structural dynamic behavior is investigated. Therefore, the backing, bending elements and epoxy sockets are modeled. The aluminum layer as well as the cyanoacrylate adhesive are not modeled in the simulation. The thickness of the aluminum layer is only a few hundred nanometers thick. The cyanoacrylate adhesive is also applied as a thin layer. We assume ideal adhesion behavior between the components and negligible influence on the mechanical behavior. The load medium is not part of the model. Thus, no fluid-structure interaction is considered. The excitation for a harmonic analysis is realized by a load applied to one, the active, bending element.

The finite element simulation of the generic model is carried out with the commercial software Simulia Abaqus 6.14. All parts are meshed with twenty-node brick elements with reduced number of integration points (C3D20R). The bending elements are modeled with 0.6 mm average element edge length and 5 layers over thickness. The backing is modeled with 1.0 mm average element edge length and 4 layers over thickness. By this, the guidelines given in Ref. [26] are satisfied. The connections between bending elements, epoxy sockets and backing are modeled with tie constraints by a surface-to-surface formulation. The backing has free-free boundary conditions.

2.4. Cross-coupling definition

In a harmonic analysis and in experiment, a load is applied to the active bending element. The cross-coupling between the active and the passive bending elements is then calculated by

$$P_{\mathrm{n}} = 10 \cdot \lg\left(\frac{\widehat{V}_2}{\widehat{V}_1}\right) \mathrm{dB}\ , \tag{4}$$

where V denotes the integral of squared velocity over the whole area of each bending element. As we assume uniformly distributed mass for the bending elements, V represents a kinetic energy equivalent value. To calculate the cross-coupling between the bending elements, the peak at resonance frequency f_{r_n} of each bending element n is used with $\widehat{V}_n = V(f_{r_n})$. It follows that $\widehat{V}_n$ appears at different frequencies for each bending element. Fig. 3 shows a schematic drawing of velocity spectra of the bending elements. In simulation, $\widehat{V}_n$ appears almost at the same frequency due to ideal conditions in setup accuracy. This is different from real setups, where small differences during the preparation process can change the resonance frequency of each bending element. Thus, a comparable and appropriate validation of cross-coupling in the system can be achieved with $\widehat{V}_n = V(f_{r_n})$ in simulation as well as in experimental tests.

2.5. Cross-coupling dependence on backing

Firstly, the influence of the backing thickness on the cross-coupling is investigated in finite element simulation. The first resonance frequency of the bending elements of the investigated generic model is between 4.9 kHz and 5.2 kHz depending on the backing thickness. The interval to search for $\widehat{V}_n$ is set from 4.5 kHz to 5.6 kHz. Fig. 4 shows that the cross-coupling is highly influenced by the backing thickness. A thicker backing, implying higher stiffness, leads to less cross-coupling. Especially in a range between 2 mm to 6 mm and 9 mm–13 mm, this is not applicable. This is due to the particular dynamic behavior of the backing.

The modes of the system are not well separated. Hence, cross-coupling strongly depends on the particular dynamic behavior of the backing. We want to demonstrate this on the example of two different configurations of the backing thickness, $t_{\mathrm{b}} =$ 3.0 mm and $t_{\mathrm{b}} = 4.0$ mm. Fig. 5 (a) shows the mode shapes and the associated eigenfrequencies of the system with $t_{\mathrm{b}} = 3.0$ mm in the range of interest. In the first mode shape, the bending elements move with the opposite phase (out-of-phase). In the second mode shape they move with the same phase (in-phase). The difference in eigenfrequency between in-phase and out-of-phase modes is $\Delta f = 208$ Hz. In comparison, Fig. 5 (b) shows the modes of the system with $t_{\mathrm{b}} = 4.0$ mm. In this case, the

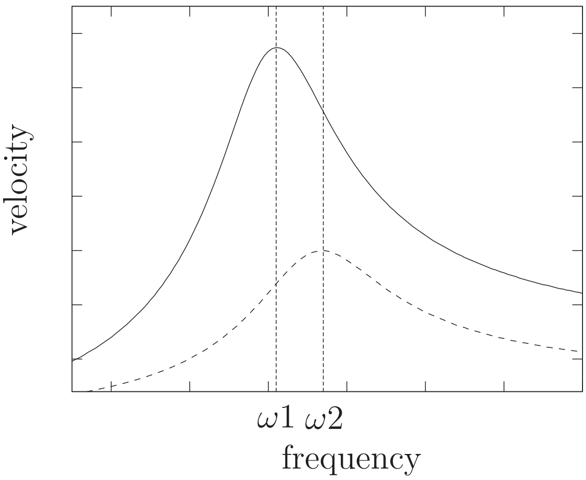

Fig. 3. Scheme of velocity spectra to calculated cross-coupling P_n. Frequency of resonance can vary between active (—) and passive bending (- -) element.

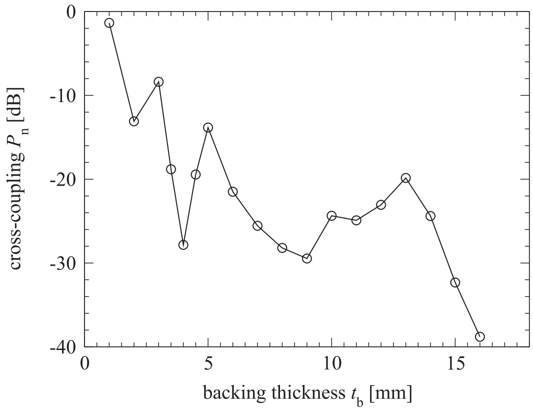

Fig. 4. Cross-coupling P_n dependence on backing thickness t_b.

difference in eigenfrequency between the in-phase and out-of-phase modes is only $\Delta f = 20$ Hz. Weak cross-coupling can be attributed to the small difference in eigenfrequency of the in-phase and out-of-phase modes. Similar relations between cross-coupling and difference in eigenfrequency are found in Ref. [27]. Thus, the behavior of weak mechanical cross-coupling caused by a common backing could be interpreted as low transfer mobility between active and passive bending element, caused by strong cancellation between the in-phase and out-of-phase mode. Meanwhile, the influence on the point mobility is negligible. The cancellation effect also depends on the damping of the system. If a system has a certain difference in eigenfrequency Δf between the in-phase and out-of-phase modes, higher damping causes weaker cross-coupling. This can be explained by a higher bandwidth of the peak in the harmonic analysis of in-phase and out-of-phase modal contributions. Thus, the magnitudes of the modal contributions for a certain frequency are more similar than in cases of lower damping. As the phase difference between the modes remains 180°, the cancellation effect is higher in systems with higher damping.

Fig. 6 shows the dependence of cross-coupling P_n on the difference in eigenfrequency Δf between the in-phase and out-of-phase modes. The results are calculated in the generic model with the same data as before. The backing thickness t_b is varied again in the range from 1 mm to 16 mm. With growing difference in eigenfrequency Δf, the cross-coupling P_n raises.

An outlier can be found for $\Delta f = 12.3$ Hz with cross-coupling of $P_n = -19.4$ dB. This point belongs to the generic model with $t_b = 4.5$ mm. In this case, a weakness of the previous presented method to calculate cross-coupling emerge. In some systems with weak cross-coupling (< -25 dB) nearby modes, dominated by the particular dynamic behavior of the backing, are excited quite strong. Thus, the amplitude $\widehat{V_2}$ is located at a different frequency. By this, a motion of the whole backing is analyzed rather than cross-coupling. An even better result can be achieved by reducing the interval of searching for $\widehat{V_2}$ in this system. To keep the calculation of cross-coupling P_n comprehensible, the authors decide to not change the range of searching for $\widehat{V_2}$ for this system.

Based on the results presented in Fig. 6, it is possible to evaluate the cross-coupling qualitatively in different phased array systems with comparable damping by a modal analysis. The objective to minimize is the difference in eigenfrequency Δf between the in-phase and the out-of-phase modes. This is an advantage for design optimization of phased array structures because a modal analysis requires less computational effort than a harmonic analysis over a broad frequency band.

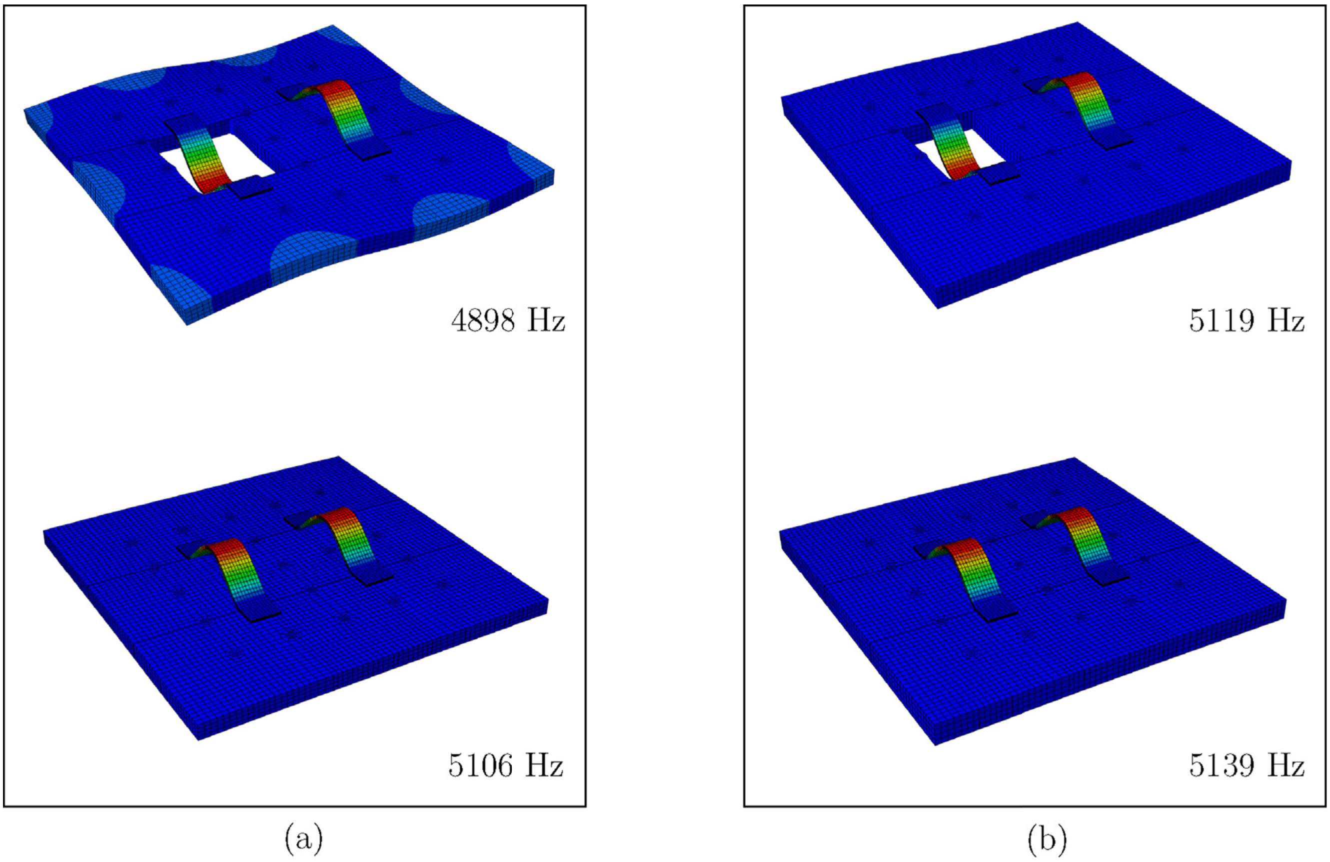

Fig. 5. Modes of interest with backing thickness (a) t_b = 3.0 mm and (b) t_b = 4.0 mm. Note: For a better visibility, some elements of the backing are not shown in the first mode shape.

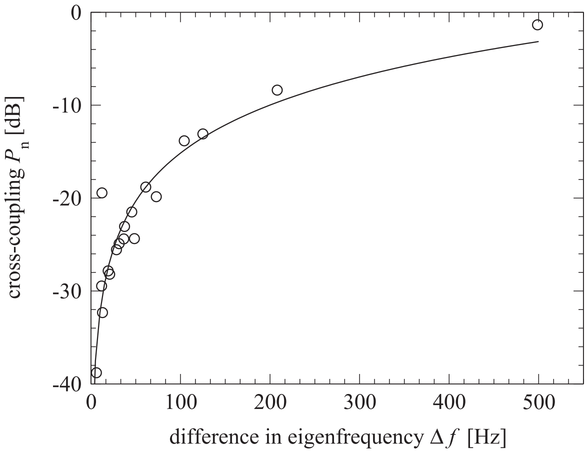

Fig. 6. Dependence of cross-coupling P_n on difference in eigenfrequency Δf between in-phase and out-of-phase mode.

3. Stop band material as backing

Mechanical cross-coupling in phased array transducers is highly influenced by the dynamic behavior of the backing as shown above. However, the reduction of cross-coupling by minimizing the difference in eigenfrequency between the in-phase and out-of-phase mode is connected to avoid the coincidence of backing dominating modes with the operating frequency. This leads to design issues for arrays with a larger number of transducer elements. More transducer elements require a larger backing. Thus, the modal density increases in the frequency range around the operating frequency. The matter even getting worse if the operating frequency is increased. To overcome this problem, a stop band material is introduced as a common backing. Stop band material can attenuate the wave propagation in the backing. Therefore, we create an extended model derived from the generic model. It contains a large number of small, equal resonators on the downside of the backing. These resonators can be tuned in

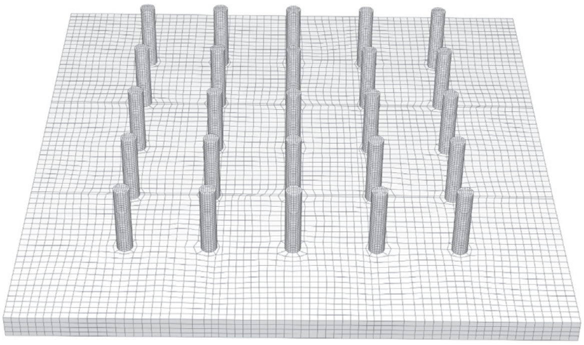

Fig. 7. Finite element model of the backing with a 5 × 5 grid of beam resonators on the downside.

order to change the frequency range where the backing shows a stop band behavior.

3.1. Design of stop band material

Stop band behavior in plates can be obtained if the resonator spacing s_{res} fits the requirement to be small enough in relation to the wavelength in the backing. Therefore, the ratio of the resonator frequency f_{res} to the frequency where the wavelength in the backing equals twice the resonator spacing $f_{\mathrm{plate}_{\lambda=2s_{\mathrm{res}}}}$ should be equal to or less than 1 [15]. According to Kirchoff plate theory, the wavelength in infinite plates is calculated by

$$\lambda = \frac{c_{\mathrm{plate}}}{f} \,, \tag{5}$$

with

$$c_{\mathrm{plate}} = \sqrt{\omega} \cdot \sqrt[4]{\frac{h^2\ E}{12\ \rho\ \left(1-\nu^2\right)}} \,.$$

A basic description is given in Ref. [28, p. 146].

Following the guideline given in Ref. [15] for the dimensionless frequency ratio

$$\frac{f_{\mathrm{res}}}{f_{\mathrm{plate}_{\lambda=2s_{\mathrm{res}}}}} \le 1 \,, \tag{6}$$

the maximum resonator spacing s_{res} can be calculated by

$$f_{\mathrm{plate}} = \frac{2\pi}{\lambda^2} \sqrt{\frac{h^2\ E}{12\ \rho\ (1-\nu^2)}} \,, \tag{7}$$

$$s_{\mathrm{res}} = \sqrt{\frac{\pi \sqrt{\frac{h^2\ E}{12\ \rho\ (1-\nu^2)}}}{2f_{\mathrm{res}}}} \,. \tag{8}$$

The resonators will be tuned so that the first resonance frequency f_{res} coincides with the operating frequency of the bending elements of the phased array transducer $f_{\mathrm{r}} = 5.2$ kHz. The calculated wavelength is $\lambda = 44.5$ mm for the backing without resonators at this frequency. This result has been verified in a time domain simulation of the finite element model. Consequently, the resonator spacing should be less than 22.3 mm. To investigate the influence of stop band material on cross-coupling in the generic model, a 5 × 5 grid of beam resonators is used as shown in Fig. 7. In order to reduce cross-coupling, a significant wave attenuation between the bending elements is desired. Therefore, a spatial placement with one row of resonators between the bending elements is applied. The center to center spacing of the resonators is set to $s_{\mathrm{res}} = 10.75$ mm which corresponds to $s_{\mathrm{res}} \approx \lambda/4$. The resonators with a diameter of 2.05 mm can be tuned by trimming the beams length. The influence of stop band material on the cross-coupling is investigated for the system with $t_{\mathrm{b}} = 3$ mm. This system has high cross-coupling. In simulation, the beam resonators are modeled with C3D20R elements with a structured mesh. The average element edge length is 0.2 mm. The beam resonators are connected with a tie constraint by a surface-to-surface formulation to the backing. Studies show that the error introduced by meshing is negligible for the effect of cross-coupling.

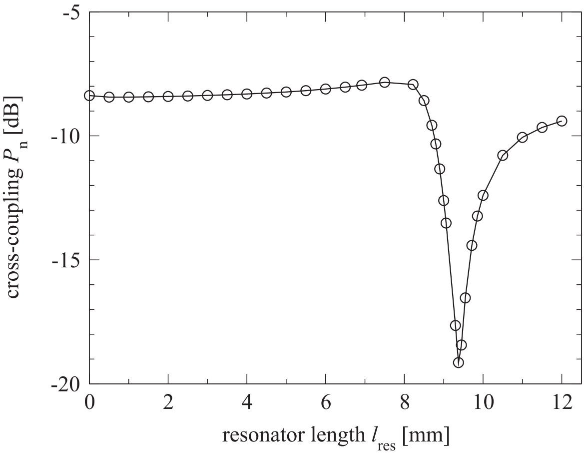

Fig. 8. Cross-coupling P_n dependence in the extended model on resonator length l_{res}.

3.2. Cross-coupling dependence on resonator length

The beam length is varied in a range between $1 \cdot 10^{-3}$ mm and 12 mm. Fig. 8 shows the cross-coupling dependence on the resonator length. Between 8.9 mm and 9.5 mm a high attenuation in cross-coupling can be achieved. In this range, the band of resonance frequency of the resonators fits the resonance frequency of the bending elements. The backing shows stop band behavior and the free wave propagation is attenuated. At a resonator length of 9.4 mm, the system has minimum cross-coupling with −19.1 dB.

In this configuration, the resonators increase the mass of the backing by 5.3% in comparison to the generic model without resonators. The influence of increased mass is evaluated in the generic model without resonators. Therefore, the density of the backing is increased by 5.3% in finite element simulation which leads to $P_n = -7.2$ dB. In this way, it is shown that the reduction of cross-coupling is not caused by the added mass but by the dynamic behavior of the stop band material.

3.3. Stop band behavior

Dispersion curves are common to analyze the behavior of periodic structures. The aim is to identify wave propagation in structures within a certain frequency range. In this study, they are calculated by applying the Floquet Bloch theorem in an undamped finite element model. The simulations are carried out with the commercial software COMSOL Multiphysics 5.3. As the theory of calculation is widely discussed in literature and is not on scope of this work, the authors refer to literature, e.g. Refs. [15,17,29,30].

The dispersion curves are used to proof the stop band behavior of the above described backing with attached beam resonators of the length 9.4 mm. As a reference, wave propagation is calculated for a unit cell representing the pure backing without a beam resonator as shown in Fig. 9 (a). The dimensions of the plate-like part of the unit cells are identical. The lattice has a 2D periodicity. Due to symmetry of the square unit cell, wave propagation has to be calculated along the contour of the triangle ΓXMΓ, cf. Fig. 9. The triangle represents the so called irreducible Brillouin zone (IBZ) [15].

To identify different types of waves propagating at the operating frequency of the phased array transducer, Fig. 10 shows the displaced unit cell of the pure backing. The corresponding points are marked in Fig. 11. Analyzing the displacements, three different wave types are found, an in-plane longitudinal wave (⋆), a shear wave (○), and a bending wave (∗). Comparable results with regard to a plate-like structure without resonators are described in Ref. [31]. Fig. 11 (b) shows the dispersion curves of the unit cell with an attached beam resonator. A major influence on the propagation of the shear wave and the bending wave is obtained. Thus, shear waves and bending waves can not propagate in the backing at the operating frequency of the phased array transducer. This reduces mechanical cross-coupling caused by a common backing.

To ensure that the stop band is related to the resonant behavior of the beam, dispersion curves of two additional test cases are calculated. The test cases refer to a beam length of 7.0 mm, cf. Fig. 12 (a) and 11.0 mm, cf. Fig. 12 (b). It is shown that changing the length of the beam resonator results in a changed stop band. Thus, the stop band with no wave propagation for shear and bending waves does not coincide with the operating frequency. In the first test case with beam length of 7.0 mm, in-plane longitudinal wave, shear wave, and bending wave can propagate at the operating frequency. In the second test case, the dispersion curves present at the operating frequency contain shear wave components. It is shown that the stop band is related to the resonant behavior of the beam. Due to the small width of the stop band, cf. Fig. 11, and the high sensitivity to the beam length, cf. Fig. 12, the curve of Fig. 8 shows high sharpness in the range between 8.0 mm and 11.0 mm. Finally, the reducing of mechanical cross-coupling can be admitted to the application of resonant stop band material as backing.

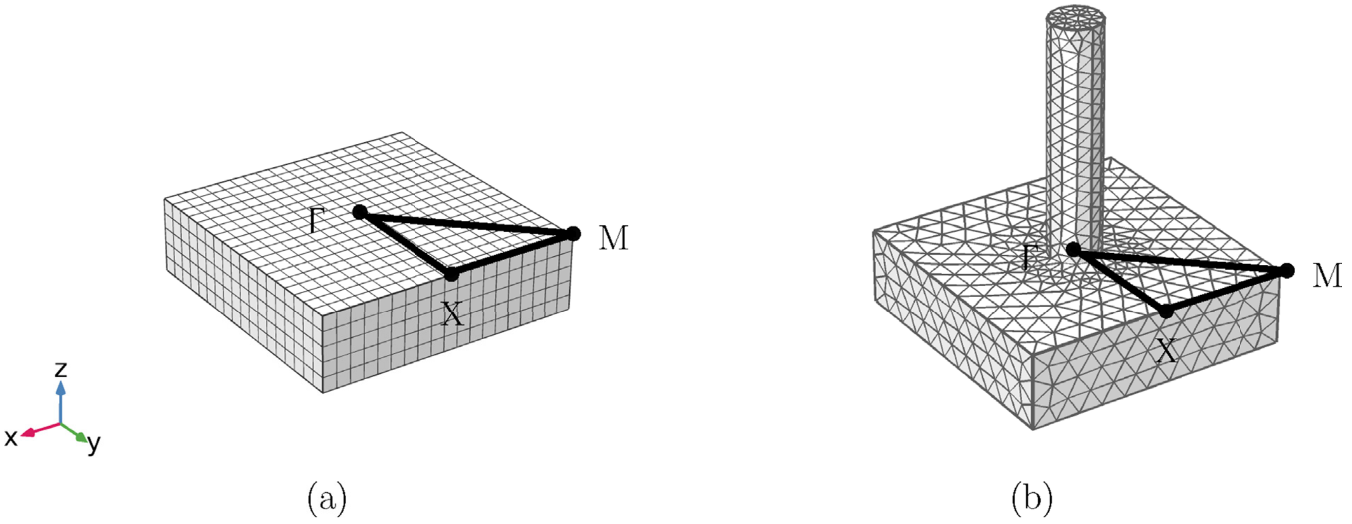

Fig. 9. (a) Unit cell without beam resonator. (b) Unit cell with attached beam resonator of 9.4 mm length.

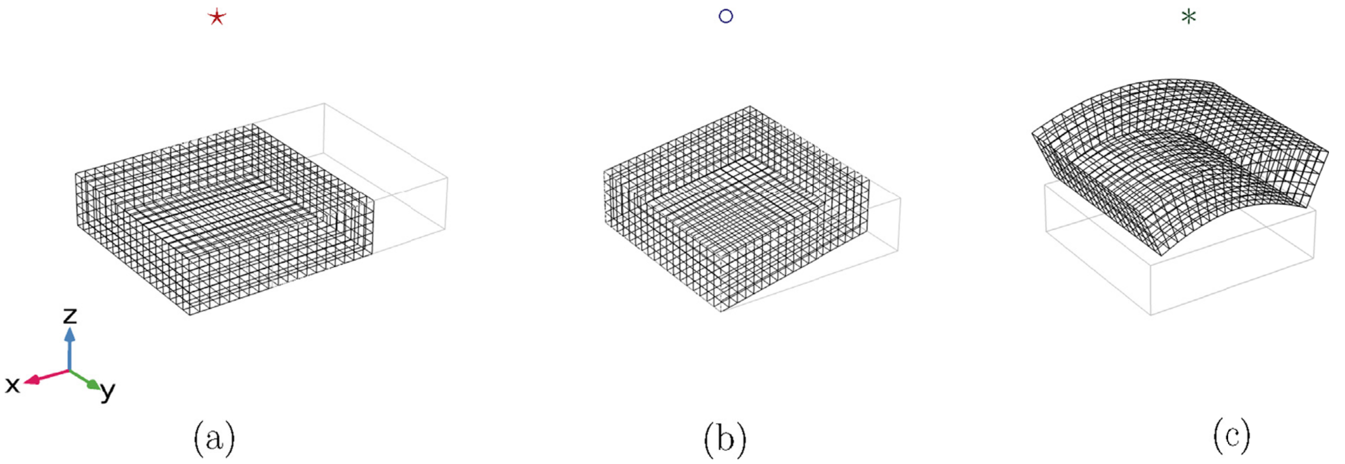

Fig. 10. The displacements of the unit cell without beam resonator are shown for the corresponding points marked in Fig. 11 (a). Three different wave types are identified: in-plane longitudinal wave (a), the shear wave (b), and the bending wave (c). The undeformed outlines are shown in gray.

4. Experimental validation

In this section, we validate the finite element simulation for the generic model as well as for the extended model by experimental testing. Firstly, we describe the specimen preparation and test setup. Afterwards, the effect of stop band materials on cross-coupling in a real setup is shown and compared to the results from Section 3. Finally, we compare the frequency response function (FRF) from the finite element simulation and the experiment to evaluate the differences between numerical and experimental results.

4.1. Specimen preparation and assembling

The experimental validation requires specimens with high geometrical accuracy. A major challenge is the preparation of an epoxy backing with 25 local resonators. The preparation as one piece is desired to avoid additional joints between backing and resonators which may have different mechanical properties. The preparation of the backing with local resonators can be done by casting epoxy in a mold which has the negative form of the backing. Especially the demold process requires high effort since small and long resonator beams tend to break during demolding. This issue possibly increases in real world applications where the operating frequency is higher and consequently the dimensions of the stop band material are smaller. To overcome this issue, it would be possible to assemble separately manufactured beam resonators and backing in an additional process. Fig. 13 (a) shows the prepared backing with 25 beam resonator on the downside. The bending elements and the backing are coated with aluminum by thermal evaporation to form electrodes. By covering certain areas of the backing, it is possible to separate the counter-electrodes for each transducer element.

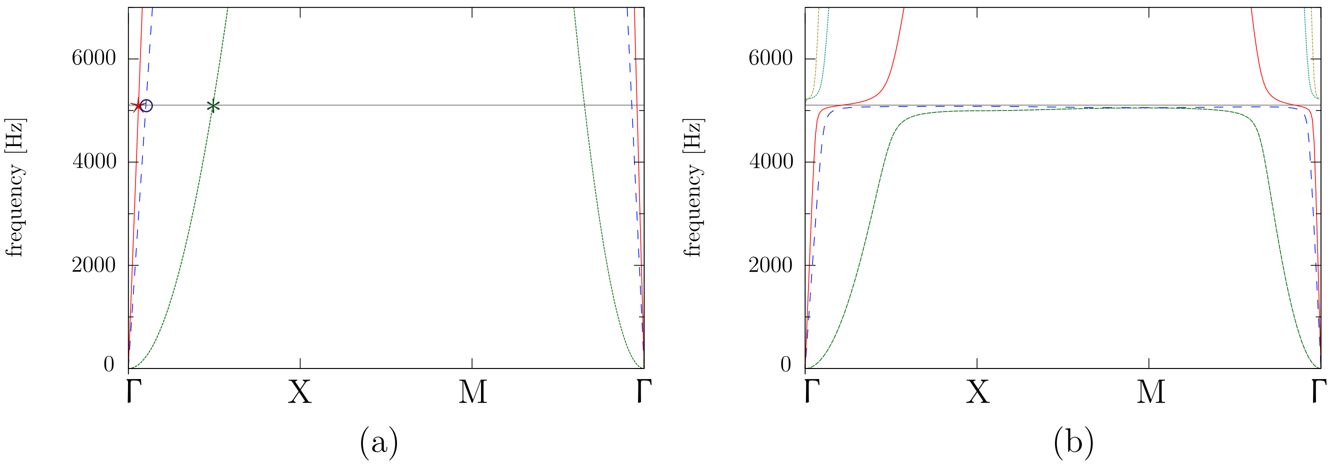

Fig. 11. Dispersion curves for different unit cells, operating frequency marked by horizontal line at 5.1 kHz (a) without beam resonator. (b) backing with attached, well tuned beam resonator, length 9.38 mm.

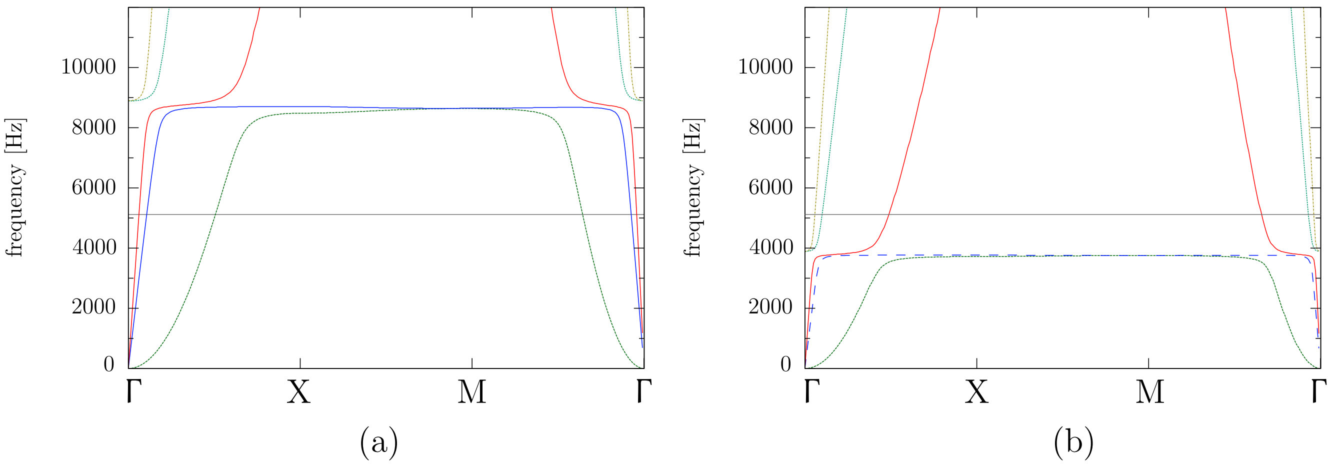

Fig. 12. Dispersion curves for different unit cells, operating frequency marked by horizontal line at 5.1 kHz (a) backing with attached, poorly tuned beam resonator, length 7.0 mm (b) backing with attached, poorly tuned beam resonator, length 11.0 mm.

Another challenging process is the assembling of the bending elements and the backing. The boundary conditions for the vibrational properties of the bending elements are defined by the length between the epoxy sockets. The bending elements are jointed with cyanoacrylate adhesive to the epoxy sockets. Thus, a small air gap between the electrodes is realized. The assembly is finished by connecting electrical wires with copper tape to the electrodes.

The influence of the local resonators on the cross-coupling is investigated with one and the same specimen. By this, differences in cross-coupling maybe caused by the single parts, preparation and assembly of the specimen can be avoided. The model is prepared using a backing with local resonators of 12 mm length. The length of the local resonators can be trimmed stepwise by sanding. In this way, it is possible to measure the cross-coupling influenced by local resonators with different length at one specimen.

4.2. Test setup for cross-coupling measurement

For experimental testing of cross-coupling, a non-contact measurement is done with a scanning laser Doppler vibrometer. The specimen is placed on two horizontal tighten yarns. By this, free-free boundary conditions can be approximated. Fig. 13 (b) shows the set up generic model during experimental testing. The active element is excited by an electrical voltage between the capacitor electrodes. In a range from 4.5 kHz to 6 kHz a periodic signal, called pseudo random, is applied. This signal type excites all frequencies of the measured spectrum simultaneously and does not cause leakage effects [32]. The signal from the signal generator is amplified with a high voltage amplifier which amplifies the alternating current (AC) excitation voltage and

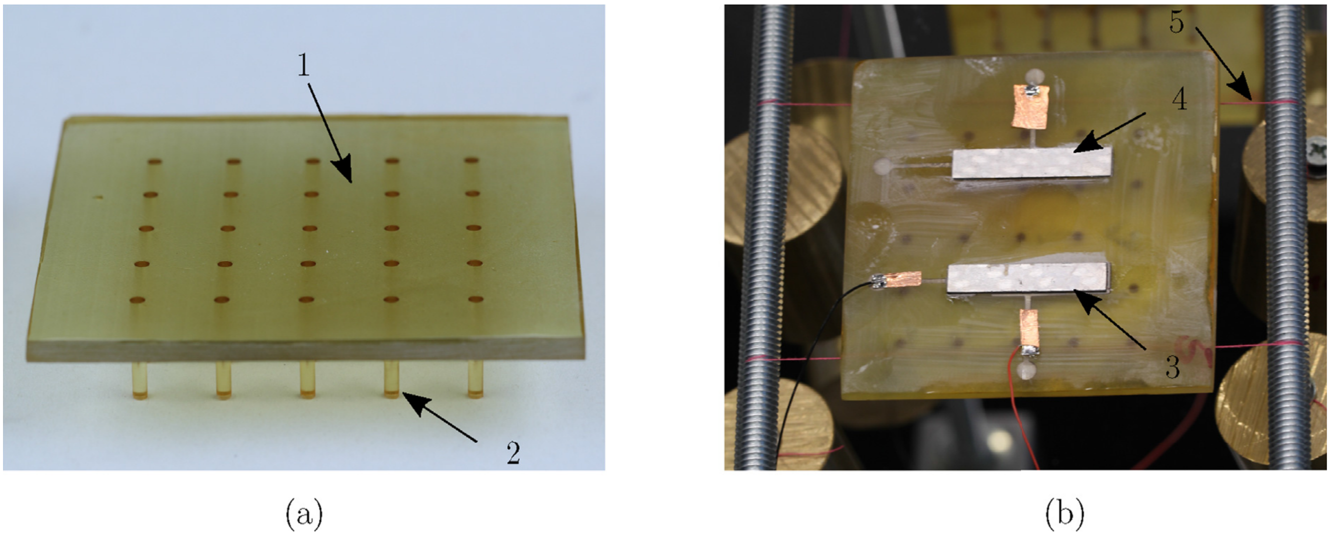

Fig. 13. Backing with beam resonators (a) and experimental test setup (b): (1) backing, (2) beam resonator, (3) active bending element, (4) passive bending element, (5) tighten yarn.

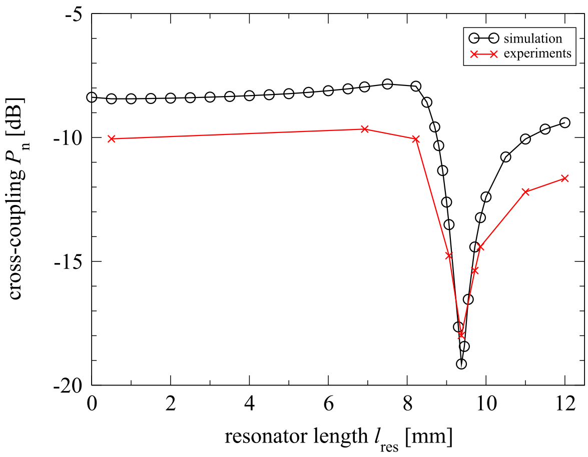

Fig. 14. Cross-coupling P_n dependence on resonator length l_{res} in the extended model. Comparison of results from simulations and experiments.

generates an additional 200 V direct current (DC) offset. The velocity spectrum is measured at 27 scanning points for each bending element. Cross-coupling is calculated at the resonance frequency of each bending element like described in Eq. (4).

4.3. Cross-coupling dependence on resonator length

The length of the beam resonators is trimmed to fit the stop band to the operating frequency of the phased array transducer. Fig. 14 shows the cross-coupling depending on the resonator length. Between 9.0 mm and 10 mm, a major reduction of cross-coupling is achieved in simulation as well as in experiment. Reasonable agreement between numerical simulation and experimental testing is attained. The reduction in cross-coupling is attributed to the stop band behavior of the backing achieved by the local resonators on the downside. The most effective reduction can be achieved at 9.4 mm. The mechanical cross-coupling is reduced from −10.1 dB to −18.0 dB.

In case of resonators with 12 mm length, the frequency range of the stop band does not coincide with the operating frequency of the phased array transducer. The mechanical cross-coupling is −11.6 dB. By this, it is verified that the reduction of cross-coupling is caused by the stop band behavior.

4.4. Harmonic analysis

To evaluate the differences between simulation and experiment, the FRFs of both are compared. Therefore, the generic model without resonators and $t_b = 3$ mm is analyzed. As the electrodynamic behavior is out of scope of this study, the excitation in the finite element simulation is applied by a mechanical load. However, the input parameter for the experiment is an electrical

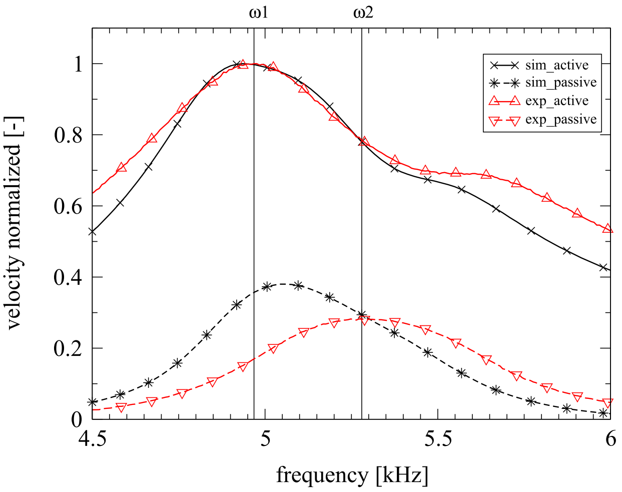

Fig. 15. Normalized frequency spectrum from simulation and experimental testing of the generic model. Results from numerical simulation active (×) and passive (∗) bending element. Results form experimental testing (△) and passive (▽) bending elements.

voltage. To compare the FRFs of the experiment and simulation, they are normalized to 1 at maximum of the active bending element. Fig. 15 shows a reasonable agreement between simulation and experiment.

In the experiment, a shift in resonance frequency for the passive bending occurs. This can be ascribed to small differences in free length of the bending element. Due to the rheological behavior, the adhesive easily flows and changes free length between the epoxy sockets in preparation process. As the resonance frequency is highly sensitive to the free length, this is a major challenge during the application process of the bending elements. In Section 2, the calculation of cross-coupling P_n is explained. Analyzing Fig. 15 it becomes clear, that it leads to differences whether P_n is calculated at a fixed frequency by $P_\mathrm{n} = \frac{V_2(\omega 1)}{V_1(\omega 1)}$, e.g. the resonance frequency of the active element, or at the resonance frequency of each bending element $P_\mathrm{n} = \frac{V_2(\omega 2)}{V_1(\omega 1)}$.

4.5. Discussion

The simulations of the generic and the extended models are validated with experimental measurements. In configurations with resonator length 1 mm–9 mm and 10 mm–12 mm, the frequency range of the stop band is poorly tuned to the operating frequency. In this cases, less cross-coupling is present in experiments than in simulations. This can be attributed to different resonance frequencies of the bending elements in experiments. Furthermore, cross-coupling is highly influenced by damping. As the precise determination of dynamic material parameters, given in Table 2, is complex and influenced by uncertainties, this can be another reason for this differences. However, the accordance between simulation and experimental measurements is quite good as the absolute difference in cross-coupling P_n varies between 1.3 dB and 2.2 dB. The frequency range of the stop band and the operating frequency coincides between 9 mm and 10 mm resonator length. In this case, a major reduction of cross-coupling is obtained in simulations and in experiments. It is reduced in experiments by 7.9 dB. In contrary to the poorly tuned configuration, the cross-coupling at 9.4 mm is higher in the experiment than in simulation. The reason for that can be found in tuning the resonators by sanding. This causes a variance in the length of each resonator. Thus, the effect of wave attenuation at a certain frequency is smaller than under ideal conditions, where the resonators have all the same length. Nevertheless, the difference between the simulation and the experimental measurements is only 1.1 dB.

5. Conclusion

The authors presented a study on mechanical cross-coupling in air-coupled phased array transducers with low operating frequency. In a generic model, the behavior of cross-coupling is investigated with special focus on the influence of the common backing. In finite element simulation, a generic model with two single transducers is set up. They are realized as capacitive transducers with bending elements which are bonded on the common backing. In order to reduce mechanical cross-coupling, stop band material as backing is investigated in this study. Therefore, beam resonators are attached on the downside of the backing. The frequency range of the stop band is tuned by trimming the length of the beam resonators. The effect on cross-coupling is investigated in numerical simulation and experimental testing. The authors conclude that in low frequency air-coupled phased array transducers

(i) mechanical cross-coupling highly depends on the particular dynamic behavior of the common backing,
(ii) the difference in eigenfrequency between in-phase and out-of-phase mode of the bending elements is an indicator of mechanical cross-coupling. A higher difference in eigenfrequency indicates a stronger mechanical cross-coupling and

(iii) stop band material realized with local resonators on the downside of the backing is a suitable solution to achieve a major reduction of mechanical cross-coupling.

The presented results offer a new possibility to estimate mechanical cross-coupling in similar low frequency phased array transducers with a common backing based on a modal analysis. This is an advantage for optimization problems, as a modal analysis usually requires less computational effort than a harmonic analysis. In further studies, the influence of uncertainties in material and geometry should be investigated in detail. Nevertheless, by experimental results of this study it is shown that a major reduction in mechanical cross-coupling can be achieved with stop band material in a real setup.

Acknowledgements

The authors gratefully acknowledge Robert Bosch GmbH Germany for the funding of this research.

References

[1] S. Harput, A. Bozkurt, F.Y. Yamaner, Ultrasonic phased array device for real-time acoustic imaging in air, in: IEEE Ultrason. Symp, 2008, pp. 619–622.
[2] S. Harput, A. Bozkurt, Ultrasonic phased array device for acoustic imaging in air, IEEE Sens. J. 8 (11) (2008) 1755–1762.
[3] G.S. Kino, Acoustic imaging for nondestructive evaluation, Proc. IEEE 67 (4) (1979) 510–525.
[4] D. Ekeom, A.H. Henni, G. Cloutier, Design of a phased-array for radiation force generation following a closed path, in: IEEE Int. Ultrason. Symp, 2010, pp. 662–665.
[5] R.L. Baer, G.S. Kino, Theory for cross coupling in ultrasonic transducer arrays, Appl. Phys. Lett. 44 (10) (1984) 954–956.
[6] J.D. Larson, Non-ideal radiators in phased array transducers, in: Ultrason. Symp, 1981, pp. 673–684.
[7] J. Dias, An experimental investigation of the cross-coupling between elements of an acoustic imaging array transducer, Ultrason. Imaging 4 (1) (1982) 44–55.
[8] C. DeSilets, Transducer Arrays Suitable for Acoustic Imaging, Ph.D. thesis, Stanford Univ., CA, 1978.
[9] J.S. Bird, S. Asadov, P. Kraeutner, Improving arrays for multi-angle swath bathymetry, in: Oceans Conference Record (IEEE), vol. 4, 2003, pp. 2085–2092.
[10] A. Bozkurt, F.L. Degertekin, A. Atalar, B.T. Khuri-Yakub, Analytic modeling of loss and cross-coupling in capacitive micromachined ultrasonic transducers, in: IEEE Ultrason. Symp., vol. 2, 1998, pp. 1025–1028.
[11] R.J. Kazys, R. Sliteris, J. Sestoke, Air-coupled low frequency ultrasonic transducers and arrays with PMN-32% PT piezoelectric crystals, Sensors 17 (2017) 1–20.
[12] M. Celmer, K. Opielinski, Research and modeling of mechanical crosstalk in linear arrays of ultrasonic transducers, Arch. Acoust. Q. 41 (3) (2016) 599–612.
[13] M. Celmer, K.J. Opielinski, M. Dopierala, Structural model of standard ultrasonic transducer array developed for fem analysis of mechanical crosstalk, Ultrasonics 83 (2018) 114–119.
[14] Z. Liu, X. Zhang, Y. Mao, Y.Y. Zhu, Z. Yang, C.T. Chan, P. Sheng, Locally resonant sonic materials, Science 289 (5485) (2000) 1734–1736.
[15] C.C. Claeys, K. Vergote, P. Sas, W. Desmet, On the potential of tuned resonators to obtain low-frequency vibrational stop bands in periodic panels, J. Sound Vib. 332 (2013) 1418–1436.
[16] C.C. Claeys, P. Sas, W. Desmet, On the acoustic radiation efficiency of local resonance based stop band materials, J. Sound Vib. 333 (2014) 3203–3213.
[17] C. Kittel, Introduction to Solid State Physics, Wiley, Hoboken, NJ, 2005.
[18] N. Kaina, F. Lemoult, M. Fink, G. Lerosey, Ultra small mode volume defect cavities in spatially ordered and disordered metamaterials, Appl. Phys. Lett. 102 (14) (2013) 144104.
[19] M. Rupin, F. Lemoult, G. Lerosey, P. Roux, Experimental demonstration of ordered and disordered multiresonant metamaterials for lamb waves, Phys. Rev. Lett. 112 (2014) 234301.
[20] Y. Xiao, J. Wen, X. Wen, Flexural wave band gaps in locally resonant thin plates with periodically attached spring-mass resonators, J. Phys. D Appl. Phys. 45 (19) (2012) 195401.
[21] R.H. Olsson III, I. El-Kady, Microfabricated phononic crystal devices and applications, Meas. Sci. Technol. 20 (1) (2009) 012002.
[22] S. Köllner, Modelling and Simulation of Ultrasonic Transducers Based on Composites (Modellbildung und Simulation von Ultraschallwandlern auf Basis von Verbundwerkstoffen), Karlsruhe Institute of Technology, Department of Mechanical Engineering, 2014. Master's thesis.
[23] J.C. Halpin, J.L. Kardos, The halpin-tsai equations: a review, Polym. Eng. Sci. 16 (5) (1976) 344–352.
[24] D. Hull, T.W. Clyne, An Introduction to Composite Materials, second ed., Cambridge Solid State Science Series, Cambridge University Press, 1996.
[25] R. Akkerman, Laminate mechanics for balanced woven fabrics, Compos. B Eng. 37 (2) (2005) 108–116.
[26] P. Langer, M. Maeder, C. Guist, M. Krause, S. Marburg, More than six elements per wavelength: the practical use of structural finite element models and their accuracy in comparison with experimental results, J. Comput. Acoust. 25 (4) (2017) 1750025.
[27] R. Reiß, Simulation and Optimization of Ultrasonic Transducers in Arrays (Simulation und Optimierung von Ultraschallwandlern im Mehrelemente-Verbund), University of Stuttgart, Institute of Applied and Experimental Mechanics, 2014. Master's thesis.
[28] M. Möser, Technical Acoustics (Technische Akustik), tenth ed., Springer-Verlag, Berlin Heidelberg New York, 2015.
[29] L. Brillouin, Wave Propagation in Periodic Structures: Electric Filters and Crystal Lattices, Dover Publications, 1953.
[30] M. Collet, M. Ouisse, M. Ruzzene, M. Ichchou, Floquet–bloch decomposition for the computation of dispersion of two-dimensional periodic, damped mechanical systems, Int. J. Solids Struct. 48 (20) (2011) 2837–2848.
[31] C. Claeys, E. Deckers, B. Pluymers, W. Desmet, A lightweight vibro-acoustic metamaterial demonstrator: numerical and experimental investigation, Mech. Syst. Sig. Process 70 (2016) 853–880.
[32] Polytec GmbH, Polytec-Platz 1-7, 76337 Waldbronn, Germany, Theory Manual Polytec Scanning Vibrometer PSV Theory, As of Software 9.1 Edition.